UNIVERSIDAD COMPLUTENSE DE MADRID

FACULTAD DE CIENCIAS FÍSICAS

TESIS DOCTORAL

Simulaciones de turbulencia en plasmas del stellarator Wendelstein 7-X.
Comparaciones entre códigos y con medidas experimentales

Plasma turbulence simulations in the stellarator Wendelstein 7-X.
Comparisons between codes and with experimental measurements

MEMORIA PARA OPTAR AL GRADO DE DOCTOR

PRESENTADA POR

Antonio González Jerez

DIRIGIDA POR

José Manuel García Regaña
Iván Calvo Rubio

Simulaciones de turbulencia en plasmas del stellarator Wendelstein 7-X

Comparaciones entre códigos y con medidas experimentales

Plasma turbulence simulations in the stellarator Wendelstein 7-X

Comparisons between codes and with experimental measurements

By

Antonio González Jerez

Universidad Complutense de Madrid
Facultad de Ciencias Físicas
Programa de Doctorado en Física

Supervisors:

Dr. José Manuel García Regaña

Prof. Iván Calvo Rubio

Simulaciones de turbulencia en plasmas del stellarator Wendelstein 7-X

Comparaciones entre códigos y con medidas experimentales

Plasma turbulence simulations in the stellarator Wendelstein 7-X

Comparisons between codes and with experimental measurements

By

Antonio González Jerez

Universidad Complutense de Madrid
Facultad de Ciencias Físicas
Programa de Doctorado en Física

Supervisors:

Dr. José Manuel García Regaña

Prof. Iván Calvo Rubio

Para mi familia y amigos

Acknowledgements

Quisiera redactar los agradecimientos de este trabajo en castellano, para que todos aquellos a quienes están dirigidos puedan comprenderlos fácilmente.

En primer lugar, quiero expresar mi más profundo agradecimiento a mi familia. A mis padres, por su amor incondicional y por inculcarme desde pequeño la importancia del conocimiento y la perseverancia. A mis tíos y tías, por tratarme siempre como a un hijo más y brindarme su apoyo. A mi hermana, porque aunque quizá no lo sepa, también ha sido una parte fundamental de este trabajo y a Lari, por aguantarme en el tramo final de este proceso. No puedo dejar de mencionar a mis queridos abuelos, quienes, aunque ya no están para ver la culminación de este proyecto, han sido las mejores personas que he conocido. Siempre estarán presentes en mi corazón, apoyándome desde donde estén.

Mi más sincero agradecimiento a mis compañeros de andanzas, quienes lograron que el edificio 20 se transformara, a mis ojos, en un lugar donde deseaba estar, a pesar de su apariencia desgastada. No quiero olvidar a aquellos que finalizaron su trabajo antes que yo y sirvieron de pioneros, como Raúl, Dhaval y Sadig, gracias por vuestro apoyo a lo largo de todo este recorrido. Las múltiples horas pasadas en ese edificio fueron memorables gracias a las conversaciones 'profundas' con Javi y las clases de español con Manolis. El ambiente, ya de por sí excelente, se enriqueció aún más con la llegada de Pedro, Jaime, Guillermo y Álex, quienes hicieron de mi despacho el suyo (de una forma casi literal). Agradezco también a Nerea, la única con un gusto musical exquisito en todo el edificio. No puedo dejar de mencionar a los veteranos del lugar: José, que se ha convertido en un hermano mayor, y Álvaro, el prófugo que abandonó el edificio cuando yo me fui al no aguantar mi marcha. Gracias, amigos, sabéis que ahora sois parte fundamental de mi familia.

Un agradecimiento muy especial a mis directores de tesis, Iván y José Manuel, por su guía, paciencia y sabiduría a lo largo de estos años. Vuestro apoyo académico y personal ha sido crucial para el desarrollo de esta investigación. Gracias por confiar en mí y por proporcionarme los recursos y el estímulo necesarios para alcanzar este objetivo.

También quiero agradecer a mi tutor, José Manuel Udías Moinelo, por su disposición y celeridad a la hora de realizar cualquier trámite para con la Universidad.

Finalmente, quiero agradecer a todos aquellos que, de una manera u otra, han contribuido a la realización de esta tesis. A mis amigos más allá del ámbito académico, por su comprensión y apoyo en los momentos en que más los necesité. En especial a Óscar que fue capaz de recuperar este documento cuando, tras una serie de catastróficas desdichas, desapareció sin dejar rastro.

A todos, muchas gracias de corazón.

Most of this work has been carried out at the National Fusion Laboratory, CIEMAT (Spain).

Table of Contents

Page

List of publications **xi**

List of Figures **xiii**

List of Tables **xxi**

Resumen **1**

Summary **5**

1 Introduction **9**

1.1 Magnetic confinement fusion 9

1.2 Tokamaks and stellarators 12

1.3 The neoclassically optimized stellarator Wendelstein 7-X (W7-X) and the importance of turbulence 14

1.4 Scope of this thesis 17

2 Gyrokinetic description of a fusion plasma **19**

2.1 Kinetic description of plasmas 19

2.2 δf-gyrokinetic formalism 20

2.3 Gyrokinetic system of equations in a flux tube 25

2.4 The gyrokinetic code `stella`: coordinates and simulation settings 30

3 Parallel boundary conditions in the code `stella` **37**

3.1 Twist-and-shift boundary conditions in flux tube codes 37

3.1.1 Standard twist-and-shift boundary conditions 39

3.1.2 Stellarator symmetric twist-and-shift boundary conditions 40

3.2 Stellarator symmetric twist-and-shift boundary conditions in `stella` . . . 42

3.3 Self-periodic boundary conditions 48
3.4 Summary of this chapter 50

4 Verification of `stella`. Benchmark between the codes `stella` and `GENE` 51
4.1 Configuration and parameters 52
4.2 Linear Simulations 56
4.2.1 Test 1. Linear ITG simulations in the bean flux tube 57
4.2.2 Test 2. Linear ITG simulations in the triangular flux tube 59
4.2.3 Test 3. Linear density-gradient-driven TEM simulations in the bean flux tube 61
4.2.4 Test 4. Linear zonal-flow relaxation in the bean flux tube 62
4.3 Nonlinear simulations 65
4.3.1 Test 5. Nonlinear ITG-driven heat flux 65
4.4 Summary of this chapter 69

5 Comparison of local gyrokinetic simulations with Doppler reflectometry (DR) measurements in W7-X 71
5.1 The DR system in W7-X. Correspondence between k_y and $k_\perp^{DR}$ 72
5.2 Plasma scenario and simulation settings 74
5.3 Radial dependence of density fluctuations: comparison between `stella` results and DR measurements 76
5.4 Numerical characterization of fluctuations in the frequency domain. Predictions for future analysis with the DR system 82
5.4.1 Frequency spectra of density fluctuations 82
5.4.2 Frequency spectra of zonal flow fluctuations 84
5.5 Comparisons between linear and nonlinear calculations of φ^{tb} 85
5.6 Summary of this chapter 90

6 Conclusions and main results of this thesis 93

Bibliography 97

List of publications

- Journal articles as the main author:
  - A. González-Jerez *et al* 2024. *Electrostatic microturbulence in W7-X: comparison of local gyrokinetic simulations with Doppler reflectometry measurements.*
    Nuclear Fusion **64**, 076029. DOI: 10.1088/1741-4326/ad411a
  - A. González-Jerez *et al* 2022. *Electrostatic gyrokinetic simulations in Wendelstein 7-X geometry: benchmark between the codes stella and GENE.*
    Journal of Plasma Physics **88(3)**, 905880310. DOI: 10.1017/S0022377822000393
- Journal articles as a co-author:
  - A. Alonso *et al* 2024. *Density profiles in stellarators: an overview of particle transport, fuelling and profile shaping studies at TJ-II.*
    Nuclear Fusion **64**, 112018. DOI:10.1088/1741-4326/ad67ef
  - H. Thienpondt *et al* 2023. *Prevention of core particle depletion in stellarators by turbulence.*
    Physical Review Research **5**, L022053. DOI: 10.1103/PhysRevResearch.5.L022053
  - C. Hidalgo *et al* 2022. *Overview of the TJ-II stellarator research programme towards model validation in fusion plasmas.*
    Nuclear Fusion **62**, 042025. DOI: 10.1088/1741-4326/ac2ca1
  - T. Sunn-Pedersen *et al* 2022. *Experimental confirmation of efficient island divertor operation and successful neoclassical transport optimization in Wendelstein 7-X.*
    Nuclear Fusion **62**, 042022. DOI: 10.1088/1741-4326/ac2cf5
  - E. Sánchez *et al* 2021. *Gyrokinetic simulations in stellarators using different computational domains.*
    Nuclear Fusion **61**, 116074. DOI: 10.1088/1741-4326/ac2a87

- J.M. García-Regaña *et al* 2021. *Turbulent transport of impurities in 3D devices.*
  Nuclear Fusion **61**, 116019. DOI: 10.1088/1741-4326/ac1d84
- Á. Cappa *et al* 2021. *Stability analysis of TJ-II stellarator NBI driven Alfvén eigenmodes in ECRH and ECCD experiments.*
  Nuclear Fusion **61**, 066019. DOI: 10.1088/1741-4326/abf74b
- J.M. García-Regaña *et al* 2021. *Turbulent impurity transport simulations in Wendelstein 7-X plasmas.*
  Journal of Plasma Physics **87(1)**, 855870103. DOI: 10.1017/S0022377820001543
- S. Yamamoto *et al* 2020. *Effect of ECH/ECCD on energetic-particle-driven MHD modes in helical plasmas.*
  Nuclear Fusion **60**, 066018. DOI: 10.1088/1741-4326/ab7f13
- E. Ascasíbar *et al* 2019. *Overview of recent TJ-II stellarator results.*
  Nuclear Fusion **59**, 112019. DOI: 10.1088/1741-4326/ab205e

- Contributions to conferences:
  - Talks
    - A.González-Jerez *et al. Electrostatic gyrokinetic simulations in Wendelstein 7-X geometry: benchmark between the codes stella and GENE.*
      2nd Fusion HPC Workshop. 03/12/2021. URL
  - Posters
    - A.González-Jerez *et al. Study of turbulent fluctuations in Wendelstein 7-X with gyrokinetic simulations and Doppler Reflectometry.*
      23rd International Stellarator-Heliotron Workshop. 23/06/2022. URL
    - A.González-Jerez *et al.Electrostatic gyrokinetic simulations in Wendelstein 7-X geometry: benchmark between the codes stella and GENE.*
      19th European Fusion Theory Conference. 14/10/2021. URL

List of Figures

Figure **Page**

1.1 Left: average binding energy per nucleon in MeV as a function of the mass number. Figure taken from [3]. Right: reaction rates for different hydrogen isotopes to fuse as a function of the temperature (on logarithmic scale) required for their occurance. Figure taken from [4]. 10

1.2 Time evolution of the highest experimental triple product ($nT\tau_E$) obtained for multiple fusion experiments. Data for devices not yet built are projections. Figure adapted from [6]. 11

1.3 Sketch of different magnetic surfaces, together with some magnetic field lines. The toroidal and poloidal directions are sketched. 13

1.4 Layout of different magnetic confinement devices. Left: a generic tokamak, where the twisted magnetic field is represented with green arrows. The axisymmetric set of external coils is also depicted. Figure adapted from [14]. Right: the stellarator Wendelstein 7-X (W7-X), where some nested magnetic flux surfaces are represented (dark blue, light blue, green and orange) together with the magnetic field lines that lie on the green surface. The complex 3-D geometry of the external coils is clearly depicted. Figure taken from [15]. . . 14

1.5 Left: effective ripple as a function of a normalized radial coordinate, labeling different magnetic surfaces, for two different W7-X configurations (standard (b) and high-mirror (c)) and two different LHD configurations (d,e). Right: neoclassical energy losses, computed with the code DKES [19] and normalized to the heating power as a function of the same normalized radial coordinate for the configurations represented in the left figure. Plots taken from [17]. . . 16

1.6 Power balance analysis for a gas-fuelled discharge in W7-X. The input power is represented as a solid black line and the sum of neoclassical ion and electron energy fluxes (dotted orange line) and radiated power is represented as a solid red line. These results are given as a function of an effective radius, which labels different magnetic surfaces. Figure adapted from [22]. 17

2.1 Sketch of the helical motion of a charged particle (red circle) in the presence of a non-uniform magnetic field, represented in blue. The position vector $\mathbf{r}$, the guiding-centre $\mathbf{X}$ and the gyroradius $\boldsymbol{\rho}_s$ (in green) are also included, together with the drifts in the direction perpendicular to the magnetic field, $\mathbf{v}_\perp$. The perpendicular scale is exaggerated for clarity. 21

2.2 Left: poloidal cross sections of different magnetic surfaces corresponding to the standard configuration of W7-X. They are labeled by r/a=0.5 (yellow), r/a=0.6 (red), r/a=0.7 (blue), r/a=0.8 (green), and r/a=0.9 (black). The radial coordinate r is depicted. Right: sketch of a flux tube surrounding a magnetic field line, represented as a thick black line, that lies on the flux surface $r/a = 0.7$. The coordinates $\{\alpha, \zeta\}$ are also illustrated. 27

3.1 Left: ratio between $|k_x|^{\min}$ and $k_y^{\min}$, or equivalently, between the grid spacing in k_x and k_y for the standard configuration of W7-X as a function of the radial direction, computed using standard twist-and-shift boundary conditions. The vertical dashed lines indicate different radial positions, labeled by $r_0/a = 0.35$ in blue, $r_0/a = 0.5$ in yellow and $r_0/a = 0.7$ in red. Right: global magnetic shear (see expression (3.15)) as a function of the radial direction, computed for the W7-X configuration used for the calculations presented in the left figure. 41

3.2 Factor that relates Δk_x and k_y when using stellarator symmetric twist-and-shift boundary conditions, see expression (3.18), represented as a function of the parallel coordinate, ζ, for the full flux tube length. Results computed for the standard configuration of W7-X in the radial positions labeled by $r_0/a = 0.35$ (left), $r_0/a = 0.5$ (center) and $r_0/a = 0.7$ (right). 42

3.3 Normalized linear growth rates (left) and real frequencies (right) as a function of k_y for a fixed $k_x = 0$ for the surface labeled by $r_0/a = 0.7$ of the standard configuration of W7-X. Results obtained using zero incoming (solid black line), standard twist-and-shift (empty red circles) and stellarator symmetric twist-and-shift (blue stars) boundary conditions. 43

3.4 Time trace of the normalized ion heat flux computed using standard twist-and-shift boundary conditions (red) and stellarator symmetric twist-and-shift boundary conditions (blue) at the radial position $r_0/a = 0.7$ of the standard configuration of W7-X. The dashed lines show the time-averaged quantities over the shadowed time range. 45

3.5 Time trace of the normalized ion heat flux computed using standard twist-and-shift boundary conditions (red) and stellarator symmetric twist-and-shift boundary conditions (blue) at the radial position $r_0/a = 0.5$ of the standard configuration of W7-X. The dashed lines show the time-averaged quantities over the shadowed time range. 46

3.6 Left: Number of k_x values as a function of the maximum computed k_x using standard twist-and-shift (red empty circles) and stellarator symmetric twist-and-shift (blue empty stars) boundary conditions for flux tubes covering nearly one poloidal turn on the surface labeled by $r_0/a = 0.35$ of the standard configuration of W7-X. Right: time-averaged values of ion heat flux calculated for the surface $r_0/a = 0.35$ of the standard configuration of W7-X as a function of the maximum computed value of k_x using standard (empty red circles) and stellarator symmetric (empty blue stars) twist-and-shift boundary conditions. 47

3.7 Right: zoom in to figure 3.6 (right), including the results obtained using exact periodic (in green) and forced periodic (in yellow) boundary conditions. The converged value is depicted as a dashed horizontal line. 49

4.1 3D view of the surface $r_0/a = 0.8$ (a), together with the field line $\alpha_0 = 0$ (solid black line), the field line $\alpha_0 = -\iota\pi/5$ (solid green line) and the last closed flux surface $r_0 = a$ as a semi-transparent halo. Details of two toroidal cuts of the flux surface $r_0/a = 0.8$ are also given, showing a bean-shaped section (b) and a triangular section (c). 53

4.2 Schematic view of the magnetic field lines $\alpha_0 = 0$ (solid black line) and $\alpha_0 = -\iota\pi/5$ (solid green line) extended along the five field periods of W7-X. The magnetic field strength is represented in the background. 54

4.3 Normalized geometric quantities in the range $\zeta - \zeta_0 = [-2\pi, 2\pi]$ for the surface $r_0/a = 0.8$ along the field lines $\alpha_0 = 0$ (solid black line) and $\alpha_0 = -\iota\pi/5$ (dashed green line). The magnetic field strength is represented in (a); the projections of $\hat{\mathbf{b}} \times \nabla B$ and $\mathbf{B} \times \boldsymbol{\kappa}$ along the binormal direction are represented in (b) and (c), respectively; the projections of $\hat{\mathbf{b}} \times \nabla B$ and $\mathbf{B} \times \boldsymbol{\kappa}$ along the radial direction are represented in (d) and (e), respectively. 55

4.4 ITG stability map corresponding to test 1. It shows the growth rate computed with the code `stella` in the bean flux tube as a function of k_x and k_y. . . . 57

4.5 Linear growth rate (left) and real frequency (right) as a function of k_y obtained for the ITG scenario studied in test 1 using `stella` (open circles linked by a solid red line) and `GENE` (open triangles linked by a dashed blue line) in the bean flux tube. The inset of figure (right) shows the structure of the modes $(k_x\rho_i, k_y\rho_i) = (0, 1.3)$ (green line) and $(k_x\rho_i, k_y\rho_i) = (0, 2.1)$ (black line) together with some bad curvature regions (shaded in red). 58

4.6 Linear growth rate (left) and real frequency (right) as a function of k_x obtained for the ITG scenario studied in test 1 using `stella` (open circles linked by a solid red line) and `GENE` (open triangles linked by a dashed blue line) in the bean flux tube. The inset of figure (right) shows the structure of the modes $(k_x\rho_i, k_y\rho_i) = (0.2, 2.1)$ (green line) and $(k_x\rho_i, k_y\rho_i) = (1.7, 2.1)$ (black line), together with a bad curvature region (shaded in red). 59

4.7 ITG stability map corresponding to test 2. It shows the growth rate computed with the code `stella` in the triangular flux tube as a function of k_x and k_y. 60

4.8 Linear growth rate (left) and real frequency (right) as a function of k_x obtained for the ITG scenario studied in test 2 using `stella` (open circles linked by a solid red line) and `GENE` (open triangles linked by a dashed blue line) in the triangular flux tube. The inset of figure (right) shows the structure of the mode $(k_x\rho_i, k_y\rho_i) = (1.2, 2.1)$ (green line) together with a bad curvature region (shaded in red). 60

4.9 Linear growth rate (left) and real frequency (right) as a function of k_y obtained for the instabilities studied in test 3 using `stella` (open circles linked by a solid red line) and `GENE` (open triangles linked by a dashed blue line) in the bean flux tube. 62

4.10 Normalized modulus of the electrostatic potential computed with `stella` (solid red line) and `GENE` (dashed blue line) as a function of ζ over the entire length of the flux tube for some modes simulated in test 3; specifically, we are representing the modes $(k_x\rho_i, k_y\rho_i) = (0, 0.7)$ (a), $(0, 1.2)$ (c) and $(0, 4.7)$ (e). The structures calculated with `stella` are shown as solid green lines in narrower ζ ranges in figures (b), (d) and (f), respectively, together with the normalized magnetic field strength (grey line) and the bad curvature regions (shaded in red). 63

4.11 For test 4, time trace of the flux-surface averaged electrostatic potential normalized to its maximum value computed with `stella` (solid red line) and with `GENE` (dashed blue line) for the pairs $(k_x\rho_i, k_y\rho_i) = (0.05, 0)$ (a), $(k_x\rho_i, k_y\rho_i) = (0.07, 0)$ (b), $(k_x\rho_i, k_y\rho_i) = (0.1, 0)$ (c) and $(k_x\rho_i, k_y\rho_i) = (0.3, 0)$ (d). The insets show a detail of each trace at large times. 64

4.12 Time trace of the normalized ITG-driven heat flux computed with `stella` (solid red line) and `GENE` (dashed blue line) in the bean flux tube for the test 5 scenario. The inset shows a detail of the time interval $tv_{th,i}/a = [1500, 1900]$, with the heat flux time average given by the black dashed lines. 67

4.13 Normalized nonlinear ITG-driven heat flux computed with `stella` in the bean flux tube, averaged over the time interval $tv_{th,i}/a = [1500, 1900]$ and represented as a function of k_x and k_y. 67

4.14 Normalized ITG-driven heat flux averaged over the time interval $tv_{th,i}/a = [1500, 1900]$ computed with `stella` (open circles linked by a solid red line) and `GENE` (open triangles linked by a dashed blue line) in the bean flux tube. It is represented as a function of k_y, summing over k_x (left) and as a function of k_x, summing over k_y (right). 68

4.15 Left: time trace of the normalized ITG-driven heat flux computed with `stella` in the triangular flux tube, together with the heat flux time average over $tv_{th,i}/a = [1200, 1500]$, represented with a black dashed line. Right: this time-averaged ITG-driven heat flux is also represented as a function of k_x and k_y. 68

5.1 Bean cross section of the standard configuration of W7-X. The DR antenna position is represented as a black triangle and the launching direction of the microwave beam as a dashed blue line. The set of points marked with blue crosses indicates the positions where the beam is reflected and the DR diagnostic performs its measurements. These points can be obtained applying ray-tracing techniques. Figure taken from [73]. 73

5.2 Radial profiles for the low (light blue) and high (dark blue) density scenarios. From left to right: density (solid line) and its normalized gradient (dashed line), ion temperature (solid line) and its normalized gradient (dashed line), electron temperature (solid line) and its normalized gradient (dashed line). . 74

5.3 Radial profiles of ι (left) and $\hat{s}$ (right) of the standard configuration considered throughout this study. 75

5.4 Points belonging to the bean (blue dots) and triangular (red squares) flux tubes of W7-X that lay on the plane $\zeta = 0$. The measurement positions for the high density scenario, obtained with `TRAVIS` for the radial locations considered in the gyrokinetic simulations, are represented as stars. 76

5.5 Relation between $k_y\rho_i$ and $k_\perp^{\mathrm{DR}}$ as a function of the radial position for a wide range of $k_\perp^{\mathrm{DR}}$. These plots are the result of evaluating expression (5.2) at $(\theta, \zeta) = (0, 0)$ considering the T_i profiles represented in figure 5.2 for the low (left) and high (right) density scenarios. The white squares represent the perpendicular wavenumbers measured by the DR system at each radial location. 77

5.6 Time evolution of $(\delta n)^2(k_y\rho_i = 0.8)$ at $r_0/a = 0.6$ in the high density scenario. The range considered for the time-average is represented by the shadowed area and the mean value of this quantity is indicated with the horizontal dashed line. 78

5.7 k_y spectrum of the time-averaged squared density fluctuations, $\langle(\delta n)^2\rangle_t$, obtained with `stella` for the low (left) and high (right) density scenarios. The dashed vertical lines indicate the wavenumber measured by the DR system, $k_\perp^{\mathrm{DR}}$, at each radial position. 79

5.8 Squared amplitude of the density fluctuations as a function of the radial coordinate for the low (light blue circles) and high (dark blue triangles) density scenarios. Left: Numerical results of $(\delta n)^2_{\mathrm{DR}}$ obtained with `stella`. The error bars represent the standard deviation from the mean value evaluated over the saturated nonlinear phase. Right: backscattered power measured by the DR system. 80

5.9 Amplitude of the density fluctuations integrated over k_x and k_y computed with `stella` as a function of the radial coordinate for the low (light blue circles) and high (dark blue triangles) density scenarios. 81

5.10 $(\delta n)^2_{\mathrm{DR}}$ as a function of the poloidal coordinate θ for a fixed $\zeta = 0$ for the low (left) and high (right) density scenarios. Computed as an interpolation of the $(\delta n)^2_{\mathrm{DR}}$ calculated for the bean (circles) and triangular (squares) flux tubes. The shadowed region shows approximately the maximum deviation of the DR measurement position from $\theta = 0$. 81
5.11 Frequency spectra of $(\delta n)^2$ for the low (top) and high (bottom) density scenarios computed with `stella` as function of k_y. 83
5.12 Density spectra of $\delta\check{n}_{\mathrm{DR}}$ computed with `stella` for the low (top) and high (bottom) density scenarios for the case $k_y = k_y^{\mathrm{DR}}$. 84
5.13 Normalized amplitudes $|\delta\check{v}^{\mathrm{ZF}}_{\perp\omega}|$ computed with `stella` and represented as a function of the frequency ω for the low (top) and high (bottom) density scenarios. The dashed vertical lines indicate the frequency ω_0 such that $|\delta\check{v}^{ZF}_{\perp\omega_0}| < \max(|\delta\check{v}^{ZF}_{\perp\omega}|)/2$ for all $\omega > \omega_0$. 86
5.14 Nonlinear frequency spectrum of $\sum_{k_x}\langle\widehat{\varphi}^{tb}_{k_x k_y}\rangle$ for the low (top) and high (bottom) density scenarios computed with `stella` as a function of k_y. The amplitudes $|\check{\varphi}_\omega|$ are normalized to their maximum value at each k_y. The white dots are the results of linear k_y scans assuming $k_x = 0$ and the vertical dashed lines indicates de value that k_y^{DR} takes in each situation. 87
5.15 Nonlinear results of $\overline{|\varphi_\omega|}$ for the low (top) and high (bottom) density scenarios, evaluated at $k_y\rho_i = 0.6$. The linear result for the mode $(k_x\rho_i, k_y\rho_i) = (0, 0.6)$ is represented as a black triangle in every situation. 88
5.16 Normalized $(\varphi^{tb})^2_{\mathrm{DR}}$ as a function of ζ, computed with `stella` for the low (left) and high (right) density scenarios. The insets show the results corresponding to $r_0/a = 0.5$, together with the magnetic field strength as a gray solid line. . 89
5.17 Normalized $(\varphi^{tb})^2_{\mathrm{DR}}$ for the linearly unstable mode with $k_x = 0$ as a function of ζ, computed with `stella` for the low (left) and high (right) density scenarios. 89

List of Tables

Table **Page**

2.1 List of input parameters required for a standard simulation performed with `stella`. The first column lists the variable names as used in the `stella` input file; the second column corresponds to the associated physical quantities and the third column provides a brief description of the relationship between each physical quantity and its respective input parameter. 35

3.1 Parameters of the nonlinear simulations performed for the radial position $r_0/a = 0.7$ of the standard configuration of W7-X. From left to right: twist-and-shift boundary condition choice; maximum considered value of k_x and k_y; number of simulated values of k_x; number of simulated values of k_y; ratio between the grid spacing in k_x and k_y or, equivalently, between $|k_x|^{\min}$ and $k_y^{\min}$; value of the time-averaged ion heat flux and CPU time required to run the simulation. 45

3.2 Parameters of the nonlinear simulations performed for the radial position $r_0/a = 0.5$ of the standard configuration of W7-X. From left to right: twist-and-shift boundary condition choice; maximum considered value of k_x and k_y; number of simulated values of k_x; number of simulated values of k_y; ratio between the grid spacing in k_x and k_y or, equivalently, between $|k_x|^{\min}$ and $k_y^{\min}$; value of the time-averaged ion heat flux and CPU time required to run the simulation. 46

3.3 Parameters of the nonlinear simulations performed for the radial position $r_0/a = 0.35$ of the standard configuration of W7-X. From left to right: twist-and-shift boundary condition choice; maximum considered value of k_x and k_y; number of simulated values of k_x; number of simulated values of k_y; ratio between the grid spacing in k_x and k_y or, equivalently, between $|k_x|^{\min}$ and $k_y^{\min}$; value of the time-averaged ion heat flux and CPU time required to run the simulation. 48

4.1 Basic quantities of the magnetic configuration at the radial position selected for the simulations. From left to right: minor radius; major radius; selected radial position; reference magnetic field given by (2.47); rotational transform and global magnetic shear. 52
4.2 Set of parameters used in each test. From left to right: flux tube, minimum and maximum number of N_{fp}, normalized ion temperature and density gradients, number of divisions in the grid of $v_{||}$ and μ, time step size and quantities compared with both codes. 56
4.3 Parameters used by `stella` and `GENE` to define the flux tube in test 5. From left to right: number of modes in the radial (N_{k_x}) and binormal (N_{k_y}) directions; smallest positive wavenumber in the radial ($|k_x|^{\min}$) and binormal ($k_y^{\min}$) directions. 66
4.4 Time required to run the nonlinear simulations with `GENE` in the bean flux tube and with `stella` in the bean and triangular flux tubes. From left to right: simulation wall-clock time in hours, number of processors and total CPU time in hours. 69

5.1 Local parameters used in the simulations at each radial position for the low and high density scenarios. From left to right: density, normalized density gradient, ion temperature, normalized ion temperature gradient, electron temperature, normalized electron temperature gradient and perpendicular wavenumber measured by the DR system. 77

Resumen

En esta tesis, titulada *Simulaciones de turbulencia en plasmas del stellarator Wendelstein 7-X*, abordamos aspectos fundamentales de la turbulencia en plasmas de fusión en geometrías de tipo stellarators. En particular, tras introducir el formalismo girocinético empleado para estudiar la turbulencia en estos plasmas, estudiaremos aspectos relacionados con la conexión entre la teoría y los resultados experimentales. En este contexto, nuestros dos principales objetivos son la correcta verificación del código girocinético `stella` en la geometría del stellarator Wendelstein 7-X (W7-X) y la comparación de medidas experimentales obtenidas en la primera campaña experimental de este dispositivo con los resultados obtenidos con el código. Tras esto, además se ofrecen predicciones que serán de gran utilidad para comparaciones con futuros experimentos en este dispositivo. Esta tesis se estructura de la siguiente forma:

El capítulo 1 ofrece una introducción general en la que se exponen las características fundamentales de la fusión nuclear por confinamiento magnético, enfatizando las diferencias clave entre los dos principales tipos dispositivos de fusión toroidal: tokamaks y stellarators. Además, se resalta la creciente relevancia del estudio del transporte turbulento en los stellarators, siendo este el producido por microinestabilidades que se forman a partir de fluctuaciones en el plasma con longitudes de onda del orden del girorradio y con frecuencias mucho menores que la girofrecuencia. El aumento en el interés por el estudio de este canal de transpote es motivado por los resultados obtenidos en las primeras campañas experimentales del stellarator optimizado neoclásicamente Wendelstein 7-X, en los cuales se ha identificado que el transporte turbulento es la principal fuente de pérdidas de energía, partículas y momento en este dispositivo.

En el capítulo 2 se introduce el sistema de ecuaciones girocinéticas, el cual es usado para modelar la turbulencia en plasmas. Las ecuaciones se presentan de una manera general, particularizándose posteriormente para la geometría de un *tubo de flujo*, que es el dominio computacional usado en los capítulos siguientes para resolver el sistema de ecuaciones girocinéticas con el código `stella`. Al concluir el capítulo, se describe

brevemente cómo el código `stella` resuelve el sistema, haciendo énfasis en su método mixto explícito-implícito que significa una gran ventaja con respecto a los usados en otros códigos girocinéticos. Además, se incluye una detallada descripción de los parámetros de entrada necesarios para la correcta realización de una simulación.

El capítulo 3 incluye la primera contribución significativa de esta tesis: la implementación de las condiciones de contorno *stellarator symmetric* twist-and-shift en el código `stella`. Esta implementación resulta fundamental, ya que las condiciones de contorno previamente disponibles requerían un uso excesivo de recursos computacionales para simular correctamente tubos de flujo en las superficies internas del stellarator W7-X, llegando incluso a imposibilitar la simulación en algunas de ellas. Dado que uno de nuestros principales objetivos es comparar los resultados obtenidos numéricamente con datos experimentales, es esencial poder simular en estas superficies con precisión. Tras la correcta implementación de estas nuevas condiciones de contorno, se proporciona una serie de comparaciones que evidencian claramente las ventajas de su uso.

Ante el creciente interés en el estudio de la turbulencia en stellarators, en el capítulo 4 se introduce un caso de referencia diseñado para la futura verificación de códigos girocinéticos en estas geometrías. Este caso de referencia, publicado en [1], incluye una serie detallada de pruebas en la geometría del stellarator W7-X, como la simulación lineal de inestabilidades de gradiente de temperatura iónica (ITGs), modos de electrones atrapados (TEMs) y modos zonales en distintos tubos de flujo, así como la simulación no lineal de ITGs. Además, hemos evaluado este caso de referencia utilizando los códigos `stella` y `GENE`, lo que ha permitido la correcta verificación del código `stella` en la simetría stellarator.

Con el código `stella` verificado en la geometría de W7-X, en el capítulo 5 se presenta una comparación entre las medidas experimentales obtenidas en W7-X y los resultados obtenidos numéricamente, así como predicciones a tener en cuenta en futuras campañas experimentales. En particular, analizamos cantidades turbulentas que pueden compararse directamente con las mediciones experimentales realizadas por el reflectómetro Doppler instalado en W7-X. El estudio se centra en cinco posiciones radiales correspondientes a dos descargas de la primera campaña experimental de este dispositivo. En primer lugar, se realizan simulaciones no lineales para comparar la amplitud de las fluctuaciones de densidad para los números de onda estudiados con el diagnóstico. Los resultados muestran que tanto las mediciones experimentales como los resultados numéricos abarcan un rango de 15 dB y exhiben un crecimiento monótono con la coordenada radial. Sin embargo, se detectan algunas discrepancias entre los resultados

numéricos y experimentales, las cuales podrían atribuirse a las limitaciones actuales del código, como la omisión de colisiones o la simulación de tubos de flujo en vez de la completa simulación de las superficies magnéticas. Estas limitaciones serán abordadas en estudios futuros. Además, en este capítulo se incluyen predicciones para las frecuencias de las fluctuaciones de densidad y de flujos zonales, considerando las mismas posiciones radiales y descargas que en la comparación anterior. Se espera que las frecuencias de las fluctuaciones de densidad presenten sus mayores amplitudes en torno a los 10 kHz, con una caída abrupta más allá de los 500 kHz. En cuanto a las fluctuaciones de los flujos zonales, se prevé que estén dominadas por frecuencias inferiores a 20 kHz, con picos por debajo de los 10 kHz. Los resultados mostrados en este capítulo están recopilados en [2].

Summary

In this thesis, titled *Simulations of turbulence in the stellarator Wendelstein 7-X plasmas*, we address fundamental aspects of fusion plasma turbulence in stellarator geometry. In particular, after introducing the gyrokinetic formalism used to study turbulence in these plasmas, we will examine aspects related to the connection between theoretical predictions and experimental results. In this context, our two main objectives are the correct verification of the gyrokinetic code `stella` in the geometry of the Wendelstein 7-X stellarator (W7-X) and the comparison of experimental measurements obtained during the first experimental campaign of this device with the results obtained from the code. This thesis is structured as follows:

Chapter 1 provides a general introduction that outlines the fundamental characteristics of magnetic confinement fusion, highlighting the key differences between the two main concepts of toroidal fusion devices: tokamaks and stellarators. Additionally, the increasing relevance in the study of turbulent transport in stellarators, produced by microinstabilities that arise from fluctuations in the plasma with wavelengths on the order of the gyroradius and with frequencies much lower than the gyrofrequency, is highlighted. The growing interest in studying this transport channel is motivated by the results obtained in the first experimental campaigns of the neoclassically optimized stellarator Wendelstein 7-X, where it has been identified that turbulent transport is the main source of energy, particle, and momentum losses in this device.

Chapter 2 introduces the gyrokinetic system of equations, which is used to model turbulence in plasmas. The equations are presented in a general manner and then particularized for the geometry of a *flux tube*, which is the computational domain used in the following chapters to solve the gyrokinetic equation system with the code `stella`. At the end of the chapter, a brief description of how `stella` solves the system is provided, with emphasis on its mixed explicit-implicit method, which represents a significant advantage over those used in other gyrokinetic codes. Additionally, a detailed description of the input parameters needed for the correct performance of a simulation is included.

Chapter 3 includes the first significant contribution of this thesis: the implementation of *stellarator symmetric* twist-and-shift boundary conditions in the code `stella`. This implementation is crucial given that the previously available boundary conditions required an excessive amount of computational resources to accurately simulate flux tubes located at the inner surfaces of the stellarator Wendelstein 7-X, being the simulation at some of these surfaces even impossible. Since one of our main objectives is to compare the numerical results with experimental measurements, it is essential to be able to simulate at these surfaces accurately. After the successful implementation of these new boundary conditions, a set of comparisons that clearly demonstrate the advantages of their use are provided.

Given the growing interest in the study of turbulence in stellarators, chapter 4 introduces a benchmark case designed for the future verification of gyrokinetic codes in these devices. This benchmark case, published in [1], includes a detailed set of tests in the geometry of the Wendelstein 7-X stellarator, such as the linear simulation of ion-temperature-gradient (ITG) instabilities, trapped-electron-modes (TEMs), and zonal flows in different flux tubes, as well as the nonlinear simulation of ITGs. Additionally, we have evaluated this benchmark case using the codes `stella` and `GENE`, meaning the correct verification of the code `stella` in the stellarator geometry.

After the verification of the code `stella` in the geometry of W7-X, chapter 5 presents a comparison between experimental measurements obtained in W7-X and the results obtained numerically, as well as predictions to be considered in future experimental campaigns. In particular, we analyze turbulent quantities that can be directly compared with experimental measurements obtained with the Doppler reflectometer system (DR) installed on W7-X. The study focuses on five radial positions corresponding to two discharges from the first experimental campaign of this device. First, nonlinear simulations are performed to compare the amplitude of density fluctuations for the wavenumbers studied with the diagnostic. The results show that both experimental measurements and numerical results cover a range of 15 dB and exhibit a monotonic increase with the radial coordinate. However, some discrepancies are detected between the numerical and experimental results, which could be attributed to the current limitations of the code, such as the omission of collisions or the simulation of flux tubes instead of the complete simulation of magnetic surfaces. These limitations will be addressed in future studies. Additionally, this chapter includes predictions for the frequencies of density fluctuations and zonal flows, considering the same radial positions and discharges as in the previous comparison. It is expected that the frequencies of density fluctuations will present their

highest amplitudes around 10 kHz, with a sharp drop beyond 500 kHz. As for the zonal flow fluctuations, it is predicted that they will be dominated by frequencies below 20 kHz, with peaks below 10 kHz. The results shown in this chapter can be found in [2].

CHAPTER 1

Introduction

1.1. Magnetic confinement fusion

Thermonuclear fusion is a promising and potential future energy source free of long-term radioactive waste. Its fuels are expected to be deuterium, which is abundant on Earth, and tritium, which is projected to be sustainably bred from lithium in future fusion reactors. This positions nuclear fusion as one of the power sources capable of ensuring large-scale energy supply in the coming centuries.

The physical principle on which thermonuclear fusion is founded is the equivalence between mass and energy. In nuclear reactions the difference in mass between the reactants and the products, known as *mass defect*, can be expressed as

$$\Delta E = (m_0 - m_f)c^2, \tag{1.1}$$

where m_0 denotes the total mass of the reactants and m_f that of the products, with c the speed of light. Therefore, in order to get energy release in a fusion reaction, the total binding energy of the reactants must exceed that of the products. Roughly, as it can be observed in figure 1.1 (left), this requirement restricts the process to nuclei with masses less than that of iron, the most stable element in terms of nuclear stability. Notably, the largest differences in binding energy per nucleon are observed in the lighter elements, particularly between hydrogen and helium.

Among fusion reactions involving hydrogen nuclei, the one with the largest reaction rate at lower temperatures is

$$\mathrm{D} + \mathrm{T} \longrightarrow {}^4_2\mathrm{He} + n + 17.58\ \mathrm{MeV}, \tag{1.2}$$

as illustrated in figure 1.1 (right). As a consequence, this reaction is the one intended for the operation of future fusion reactors. During this reaction, tritium (T) and deuterium

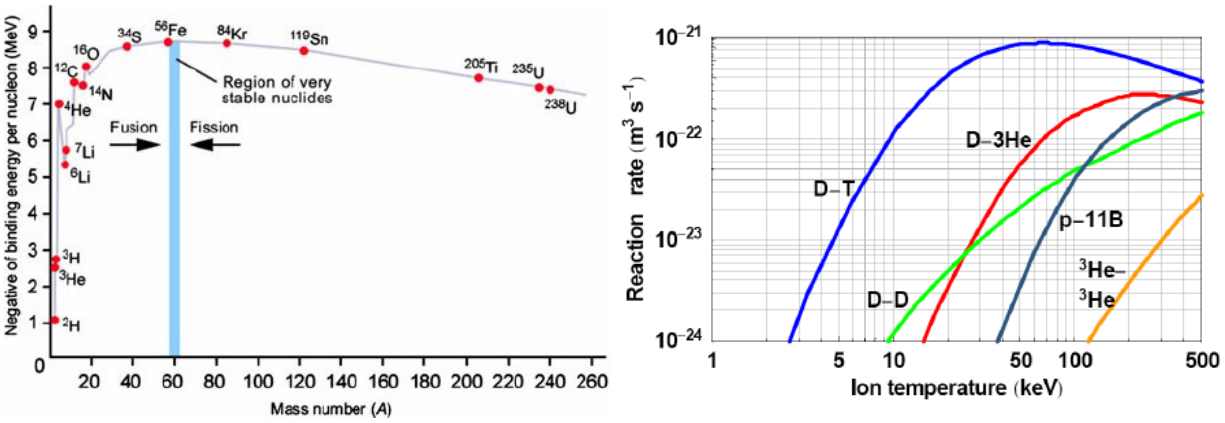

Figure 1.1: Left: average binding energy per nucleon in MeV as a function of the mass number. Figure taken from [3]. Right: reaction rates for different hydrogen isotopes to fuse as a function of the temperature (on logarithmic scale) required for their occurance. Figure taken from [4].

(D) react to produce a fast alpha particle (a fully ionized helium nucleus) with 3.52 MeV of the energy generated in the reaction and a neutron with the remaining energy of 14.06 MeV. The main challenge for this reaction to occur lies in overcoming the electric repulsion between the nuclei, which requires a significant amount of kinetic energy. Specifically, as depicted in figure 1.1 (right), this energy is of the order of 10 keV[1] which is equivalent to temperatures of the order of 10^8 K. At these temperatures, matter exists in plasma state. A brief and concise description of plasma is given at the beginning of section 2.1.

At the temperatures required for fusion reactions to occur, particles within the plasma would escape from any container in a very short time, typically of the order of milliseconds. Due to their charged nature, magnetic fields can be applied to confine these particles, which is the main principle on which magnetic confinement fusion is based.

Magnetic confinement takes advantage of the Lorentz force, which causes charged particles to follow helical trajectories around magnetic field lines [5]. The radius of these helical paths, ρ_s, is known as gyroradius and expressed as

$$\rho_s = \frac{v_\perp}{\Omega_s}, \tag{1.3}$$

where $v_\perp$ represents the component of the velocity of the particles that is perpendicular

[1]In this thesis, as well as in the literature on plasma physics and nuclear fusion, temperature is usually expressed in energy units, typically in eV or keV. That is, what would actually be $k_B T$ is denoted as T, omitting the Boltzmann constant, k_B, in this notation.

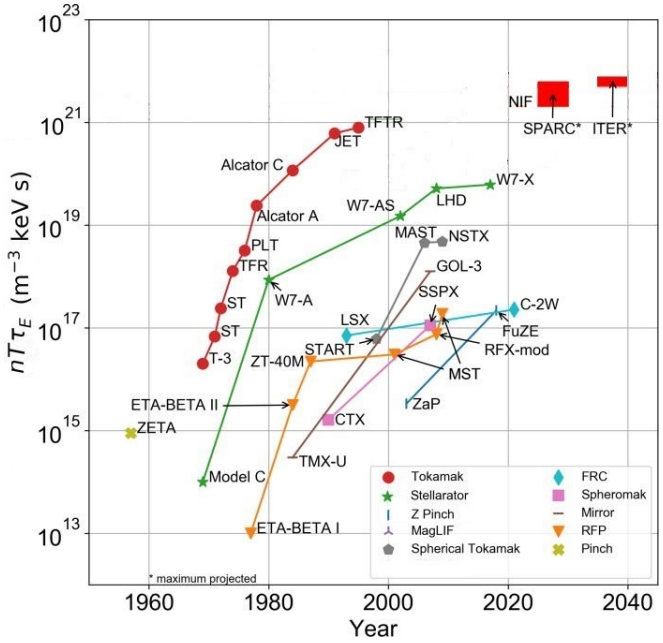

Figure 1.2: Time evolution of the highest experimental triple product ($nT\tau_E$) obtained for multiple fusion experiments. Data for devices not yet built are projections. Figure adapted from [6].

to the magnetic field and Ω_s stands for the gyrofrequency

$$\Omega_s = \frac{q_s B}{m_s}, \tag{1.4}$$

with B the magnetic field strength, q_s the charge of species s and m_s its mass. Therefore, since the gyroradius is inversely proportional to the the magnetic field strength, by generating an intense magnetic field, charged particles are compelled to move along magnetic field lines, increasing the time it takes for them to escape in the direction across magnetic field lines. Specifically, if the magnetic field is strong enough such that ρ_s is significantly smaller than the device size, we talk about a *strongly magnetized plasma*.

Future fusion reactors should desirably achieve plasma ignition, which is the self-sustainment of nuclear fusion reactions by the energy relased in the process, in particular, by the transfer of the energy carried by the fast alpha particle back to the reactans. In order to achieve that state, the product of the plasma density (n), temperature (T) and energy confinement time (τ_E), must exceed approximately a certain threshold of

$$nT\tau_E \gtrsim 10^{21} \text{ keV s m}^{-3}, \tag{1.5}$$

known as the Lawson criterion [7]. The evolution of the product $nT\tau_E$, known as *triple product*, over the decades is illustrated in figure 1.2, which compiles data from various

fusion experiments across different magnetic confinement fusion concepts. Among the devices shown, tokamaks and stellarators have consistently achieved the highest triple product in each era depicted, making them the most promising magnetic confinement devices. A more in-depth description of tokamaks and stellarators is given in the next section.

1.2. Tokamaks and stellarators

From a macroscopic description, plasmas can be analyzed as charged fluids and, therefore, they must follow the equations of magneto-hydrodynamics (MHD). In particular, from the ideal MHD force balance equation we can infer that an equilibrium must be achieved between the expansion forces induced by the gradients of plasma pressure, $p = nT$, and those resulting from the interaction between the magnetic field, $\mathbf{B}$, and the electric currents, $\mathbf{J}$, present in the plasma

$$\mathbf{J} \times \mathbf{B} = \nabla p, \tag{1.6}$$

where the plasma has been assumed to be an ideal electric conductor which is close to thermodynamic equilibrium and in steady-state. Equation (1.6) imposes that both vectors $\mathbf{B}$ and $\mathbf{J}$ should lie on surfaces of constant pressure since $\mathbf{J} \cdot \nabla p = \mathbf{B} \cdot \nabla p = 0$. These surfaces are known as *magnetic surfaces*. We will discuss magnetic confinement concepts where magnetic field lines generate nested toroidal[2] magnetic surfaces, as sketched in figure 1.3.

The magnetic fields suitable to maintain the plasma in an ideal MHD equilibrium must have both toroidal (defined as the component in the direction of the major circumference of the torus) and poloidal (defined as the component in the direction of the minor circumference of the torus) components. These directions are represented in figure 1.3. The presence of both components in the magnetic field gives rise to the rotational transform (ι), which is a quantity that can be understood as the number of poloidal turns the magnetic field makes per toroidal turn (a more technical description of this quantity is given in section 2.3). While in magnetic confinement devices the toroidal component of the magnetic field is created by external electromagnetic coils, there are three different approaches to create the poloidal magnetic field, or to generate ι, in these geometries [8]:

[2] According to the Poincaré-Hopf index theorem, the only closed surface that admits non-vanishing smooth vector fields is the torus, hence magnetic surfaces should present toroidal topology to avoid singular points in the magnetic field.

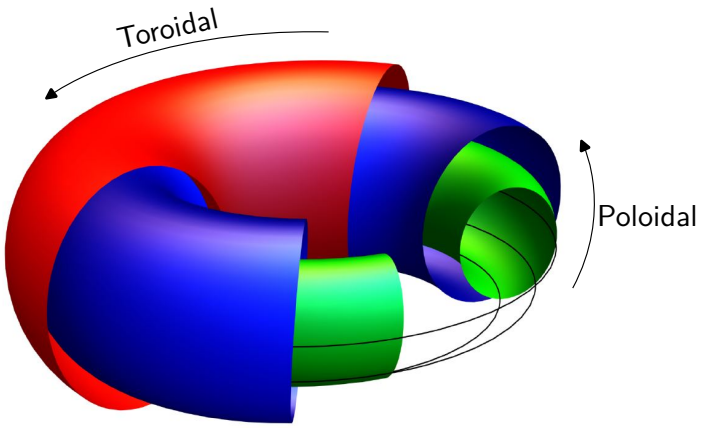

Figure 1.3: Sketch of different magnetic surfaces, together with some magnetic field lines. The toroidal and poloidal directions are sketched.

- creating the poloidal magnetic field by a toroidal electric current,
- rotating the poloidal cross-section of stretched magnetic surfaces around the torus,
- making the magnetic axis non-planar.

Tokamaks and stellarators are the two main concepts for a magnetic confinement fusion reactor, and differ on how the poloidal magnetic field is generated.

In tokamaks (represented in figure 1.4 (left)), the first approach is implemented, twisting the magnetic field through an external current. This choice allows the set of external coils and the confined plasma to be axisymmetric. This setup presents considerable advantages from an engineering perspective, particularly in the fabrication of the coils and the vacuum chamber where the plasma is confined. However, since in these devices the magnetic field generation is achieved through a transformer-like process, with the confined plasma acting as the secondary coil, they are limited to a pulsed operation. In addition, the significant amount of external time-varying electric current required to create the poloidal magnetic fields makes tokamaks vulnerable to current-driven instabilities, which can lead to disruptions, i.e., abrupt losses of the confined particles and energy. Examples of tokamaks include the Joint European Torus (JET) [9] located in Culham (England), the Axially Symmetric Divertor Experiment (ASDEX-Upgrade) [10] in Garching (Germany), and the under-construction International Thermonuclear Experimental Reactor (ITER) in Cadarache (France). On the other hand, stellarators usually rely on the second and the third methods, rotating the poloidal cross-section of stretched magnetic surfaces around the torus or making the magnetic axis non-planar,

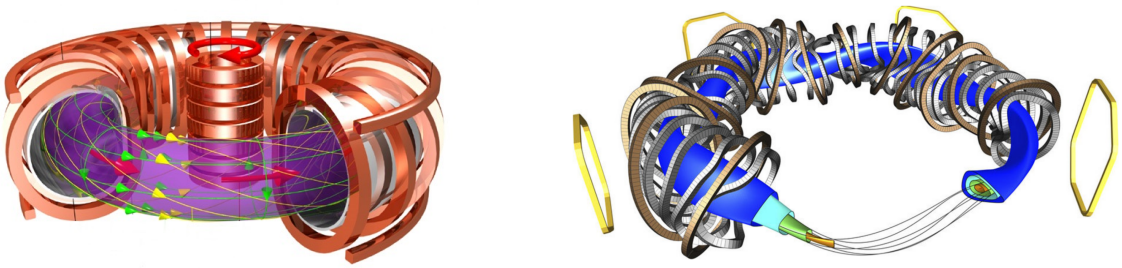

Figure 1.4: Layout of different magnetic confinement devices. Left: a generic tokamak, where the twisted magnetic field is represented with green arrows. The axisymmetric set of external coils is also depicted. Figure adapted from [14]. Right: the stellarator Wendelstein 7-X (W7-X), where some nested magnetic flux surfaces are represented (dark blue, light blue, green and orange) together with the magnetic field lines that lie on the green surface. The complex 3-D geometry of the external coils is clearly depicted. Figure taken from [15].

which imply that the magnetic configuration of stellarators is three-dimensional. The inherent 3-D geometry of the coils makes stellarators complex to build and causes the shape of the plasma to lack any axis of symmetry. However, this intricate geometry allows to twist the magnetic field without the need of an external current, resulting in a disruption-free operation for stellarators with the ability to operate in steady state. Among the current stellarators, some examples include TJ-II [11], which is located in Madrid (Spain), the Large Helical Device (LHD) [12], which is located in Toki (Japan) or Wendelstein 7-X (W7-X) [13], which is located in Greifswald (Germany) and represented in figure 1.4 (right).

1.3. The neoclassically optimized stellarator Wendelstein 7-X (W7-X) and the importance of turbulence

Concisely, in magnetically confined plasmas, the transport and losses of particles, energy and momentum can be categorized into three different channels: classical, neoclassical and turbulent transport. Classical transport solely considers Coulomb collisions and it is typically negligible both in tokamaks and stellarators. On the other hand, neoclassical transport also incorporates the effect of the magnetic field curvature and its inhomogeneities. While at low collisionality the contribution of this channel tends to be small in tokamaks, it has traditionally been the major source of concern at the core of stellarators. Lastly, turbulent transport accounts for the transport driven by microinstabilities, which arise from fluctuations of the plasma electromagnetic fields with frequencies much

lower than the gyrofrequency, Ω_s, of the plasma species and length scales on the order of their gyroradius, ρ_s. This channel of transport is the most relevant in tokamaks, whereas it has been explored in less detail in stellarators due to the traditional predominance of neoclassical transport in them.

The concept of neoclassically optimized stellarators has emerged with the objective of minimizing neoclassical losses. Wendelstein 7-X [13], in operation since 2015, is the first large stellarator optimized with respect to neoclassical transport. In figure 1.4 (right) we can observe some magnetic surfaces of this device alongside part of its set of coils, which consists on 50 non-planar and 20 planar superconducting coils. By appropriately choosing the currents in the coil system, this flexible set of planar and non-planar coils allows a large variety of magnetic fields conforming different *magnetic configurations*. For a comprehensive overview of the W7-X configuration space, we refer the reader to [16].

The optimization of W7-X with respect to neoclassical transport [17] has involved a systematic reduction of the effective ripple ϵ_{eff}, which is a measure of the effect of the 'helical' ripple[3] on the behaviour and confinement of particles in a stellarator. This reduction is appreciated in figure 1.5 (left), where we show the effective ripple values for two different configurations of W7-X and LHD as a function of a normalized coordinate that labels different magnetic surfaces. In particular, the highest triple product values (see expression (1.5)) in stellarators has been achieved with the two W7-X configurations shown in this figure. They are the so-called *standard* (line b), in which all planar coil currents are set to zero and the non-planar coil currents are set to the same value, and *high-mirror* (line c), in which the toroidal mirror ratio[4] is significantly higher. Since neoclassical energy fluxes in the $1/\nu$ regime scale with $\epsilon_{eff}^{3/2}$ [18], reducing ϵ_{eff} is a natural way of decreasing neoclassical losses in stellarators. Indeed, as observed in figure 1.5 (right), where the normalized neoclassical energy losses are represented for the same configurations depicted in 1.5 (left), the normalized neoclassical energy fluxes in W7-X are significantly lower than those in LHD.

This optimization has been successfully proven experimentally in the first experimental campaigns of W7-X [20, 21]. However, the results obtained in these experiments have made it evident that, in general, the total particle and energy transport exceeds the predictions made by neoclassical theory [22]. As it can be observed in figure 1.6, there is

[3]The helical ripple of the magnetic field quantifies the strength of its inhomogeneities.

[4]The toroidal mirror ratio is defined as $b_{01} \equiv B_{01}/B_{00}$ in a Fourier representation B_{mn} of the magnetic field strength, where m and n are, respectively, poloidal and toroidal mode numbers. In W7-X, depending on the configuration, this ratio can reach values up to $b_{01} \sim 0.2$.

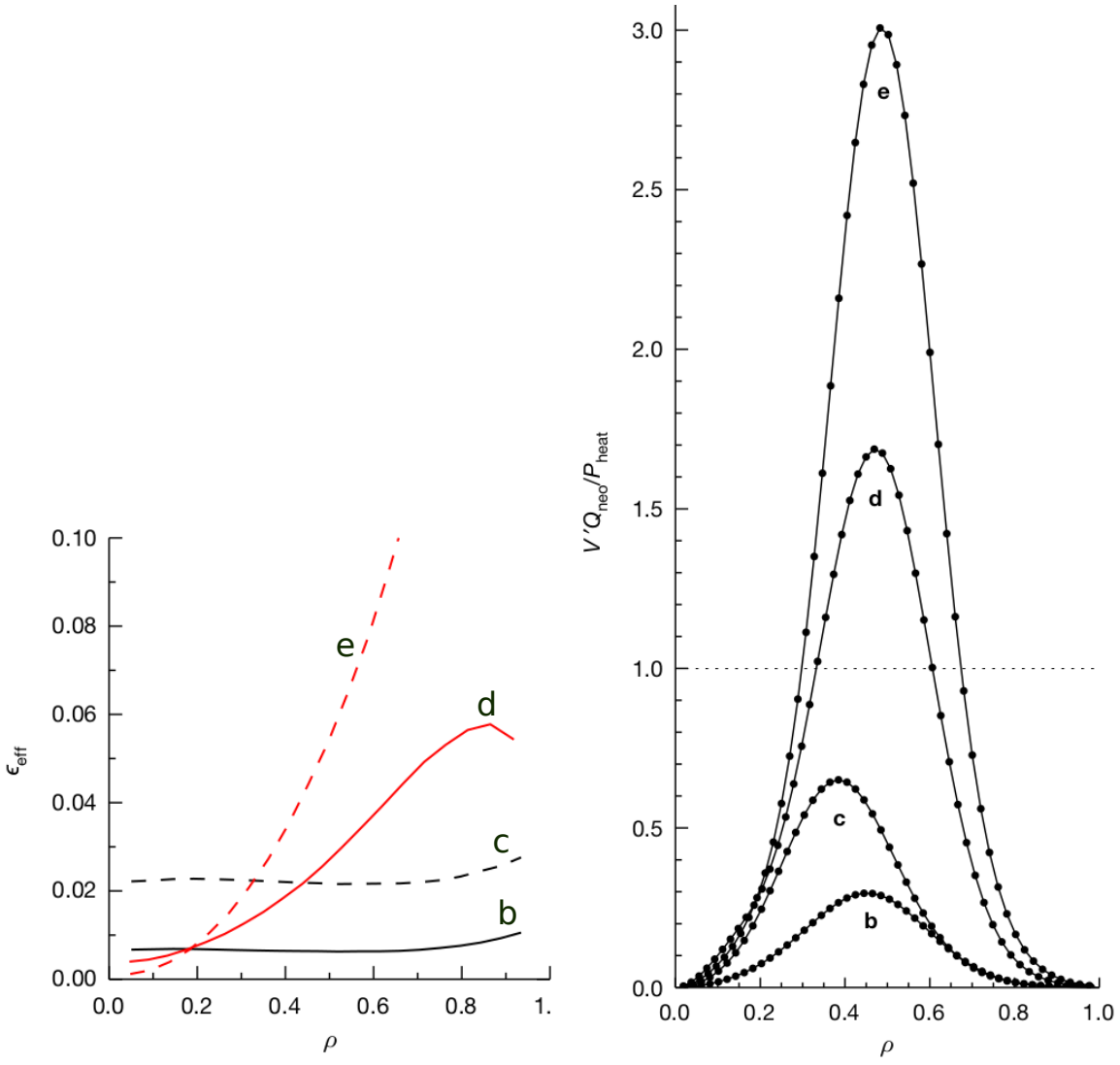

Figure 1.5: Left: effective ripple as a function of a normalized radial coordinate, labeling different magnetic surfaces, for two different W7-X configurations (standard (b) and high-mirror (c)) and two different LHD configurations (d,e). Right: neoclassical energy losses, computed with the code DKES [19] and normalized to the heating power as a function of the same normalized radial coordinate for the configurations represented in the left figure. Plots taken from [17].

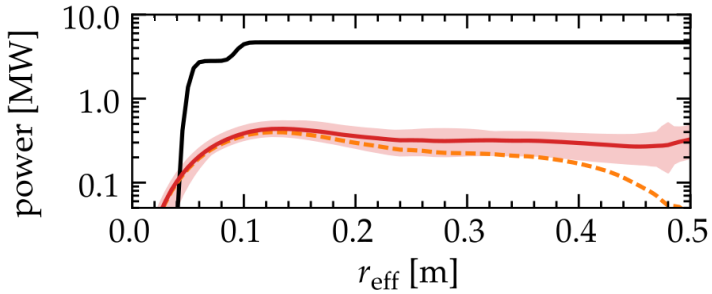

Figure 1.6: Power balance analysis for a gas-fuelled discharge in W7-X. The input power is represented as a solid black line and the sum of neoclassical ion and electron energy fluxes (dotted orange line) and radiated power is represented as a solid red line. These results are given as a function of an effective radius, which labels different magnetic surfaces. Figure adapted from [22].

a significant gap —approximately of a factor of ten— between the sum of the neoclassical fluxes (for both ions and electrons) combined with the radiated power, and the input power. Thus, the neoclassical heat flux alone is not sufficient to explain the total losses. This energy and particle transport has been attributed to the turbulent channel, turning turbulent transport into an essential mechanism to understand and predict how plasmas perform in this device. This disagreement between the experimental losses and those predicted by neoclassical theory has motivated much work in the study of turbulence, modelled by gyrokinetic theory.

1.4. Scope of this thesis

In this thesis, we have focused on the numerical study of electrostatic turbulence described within the framework of the gyrokinetic theory [23], which will be introduced in chapter 2. As will be discussed throughout this work, we have addressed two fundamental aspects related to the theory and its connection to experiments: the benchmark (or verification) of gyrokinetic codes and the validation of their predictions against experimental measurements. Specifically, the code `stella` [24] has been benchmarked against the code `GENE` [25] in W7-X geometry. Notably, at the beginning of this thesis, `stella` had recently been developed and had not yet been verified against any other code for stellarator geometry. This verification has been carried out in the form of a comprehensive benchmark, which includes different tests thought as a reference case against which present and future stellarator codes can be tested and benchmarked. Following this verification, which will be explained in detail in chapter 4, we have used `stella` to provide, for the first time in W7-X, a detailed comparison between the numerical characteriza-

tion of turbulent fluctuations in this device and the existing experimental measurements, particularly those obtained with a Doppler Reflectometer installed in W7-X. In order to asses this comparison, given in chapter 5, it has been necessary to implement a new set of boundary conditions in the code, which allow us to simulate flux tubes located at the inner surfaces of W7-X, as carefully described in section 3. Finally, after the verification and validation of `stella`, we have employed the code to predict certain quantities that will be valuable for comparisons with future experimental analyses of W7-X, as detailed in the final part of chapter 5.

CHAPTER 2

Gyrokinetic description of a fusion plasma

In this chapter we will introduce the gyrokinetic system of equations, which is used for modelling microturbulence in strongly magnetized plasmas. Specifically, our focus will be on the electrostatic and collisionless version of these equations. Once the gyrokinetic equations are introduced, we will particularize them to the flux tube geometry, which is the computational domain in which the code `stella`, used in the development of this thesis, solves them. Then, we will provide a brief overview of how `stella` solves the gyrokinetic system of equations, highlighting the differences between linear and nonlinear simulations. Finally, we will collect the input parameters required to run the code, establishing the correspondence between each parameter and the physical quantity it represents.

2.1. Kinetic description of plasmas

A plasma is a globally neutral ionized gas, composed of positively and negatively charged particles. The near balance between positive and negative charges makes the plasma quasi-neutral, which can be represented by the quasi-neutrality equation

$$\sum_s q_s n_s = 0. \tag{2.1}$$

This condition implies that, on the relevant scales for our study —meaning for frequencies smaller than the plasma frequency and spatial scales larger than the Debye length—, the plasma can be considered locally neutral. Furthermore, at these scales, plasmas are capable of effectively screening electric fields. As a consequence, the particles within the plasma respond collectively to any perturbations, thereby exhibiting collective effects [26].

Each particle in the plasma can be characterized by its position $\mathbf{r}$ and its velocity $\mathbf{v}$. The description of fusion plasmas requires a kinetic treatment in terms of phase-space distribution functions. Specifically, each species s, where in this thesis $s = i$ stands for the main ions and $s = e$ stands for the electrons, is described by a time (t) dependent distribution function $f_s(\mathbf{r}, \mathbf{v}, t)$. The total number of particles of species s (N_s) within the system can be obtained by integrating its distribution function over the phase-space variables,

$$N_s(t) = \int f_s(\mathbf{r}, \mathbf{v}, t) \mathrm{d}^3 r \mathrm{d}^3 v. \tag{2.2}$$

In the absence of sources and sinks, the distribution function must follow the continuity equation

$$\frac{\mathrm{d}f_s}{\mathrm{d}t} = 0, \tag{2.3}$$

or, following the chain rule,

$$\frac{\partial f_s}{\partial t} + \dot{\mathbf{r}} \cdot \frac{\partial f_s}{\partial \mathbf{r}} + \dot{\mathbf{v}} \cdot \frac{\partial f_s}{\partial \mathbf{v}} = 0, \tag{2.4}$$

where a dot over a quantity indicates its differentiation with respect to t. Here, $\dot{\mathbf{v}}$ must equal the force per mass unit. If we neglect gravitational forces, the only remaining force of interest is the electromagnetic Lorentz force [27], given by the expression

$$\dot{\mathbf{v}} = \frac{q_s}{m_s} \left(-\nabla\varphi + \mathbf{v} \times \mathbf{B} \right), \tag{2.5}$$

where $-\nabla\varphi$ and $\mathbf{B}$ are, respectively, the total electric and magnetic fields, with φ the electrostatic potential. Substituting this expression into the continuity equation (2.4), we obtain the so-called Vlasov equation

$$\frac{\partial f_s}{\partial t} + \mathbf{v} \cdot \frac{\partial f_s}{\partial \mathbf{r}} + \frac{q_s}{m_s} \left(-\nabla\varphi + \mathbf{v} \times \mathbf{B} \right) \cdot \frac{\partial f_s}{\partial \mathbf{v}} = 0. \tag{2.6}$$

2.2. δf-gyrokinetic formalism

The Vlasov equation (2.6) contains information about both large and small scales. However, the focus of this thesis is to examine the effects of microturbulence, whose wavelengths are on the order of the gyroradius (1.3) and whose frequencies are much lower than the gyrofrequency (1.4). We can exploit the scale separation between the typical variation lengths of the background magnetic field, $\mathbf{B}$, and plasma profiles, and the scales of the turbulent fluctuations and treat the small-scale fluctuations of f_s and φ, denoted, respectively, by f_s^{tb} and φ^{tb}, as the unknown variables of the system.

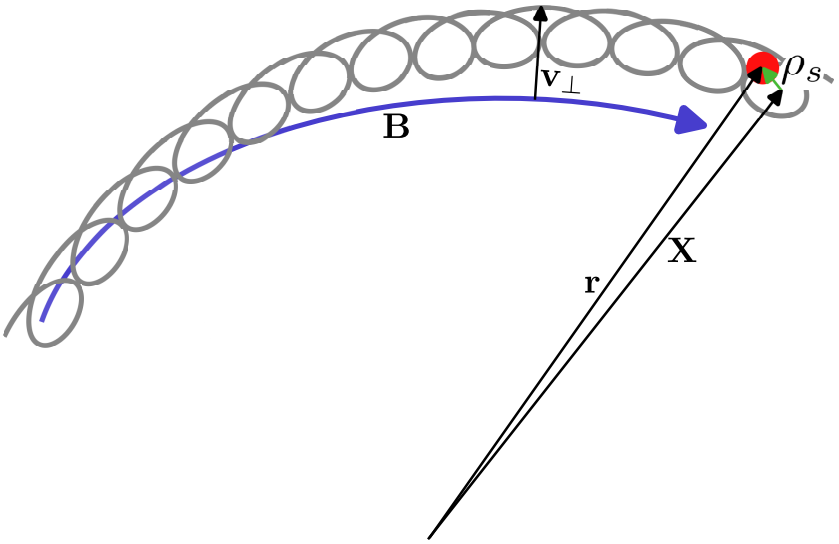

Figure 2.1: Sketch of the helical motion of a charged particle (red circle) in the presence of a non-uniform magnetic field, represented in blue. The position vector $\mathbf{r}$, the guiding-centre $\mathbf{X}$ and the gyroradius $\boldsymbol{\rho}_s$ (in green) are also included, together with the drifts in the direction perpendicular to the magnetic field, $\mathbf{v}_\perp$. The perpendicular scale is exaggerated for clarity.

Let us decompose the particle motion under the action of a time-independent magnetic field into two components: a fast, approximately circular orbit around the magnetic field, and a slower movement of the orbit's center (or guiding-center). Figure 2.1 illustrates this, showing the trajectory of a charged particle in a non-uniform, time-independent magnetic field. In this context, and as shown in figure 2.1, the position of the particle, $\mathbf{r}$, is given by

$$\mathbf{r} = \mathbf{X} + \boldsymbol{\rho}_s, \tag{2.7}$$

where $\mathbf{X}$ represents the guiding-center position and $\boldsymbol{\rho}_s = \rho_s \left(\cos\gamma \mathbf{e_2} - \sin\gamma \mathbf{e_1}\right)$ is the gyroradius vector[1] with γ the gyro-angle. The gyroradius $\boldsymbol{\rho}_s$ is perpendicular to $\mathbf{B}$ and its magnitude, known as Larmor radius, is given by (1.3). Additionally, as it can be noticed in figure 2.1, the guiding-center trajectory does not coincide with the magnetic field line due to drifts that occur on the plane perpendicular to the field.

In a strongly magnetized plasma, the parameter

$$\rho_{*s} = \frac{\rho_s}{L} \ll 1 \tag{2.8}$$

[1]Here the gyroradius is expressed in the orthonormal basis $\{\mathbf{e_1}, \mathbf{e_2}, \mathbf{B}/B\}$, where $\mathbf{e_1}$ and $\mathbf{e_2}$ are unitary vectors satisfying $\mathbf{e_1} \times \mathbf{e_2} = \mathbf{B}/B$.

can be defined, with L a characteristic length scale typically on the order of the device size. Gyrokinetic theory consists of systematically expanding the equations in this small ρ_{*s} and averaging them over the fast gyromotion, retaining only the slower timescales relevant for microturbulence. Thus, the equations are averaged over the rapid gyration to eliminate γ as a phase-space variable, reducing them from 6 to 5. This operation, known as gyro-average, is represented by $\langle\cdot\rangle_\gamma$ and defined as

$$\langle\cdot\rangle_\gamma = (2\pi)^{-1}\int_0^{2\pi}(\cdot)\mathrm{d}\gamma. \tag{2.9}$$

In what follows, we use $\{v_\parallel, \mu, \gamma\}$ as velocity coordinates, where $v_\parallel$ represents the component of the velocity parallel to $\mathbf{B}$ and

$$\mu = \frac{m_s v_\perp^2}{2B} \tag{2.10}$$

is the magnetic moment. Using these coordinates, the Vlasov equation (2.6) can be expressed as

$$\frac{\partial f_s}{\partial t} + \dot{\mathbf{X}}\cdot\nabla f_s + \dot{v}_\parallel\frac{\partial f_s}{\partial v_\parallel} + \dot{\mu}\frac{\partial f_s}{\partial \mu} + \dot{\gamma}\frac{\partial f_s}{\partial \gamma} = 0, \tag{2.11}$$

where, from now on and unless otherwise stated, every quantity is evaluated at the position $\mathbf{X}$ and ∇ represents the gradient operator $\partial/\partial\mathbf{X}$.

We gyro-average expression (2.11) and retain its terms accurate to $O\left(n_s v_{th,s}^{-2} L^{-1}\rho_{*s}\right)$, where $v_{th,s} = \sqrt{2T_s/m_s}$ is the thermal velocity. To the required accuracy we take[2]

$$\langle\dot{\mathbf{X}}\rangle_\gamma = v_\parallel\hat{\mathbf{b}} + \mathbf{v}_{Ms} + \langle\mathbf{v}_{Es}^{tb}\rangle_\gamma, \tag{2.12}$$

where we can distinguish between the parallel motion of the particle ($v_\parallel\hat{\mathbf{b}}$), with $\hat{\mathbf{b}} = \mathbf{B}/B$ an unitary vector pointing in the direction of the magnetic field, and the perpendicular drifts. Among the latter, we differentiate between the magnetic drift, $\mathbf{v}_{Ms}$, and the fluctuating $E\times B$ drift[3], $\mathbf{v}_E^{tb}$. The magnetic drift is caused by the magnetic field inhomogenities and can be divided into a magnetic curvature drift and a magnetic ∇B drift,

$$\mathbf{v}_{Ms} = \underbrace{\frac{1}{\Omega_s}\hat{\mathbf{b}}\times v_\parallel^2\boldsymbol{\kappa}}_{\text{Curvature drift}} + \underbrace{\frac{\mu}{m_s\Omega_s}\hat{\mathbf{b}}\times\nabla B}_{\nabla B\text{ drift}} \tag{2.13}$$

[2]The expressions for $\langle\dot{\mathbf{X}}\rangle_\gamma$ and $\langle v_\parallel\rangle_\gamma$ up to second order in ρ_{*s} are derived in [28].

[3]Given the objective of this thesis, we have only considered the fluctuating component of the $E\times B$ drift in (2.12), which varies on short time scales and small spatial scales. However, this quantity also possess a neoclassical analogous, which varies on long time scales and large spatial scales, and has not been considered. Formally, up to first order in ρ_{*s}, we should write $\langle\mathbf{v}_{Es}\rangle_\gamma = \mathbf{v}_E^{nc} + \langle\mathbf{v}_{Es}^{tb}\rangle_\gamma$, where $\mathbf{v}_E^{nc} = \frac{1}{B}\hat{\mathbf{b}}\times\nabla\varphi_0$ represents the neoclassical component of the $E\times B$ drift, with φ_0 the mean component of the electrostatic potential.

with $\boldsymbol{\kappa} = \hat{\mathbf{b}} \cdot \nabla \hat{\mathbf{b}}$ the magnetic curvature. Analogously, the $E \times B$ drift is caused by the combined effect of electric and magnetic fields that are not aligned,

$$\mathbf{v}_{Es}^{tb} = \frac{1}{B} \hat{\mathbf{b}} \times \nabla \phi_s^{tb}, \tag{2.14}$$

where ϕ_s^{tb} describes the fluctuating component of the electrostatic potential evaluated at the position $\mathbf{r}$,

$$\phi_s^{tb}(\mathbf{X}, \mathbf{v}, t) = \varphi^{tb}(\mathbf{X} + \boldsymbol{\rho}_s, \mathbf{v}, t). \tag{2.15}$$

As for $\langle \dot{v}_\parallel \rangle_\gamma$, up to first order in ρ_{*s} we can write

$$\langle \dot{v}_\parallel \rangle_\gamma = -\frac{\mu}{m_s} \hat{\mathbf{b}} \cdot \nabla B - \frac{q_s}{m_s} \hat{\mathbf{b}} \cdot \nabla \langle \phi_s^{tb} \rangle_\gamma + v_\parallel \boldsymbol{\kappa} \cdot \left(\mathbf{v}_{\nabla Bs} + \langle \mathbf{v}_E^{tb} \rangle_\gamma \right), \tag{2.16}$$

with $\mathbf{v}_{\nabla Bs}$ the magnetic ∇B drift defined in expression (2.13).

In addition, the use of δf-gyrokinetics allows to split the particle distribution function, f_s, into a mean component, F_s, and a turbulent one, f_s^{tb}. This is

$$f_s = F_s + f_s^{tb}. \tag{2.17}$$

With the aforementioned considerations we can introduce the gyrokinetic ordering

$$\rho_{*s} \sim \frac{\omega_s}{\Omega_s} \sim \frac{f_s^{tb}}{F_s} \sim \frac{\varphi^{tb} q_s}{T_s} \sim \frac{k_\parallel}{k_\perp} \ll 1, \tag{2.18}$$

$$\rho_{*s} v_{th,s} \sim \rho_{*s} v_\parallel \sim |\mathbf{v}_{Ms}| \sim |\mathbf{v}_{Es}^{tb}|, \tag{2.19}$$

where ω is the characteristic frequency of turbulence and $k_\parallel$ and $k_\perp$ represent, respectively, the characteristic wavenumbers of the fluctuations parallel and perpendicular to the magnetic field line.

To the lowest order in ρ_{*s}, the mean component of the distribution function of the species s is a Maxwellian distribution function, $F_M = F_{Ms}$, with

$$F_{Ms} = n_s \left(\frac{m_s}{2\pi T_s} \right)^{3/2} \exp \left[-\frac{m_s \left(v_\parallel^2/2 + \mu B/m_s \right)}{T_s} \right], \tag{2.20}$$

so that

$$\langle f_s \rangle_\gamma = F_{Ms} + g_s^{tb}, \tag{2.21}$$

with $g_s^{tb} = \langle f_s^{tb} \rangle_\gamma$. In what follows we assume derivatives of g_s^{tb} such that

$$\begin{aligned} \frac{\partial g_s^{tb}}{\partial t} &\sim \frac{g_s^{tb} v_{th,s}}{L}, \\ \hat{\mathbf{b}} \cdot \nabla g_s^{tb} &\sim \frac{g_s^{tb}}{L}, \\ \left(\nabla - \hat{\mathbf{b}} \cdot \nabla \right) g_s^{tb} &\sim \frac{g_s^{tb}}{\rho_{*s} L}. \end{aligned} \tag{2.22}$$

Analogously, we assume derivatives of the fluctuating part of the electrostatic potential, φ^{tb}, such that

$$\begin{aligned}\frac{\partial \varphi^{tb}}{\partial t} &\sim \frac{\varphi^{tb} v_{th,s}}{L},\\ \hat{\mathbf{b}}\cdot\nabla\varphi^{tb} &\sim \frac{\varphi^{tb}}{L},\\ \left(\nabla - \hat{\mathbf{b}}\cdot\nabla\varphi^{tb}\right) &\sim \frac{\varphi^{tb}}{\rho_{*s}L}.\end{aligned} \tag{2.23}$$

Retaining the gyro-averaged turbulent terms up to order $O(n_s v_{th,s}^{-2} L^{-1}\rho_{*s})$ in (2.11) we obtain

$$\begin{aligned}&\frac{\partial g_s^{tb}}{\partial t} + \left(v_\parallel \hat{\mathbf{b}}\cdot\nabla - \frac{\mu}{m_s}\hat{\mathbf{b}}\cdot\nabla B\frac{\partial}{\partial v_\parallel}\right) g_s^{tb} + \left(\mathbf{v}_{Ms} + \langle \mathbf{v}_E^{tb}\rangle_\gamma\right)\cdot\nabla g_s^{tb}\\ &\quad + \langle \mathbf{v}_E^{tb}\rangle_\gamma \cdot \left[\frac{\nabla n_s}{n_s} + \frac{\nabla T_s}{T_s}\left(\frac{m_s\left(v_\parallel^2/2 + \mu B/m_s\right)}{T_s} - \frac{3}{2}\right)\right] F_{Ms}\\ &\quad + \frac{q_s}{T_s}\left(v_\parallel\hat{\mathbf{b}} + \mathbf{v}_{Ms}\right)\cdot\nabla\langle\phi_s^{tb}\rangle_\gamma F_{Ms} = 0,\end{aligned} \tag{2.24}$$

where we have taken into account that μ is an adiabatic invariant, implying $\dot{\mu} = 0$ and that, up to first order in ρ_{*s}, f_s is independent of γ [29]. In addition, we have explicitly computed the derivatives of the Maxwellian distribution function from its definition (2.20), so that

$$\nabla F_{Ms} = \left[\frac{\nabla n_s}{n_s} + \frac{\nabla T_s}{T_s}\left(\frac{m_s(v_\parallel^2/2 + \mu B/m_s)}{T_s} - \frac{3}{2}\right) - \frac{\mu}{T_s}\nabla B\right] F_{Ms} \tag{2.25}$$

and

$$\frac{\partial F_{Ms}}{\partial v_\parallel} = -\frac{v_\parallel m_s}{T_s} F_{Ms}. \tag{2.26}$$

The gyrokinetic Vlasov equation (2.24) shows that the main sources of microinstabilities in this formalism are the temperature and density gradients, which act as source terms in the equation. These gradients can create favourable conditions for the growth of small perturbations in the plasma, potentially leading to significant instability. When the temperature gradient, ∇T, is the dominant destabilizing factor, the resulting microinstability is referred to as a *temperature-gradient-driven* mode. Conversely, if density gradients, ∇n, are the primary source, the instability is known as a *density-gradient-driven* mode.

Finally, the system which unknowns are g_s^{tb} and φ^{tb} is closed by coupling the quasi-neutrality equation (2.1) gyro-averaged under the considerations made in this section. Retaining just its turbulent terms up to first order in ρ_{*s} we can write

$$\sum_s \frac{q_s B}{m_s} \int_{-\infty}^{\infty} \mathrm{d}v_\parallel \int_0^{\infty} \mathrm{d}\mu \int_0^{2\pi} \mathrm{d}\gamma \left(g_s^{tb} - \frac{q_s \tilde{\phi}_s^{tb}}{T_s} F_{Ms} \right) = 0, \tag{2.27}$$

with $\tilde{\phi}_s^{tb} = \phi_s^{tb} - \langle \phi_s^{tb} \rangle_\gamma$ the gyrophase-dependent part of ϕ_s^{tb}.

Therefore, the electrostatic, collisionless gyrokinetic system of equations consists of equations (2.24) and (2.27).

2.3. Gyrokinetic system of equations in a flux tube

The gyrokinetic Vlasov (2.24) and quasi-neutrality (2.27) equations can be further simplified by exploiting the fact that the parallel wavenumber ($k_\parallel$) of the fluctuations of interest is much smaller than their perpendicular wavenumber ($k_\perp$), as indicated by the gyrokinetic ordering (2.18). To fully exploit this scale separation, it is advantageous to solve the gyrokinetic system of equations within a *flux tube*. A flux tube is a volume that extends over a large finite length parallel to the magnetic field direction while being relatively small in the perpendicular directions. This approach offers several advantages, focusing on the relevant spatial scales for studying microturbulence. Notably, one of its key benefits is the improved computational efficiency, as it can be found in [30], where simulations conducted in various computational domains, including the flux tube geometry, are compared.

Since a flux tube represents a volume around a magnetic field line, it is convenient to introduce coordinates adapted to this geometry. We begin by defining a set of coordinates that accurately describes the geometry of magnetic surfaces. We choose two different angular variables, a poloidal-like one (θ) and a toroidal-like one (ζ), together with a variable (r) that labels magnetic surfaces. We use ψ to represent the toroidal magnetic flux enclosed by a magnetic surface over 2π. Therefore

$$2\pi\psi(r) = \int \mathbf{B} \cdot \mathrm{d}\mathbf{S}_\zeta, \tag{2.28}$$

where $\mathrm{d}\mathbf{S}_\zeta$ is the area element perpendicular to surfaces of constant ζ. The poloidal flux χ enclosed by a magnetic surface is given by

$$2\pi\chi(r) = \int \mathbf{B} \cdot \mathrm{d}\mathbf{S}_\theta, \tag{2.29}$$

where $\mathrm{d}\mathbf{S}_\theta$ is the area element perpendicular to surfaces of constant θ.

The introduction of toroidal and poloidal magnetic fluxes allows for the mathematical description of the rotational transform, ι, a quantity already mentioned in section 1.2. It is defined as

$$\iota = \frac{\mathrm{d}\chi(r)}{\mathrm{d}\psi(r)}. \tag{2.30}$$

This formal definition clarifies the interpretation previously given in section 1.2, where ι was explained as the number of poloidal turns a magnetic field line makes in a toroidal turn.

With the previous considerations, we can now introduce spatial coordinates $\{r, \alpha, \zeta\}$ that properly describe the flux tube geometry, where $r \in [0, a]$ is the radial coordinate, $\alpha \in [0, 2\pi)$ is an angular coordinate labelling field lines on each magnetic surface and $\zeta \in [\zeta_{\min}, \zeta_{\max}]$ is used as a coordinate along field lines. Here, a is the stellarator minor radius[4] and the value $r = a$ corresponds to the *last closed flux surface*. Specifically, we choose

$$r = a\sqrt{\frac{\psi}{\psi_a}}, \tag{2.31}$$

where $\psi_a = \psi(a)$ is the value of the toroidal magnetic flux at the last closed flux surface. As for α we take

$$\alpha = \theta - \iota\zeta, \tag{2.32}$$

known as Clebsch angle, where we have particularized θ and ζ to be, respectively, toroidal and poloidal angles such that the magnetic field lines are straight on them.

The coordinates $\{r, \alpha, \zeta\}$ allow to express the magnetic field $\mathbf{B}$ as

$$\mathbf{B} = \frac{\mathrm{d}\psi}{\mathrm{d}r}\nabla r \times \nabla\alpha. \tag{2.33}$$

In figure 2.2 (left) we show poloidal contours of different flux surfaces for the standard configuration of W7-X, together with the radial coordinate r. Additionally, figure 2.2 (right) presents a sketch of a flux tube surrounding a magnetic field line that crosses one of the contours depicted in figure 2.2 (left), along with the coordinates $\{\alpha, \zeta\}$. These magnetic surfaces and poloidal contours are obtained using the ideal MHD equilibrium code `VMEC` [31], which computes the equilibrium configurations of plasmas in three-dimensional devices by solving the three-dimensional MHD equilibrium equations.

[4]Given the volume of the last closed flux surface, V_a, the minor radius can be defined as $a = \sqrt{V_a/2\pi^2 R_0}$, where $2\pi R_0$ is the length of the magnetic axis and R_0 is called the stellarator major radius.

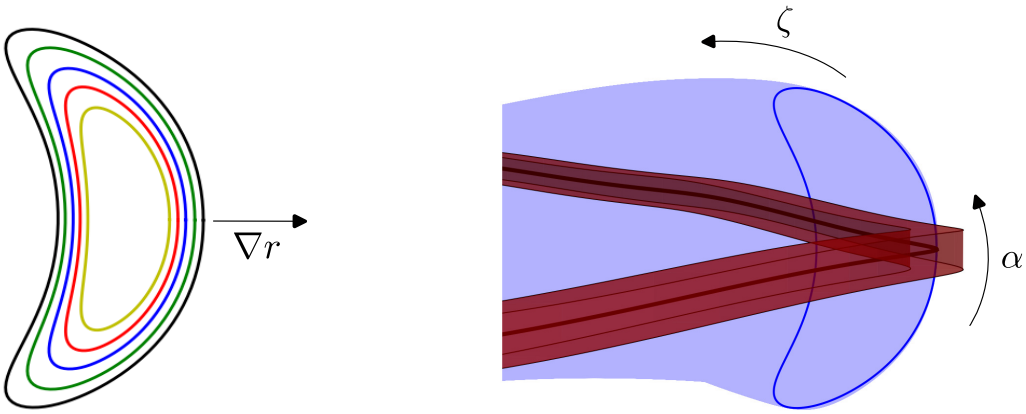

Figure 2.2: Left: poloidal cross sections of different magnetic surfaces corresponding to the standard configuration of W7-X. They are labeled by r/a=0.5 (yellow), r/a=0.6 (red), r/a=0.7 (blue), r/a=0.8 (green), and r/a=0.9 (black). The radial coordinate r is depicted. Right: sketch of a flux tube surrounding a magnetic field line, represented as a thick black line, that lies on the flux surface $r/a = 0.7$. The coordinates $\{\alpha, \zeta\}$ are also illustrated.

We use flux coordinates to express the gyrokinetic Vlasov (2.24) and quasi-neutrality (2.27) equations in the flux tube geometry. We begin by Fourier expanding the unknowns g_s^{tb} and φ^{tb} in the fast variations, see (2.22) and (2.23), perpendicular to the magnetic field:

$$\begin{aligned} g_s^{tb}\left(r,\alpha,\zeta,v_\parallel,\mu,t\right) &= \sum_{k_r,k_\alpha} \hat{g}^{tb}_{k_r k_\alpha,s}\left(r,\alpha,\zeta,v_\parallel,\mu,t\right)\exp(\mathrm{i}k_r r + \mathrm{i}k_\alpha \alpha), \\ \varphi^{tb}\left(r,\alpha,\zeta,t\right) &= \sum_{k_r,k_\alpha} \hat{\varphi}^{tb}_{k_r k_\alpha}\left(r,\alpha,\zeta,t\right)\exp(\mathrm{i}k_r r + \mathrm{i}k_\alpha \alpha), \end{aligned} \tag{2.34}$$

where k_r and k_α are wavenumbers such that the wavevector perpendicular to $\mathbf{B}$, $\mathbf{k}_\perp$, can be expressed as

$$\mathbf{k}_\perp = k_r \nabla r + k_\alpha \nabla \alpha. \tag{2.35}$$

We assume the Fourier coefficients vary slowly, accurate to

$$\begin{aligned}
&\frac{\partial \hat{g}^{tb}_{k_r k_\alpha,s}}{\partial r} \sim O\left(L^{-1}\hat{g}^{tb}_{k_r k_\alpha,s}\right), \qquad \frac{\partial \hat{g}^{tb}_{k_r k_\alpha,s}}{\partial \alpha} \sim O\left(\hat{g}^{tb}_{k_r k_\alpha,s}\right), \qquad \frac{\partial \hat{g}^{tb}_{k_r k_\alpha,s}}{\partial \zeta} \sim O\left(\hat{g}^{tb}_{k_r k_\alpha,s}\right), \\
&\frac{\partial \hat{\varphi}^{tb}_{k_r k_\alpha}}{\partial r} \sim O\left(L^{-1}\hat{\varphi}^{tb}_{k_r k_\alpha}\right), \qquad \frac{\partial \hat{\varphi}^{tb}_{k_r k_\alpha}}{\partial \alpha} \sim O\left(\hat{\varphi}^{tb}_{k_r k_\alpha}\right), \qquad \frac{\partial \hat{\varphi}^{tb}_{k_r k_\alpha}}{\partial \zeta} \sim O\left(\hat{\varphi}^{tb}_{k_r k_\alpha}\right),
\end{aligned} \tag{2.36}$$

whereas the wavenumbers k_r and k_α are assumed to be of the order

$$k_r \sim o\left(\rho_{*s}^{-1}L^{-1}\right), \qquad\qquad k_\alpha \sim o\left(\rho_{*s}^{-1}\right). \tag{2.37}$$

Hence, in the expansion $\rho_{*s} \ll 1$ the spatial derivatives of g^{tb}_s and φ^{tb} read

$$\begin{aligned}
\frac{\partial g^{tb}_s}{\partial r} &\simeq \sum_{k_r,k_\alpha} \mathrm{i}k_r \hat{g}^{tb}_{k_r k_\alpha,s} \exp(\mathrm{i}k_r r + \mathrm{i}k_\alpha \alpha), \\
\frac{\partial g^{tb}_s}{\partial \alpha} &\simeq \sum_{k_r,k_\alpha} \mathrm{i}k_\alpha \hat{g}^{tb}_{k_r k_\alpha,s} \exp(\mathrm{i}k_r r + \mathrm{i}k_\alpha \alpha), \\
\frac{\partial g^{tb}_s}{\partial \zeta} &\simeq \sum_{k_r,k_\alpha} \frac{\partial \hat{g}^{tb}_{k_r k_\alpha,s}}{\partial \zeta} \exp(\mathrm{i}k_r r + \mathrm{i}k_\alpha \alpha), \\
\frac{\partial \varphi^{tb}}{\partial r} &\simeq \sum_{k_r,k_\alpha} \mathrm{i}k_r \hat{\varphi}^{tb}_{k_r k_\alpha} \exp(\mathrm{i}k_r r + \mathrm{i}k_\alpha \alpha), \\
\frac{\partial \varphi^{tb}}{\partial \alpha} &\simeq \sum_{k_r,k_\alpha} \mathrm{i}k_\alpha \hat{\varphi}^{tb}_{k_r k_\alpha} \exp(\mathrm{i}k_r r + \mathrm{i}k_\alpha \alpha), \\
\frac{\partial \varphi^{tb}}{\partial \zeta} &\simeq \sum_{k_r,k_\alpha} \frac{\partial \hat{\varphi}^{tb}_{k_r k_\alpha}}{\partial \zeta} \exp(\mathrm{i}k_r r + \mathrm{i}k_\alpha \alpha).
\end{aligned} \tag{2.38}$$

In order to formulate the flux tube version of equations (2.24) and (2.27) we need to express $\langle \phi^{tb}_s \rangle_\gamma(\mathbf{X})$ as a function of the coefficients $\hat{\varphi}^{tb}_{k_r k_\alpha}(\mathbf{X})$. Therefore, we Taylor expand

ϕ_s^{tb} in the vicinity of $\mathbf{X}$,

$$\begin{aligned}
\langle\phi_s^{tb}\rangle_\gamma(\mathbf{X}) &= \left\langle \sum_{k_r,k_\alpha} \hat{\varphi}^{tb}_{k_r k_\alpha}(\mathbf{X}+\boldsymbol{\rho}_s)\exp[\mathrm{i}k_r r(\mathbf{X}+\boldsymbol{\rho}_s)+\mathrm{i}k_\alpha\alpha(\mathbf{X}+\boldsymbol{\rho}_s)]\right\rangle_\gamma \\
&= \Bigg\langle \sum_{k_r,k_\alpha} \left(\hat{\varphi}^{tb}_{k_r k_\alpha}(\mathbf{X}) + \boldsymbol{\rho}_s\cdot\nabla\hat{\varphi}^{tb}_{k_r k_\alpha}(\mathbf{X})+\cdots\right) \\
&\quad \exp\{\mathrm{i}k_r\left[r(\mathbf{X})+\boldsymbol{\rho}_s\cdot\nabla r(\mathbf{X})+\cdots\right]+\mathrm{i}k_\alpha\left[\alpha(\mathbf{X})+\boldsymbol{\rho}_s\cdot\nabla\alpha(\mathbf{X})+\cdots\right]\}\Bigg\rangle_\gamma \\
&= \left\langle \sum_{k_r,k_\alpha} \hat{\varphi}^{tb}_{k_r k_\alpha}(\mathbf{X})\exp[\mathrm{i}\left(k_r r+k_\alpha\alpha\right)]\exp[\mathrm{i}\boldsymbol{\rho}_s\cdot(k_r\nabla r+k_\alpha\nabla\alpha)]+\cdots\right\rangle_\gamma \\
&= \sum_{k_r,k_\alpha} \hat{\varphi}^{tb}_{k_r k_\alpha}\exp[\mathrm{i}\left(k_r r+k_\alpha\alpha\right)]\frac{1}{2\pi}\int_0^{2\pi}\exp(\mathrm{i}\boldsymbol{\rho}_s\cdot\mathbf{k}_\perp)\mathrm{d}\gamma+\cdots \\
&\simeq \sum_{k_r,k_\alpha} \hat{\varphi}^{tb}_{k_r k_\alpha}\exp[\mathrm{i}\left(k_r r+k_\alpha\alpha\right)]J_0\left(k_\perp v_\perp/\Omega_s\right), \qquad (2.39)
\end{aligned}$$

where

$$J_0(k_\perp v_\perp/\Omega_s)=\frac{1}{2\pi}\int_0^{2\pi}\exp\left(\mathrm{i}\frac{k_\perp v_\perp}{\Omega_s}\sin\gamma\right)\mathrm{d}\gamma \qquad (2.40)$$

is the zeroth order Bessel function of the first kind with $k_\perp=|\mathbf{k}_\perp|$ and $(\cdots)$ refers to higher-order terms in the expansion. As usual, if not stated otherwise, every quantity is evaluated at $\mathbf{X}$.

With these considerations, expression (2.24) simplifies to the collisionless and electrostatic gyrokinetic equation in a flux tube for the modes $\hat{g}^{tb}_{k_r k_\alpha,s}$ and $\hat{\varphi}^{tb}_{k_r k_\alpha}$, which reads

$$\begin{aligned}
&\frac{\partial\hat{g}^{tb}_{k_r k_\alpha,s}}{\partial t}+\left(\hat{\mathbf{b}}\cdot\nabla\zeta\right)\left(\frac{q_s}{T_s}v_\parallel\frac{\partial\left[\hat{\varphi}^{tb}_{k_r k_\alpha}J_0(k_\perp v_{\perp,s}/\Omega_s)\right]}{\partial\zeta}F_{Ms}+v_\parallel\frac{\partial\hat{g}^{tb}_{k_r k_\alpha,s}}{\partial\zeta}-\frac{\mu}{m_s}\frac{\partial B}{\partial\zeta}\frac{\partial\hat{g}^{tb}_{k_r k_\alpha,s}}{\partial v_\parallel}\right) \\
&-\frac{\mathrm{i}k_\alpha}{\mathrm{d}\psi/\mathrm{d}r}\left[\frac{\mathrm{d}\ln n_s}{\mathrm{d}r}+\frac{\mathrm{d}\ln T_s}{\mathrm{d}r}\left(\frac{m_s(v_\parallel^2/2+\mu B/m_s)}{T_s}-\frac{3}{2}\right)\right]\hat{\varphi}^{tb}_{k_r k_\alpha}J_0(k_\perp v_\perp/\Omega_s)F_{Ms} \\
&+\mathrm{i}\mathbf{v}_{Ms}\cdot\mathbf{k}_\perp\left(\hat{g}^{tb}_{k_r k_\alpha,s}+\frac{q_s}{T_s}\hat{\varphi}^{tb}_{k_r k_\alpha}J_0(k_\perp v_\perp/\Omega_s)F_{Ms}\right)-\mathcal{N}_{k_r k_\alpha,s}=0, \qquad (2.41)
\end{aligned}$$

with

$$\mathcal{N}_{k_r k_\alpha,s}=\sum_{\substack{k_{r1},k_{r2}\\ k_{\alpha1},k_{\alpha2}}}\frac{1}{B}\left[(\mathbf{k}_{\perp1}\times\mathbf{k}_{\perp2})\cdot\hat{\mathbf{b}}\right]\hat{g}^{tb}_{k_{r2}k_{\alpha2},s}\hat{\varphi}^{tb}_{k_{r1}k_{\alpha1}}J_0(k_{\perp1}v_\perp/\Omega_s) \qquad (2.42)$$

the nonlinear term, where $\mathbf{k}_{\perp1}=k_{r1}\nabla r+k_{\alpha1}\nabla\alpha$ and $\mathbf{k}_{\perp2}=k_{r2}\nabla r+k_{\alpha2}\nabla\alpha$ are such that $\mathbf{k}_{\perp1}+\mathbf{k}_{\perp2}=\mathbf{k}_\perp$. In order to obtain expression (2.41), we have assumed T_s and n_s to be flux functions, i.e., $T_s(r)$ and $n_s(r)$.

Similarly, we can express the quasi-neutrality equation (2.27) in the flux tube geometry for the modes $\hat{g}^{tb}_{k_r k_\alpha,s}$ and $\hat{\varphi}^{tb}_{k_r k_\alpha}$ as

$$\sum_s \frac{q_s B}{m_s} \int_{-\infty}^{\infty} \mathrm{d}v_\parallel \int_0^{\infty} \mathrm{d}\mu \hat{g}^{tb}_{k_r k_\alpha,s} J_0(k_\perp v_\perp/\Omega_s) \\ - \sum_s \frac{q_s^2 n_s}{2\pi T_s} \hat{\varphi}^{tb}_{k_r k_\alpha} \left(1 - \Gamma_0\left(\frac{k_\perp^2 v_{th,s}^2}{2\Omega_s^2}\right)\right) = 0, \tag{2.43}$$

where

$$\Gamma_0\left(\frac{k_\perp^2 v_{th,s}^2}{2\Omega_s^2}\right) = \exp\left(-\frac{k_\perp^2 v_{th,s}^2}{2\Omega_s^2}\right) I_0\left(\frac{k_\perp^2 v_{th,s}^2}{2\Omega_s^2}\right) \tag{2.44}$$

with I_0 the zeroth order modified Bessel function.

Therefore, the electrostatic and collisionless gyrokinetic system of equations in a flux tube consists of the gyrokinetic equation (2.41) and the quasi-neutrality equation (2.43). In this thesis we will use the code `stella` [24] to solve them.

2.4. The gyrokinetic code `stella`: coordinates and simulation settings

At the time of writing this thesis, `stella` [24], in its flux tube version, is a gyrokinetic code capable of solving the electromagnetic gyrokinetic system of equations for an arbitrary number of species and including the presence of collisions. In this work, we use the electrostatic and collisionless version of the code, which solves the gyrokinetic system of equations given by (2.41) and (2.43) for an arbitrary number of species.

The perpendicular spatial coordinates used by `stella` and employed throughout this thesis are $\{x, y\}$ defined as

$$x = r - r_0, \\ y = r_0(\alpha - \alpha_0), \tag{2.45}$$

where r and α are defined, respectively, by expressions (2.31) and (2.32), being r_0 and α_0 the values of r and α that select each simulated flux tube (and the centre of the simulation domain). In this way, both x and y have units of length. In particular, x measures the distance from the center of our domain in the radial coordinate (r) while y represents the arc length that subtends the angle α. Therefore, throughout this thesis, the direction of x will be referred to as *radial direction* and the direction of y as *binormal direction*. Analogously, `stella` takes ζ as the spatial coordinate parallel to the magnetic field.[5]

[5] With α selected, either ζ or θ can be chosen as parallel spatial coordinate, as shown in expression (2.32). In the study of tokamaks, θ is commonly used, whereas in stellarators, ζ is typically preferred.

Thus, `stella` solves the system of equations composed by (2.41) and (2.43) considering the coordinate system conformed by $\{x, y, \zeta\}$. Within this context, the flux tube version of the collisionless and electrostatic gyrokinetic Vlasov equation (2.41) implemented in the code can be expressed as

$$\frac{\partial \hat{g}^{tb}_{k_x k_y,s}}{\partial t} + \left(\hat{\mathbf{b}} \cdot \nabla\zeta\right)\left(\frac{q_s}{T_s} v_\parallel \frac{\partial\left[\hat{\varphi}^{tb}_{k_x k_y} J_0(k_\perp v_{\perp,s}/\Omega_s)\right]}{\partial\zeta} F_{Ms} + v_\parallel \frac{\partial \hat{g}^{tb}_{k_x k_y,s}}{\partial\zeta} - \frac{\mu}{m_s}\frac{\partial B}{\partial\zeta}\frac{\partial \hat{g}^{tb}_{k_x k_y,s}}{\partial v_\parallel}\right)$$
$$- \mathrm{i}k_y \frac{\mathrm{sgn}(\psi_a)}{B_a}\left[\frac{\mathrm{d}\ln n_s}{\mathrm{d}x} + \frac{\mathrm{d}\ln T_s}{\mathrm{d}x}\left(\frac{m_s(v_\parallel^2/2 + \mu B/m_s)}{T_s} - \frac{3}{2}\right)\right]\hat{\varphi}^{tb}_{k_x k_y} J_0(k_\perp v_\perp/\Omega_s) F_{Ms}$$
$$+ \mathrm{i}\mathbf{v}_{Ms}\cdot\mathbf{k}_\perp\left(\hat{g}^{tb}_{k_x k_y,s} + \frac{q_s}{T_s}\hat{\varphi}^{tb}_{k_x k_y} J_0(k_\perp v_\perp/\Omega_s) F_{Ms}\right) - \mathcal{N}_{k_x k_y,s} = 0, \tag{2.46}$$

where

$$B_a = \frac{2\psi_a}{a^2}\mathrm{sgn}(\psi_a) \tag{2.47}$$

denotes a normalizing magnetic field, such that the magnetic field (2.33) can be expressed as

$$\mathbf{B} = B_a \nabla x \times \nabla y. \tag{2.48}$$

As usual, in equation (2.46) $\mathcal{N}_{k_x k_y,s}$ represents the nonlinear term, which can be written in the coordinates (2.45) as

$$\mathcal{N}_{k_x k_y,s} = \frac{\mathrm{sgn}(\psi_a)}{B_a}\sum_{\substack{k_{x1},k_{y1}\\ k_{x2},k_{y2}}}\left(k_{x1}k_{y2} - k_{x2}k_{y1}\right)\hat{g}^{tb}_{k_{x2}k_{y2},s}\hat{\varphi}^{tb}_{k_{x1}k_{y1}} J_0(k_{\perp 1} v_\perp/\Omega_s). \tag{2.49}$$

Analogously, we can express the flux tube version of the quasineutrality equation (2.43) implemented in `stella` by using perpendicular coordinates $\{x, y\}$ as

$$\sum_s \frac{q_s B}{m_s}\int_{-\infty}^{\infty}\mathrm{d}v_\parallel \int_0^\infty \mathrm{d}\mu \hat{g}^{tb}_{k_x k_y,s} J_0(k_\perp v_\perp/\Omega_s)$$
$$- \sum_s \frac{q_s^2 n_s}{2\pi T_s}\hat{\varphi}^{tb}_{k_x k_y}\left(1 - \Gamma_0\left(\frac{k_\perp^2 v_{th,s}^2}{2\Omega_s^2}\right)\right) = 0. \tag{2.50}$$

The code `stella` employs a mixed implicit-explicit scheme for solving the system of equations conformed by (2.46) and (2.50). Specifically, the parallel streaming and acceleration terms appearing in the flux tube version of the gyrokinetic Vlasov equation (2.46) —the third and fourth terms in the equation, respectively— are solved implicitly, while the remaining terms are solved using an explicit time advance algorithm[6] (for

[6]For the explicit time advance algorithm, the user can choose between a standard fourth order Runge-Kutta and second or third order strong stability preserving Runge-Kutta schemes [32].

a more detailed explanation of how the code treats each term of equations (2.46) and (2.50) we refer the reader to [24]). This mixed implicit-explicit method offers a significant advantage over fully explicit schemes when accounting for the electron dynamics. This is because, when kinetic electrons are taken into account, the parallel streaming and acceleration terms of (2.46) scale up to a factor of $\sqrt{m_i/m_e} \approx 40$ (assuming H^+ as main ion species) compared to the other terms in the equation. This imposes a severe constraint on the integration time step size that is alleviated by implicit time advance schemes. This advantage in the performance of the code will be further discussed in section 4.2.

For the analysis of the results presented in chapters 4 and 5, it is essential to define the real frequency and growth rate of plasma instabilities. Given the coefficient of a mode of the electrostatic potential, characterized by its wavenumbers k_x and k_y, $\hat{\varphi}^{tb}_{k_x k_y}$, its temporal evolution can be Fourier-transformed as

$$\hat{\varphi}^{tb}_{k_x k_y}(\zeta, t) = \sum_{\omega} \check{\varphi}^{tb}_{k_x k_y, \omega}(\zeta) e^{-\mathrm{i}\omega t}, \tag{2.51}$$

where the frequency ω is a complex number defined as

$$\omega = \omega_r + \mathrm{i}\gamma. \tag{2.52}$$

Its real component, ω_r (usually referred to as *real frequency*), indicates the frequency of oscillation and its imaginary part, γ (usually referred to as *growth rate*), represents the growth or damping of the amplitude of $\hat{\varphi}_{k_x k_y}$. Values $\gamma \leq 0$ imply that the mode is stable while values $\gamma > 0$ correspond to those responsible for the instability growth. In the case of ignoring nonlinear effects, i.e. neglecting the nonlinear term $N_{k_x k_y, s}$, instabilities lead to the exponential increase of the electrostatic potential amplitude over time. In such linear simulations, the value of the complex frequency is adjusted for each mode at each time step by comparing the squared electrostatic potential between consecutive time steps. On the other hand, in nonlinear simulations where the exponential growth phase is followed by a saturation phase, the evolution of the potential in this saturated phase gives rise to frequency spectra, as presented in chapter 5.

The input parameters required by the code to perform a simulation, regardless of whether it is linear or nonlinear, include the magnetic configuration to be studied, the definition of the flux tube position in space, the phase-space grid, physical parameters of every species present in the plasma and the specification of the analysed wavenumbers (k_x, k_y). Regarding the magnetic configuration, it is obtained with the ideal MHD code `VMEC` [31]. The description of the flux tube of interest for the simulation requires the

specification of r_0 and α_0, along with the length of the flux tube in the direction parallel to the magnetic field. This is determined by the number of turns the flux tube makes expressed in machine field periods (e.g. in W7-X, which has 5 field periods, i.e. $N_{fp} = 5$, each field period covers an angle $2\pi/5$ in ζ) and the number of divisions along ζ, N_ζ. With respect to the physical parameters of each species, they include the temperature and density ratios of the main ions and electrons in the plasma, along with other species-specific characteristics such as their charge, mass, temperature, density, and normalized temperature and density gradients, given by

$$a/L_{T_s} = -a\left(\frac{\mathrm{d}\ln T_s}{\mathrm{d}x}\right), \qquad a/L_{n_s} = -a\left(\frac{\mathrm{d}\ln n_s}{\mathrm{d}x}\right). \tag{2.53}$$

In addition, the number of divisions in $v_\parallel$ ($N_{v_\parallel}$) and μ (N_μ) must be provided, together with the time step, Δt, considered for the simulation. As previously indicated, for linear simulations, each mode $\hat{\varphi}^{tb}_{k_x k_y}$ is analysed independently, requiring just the specific value of the wavenumber (k_x, k_y) as input parameter. However, when a nonlinear simulation is addressed, the Fourier components of the fluctuation are coupled. In fact, the selection of k_x and k_y values considered in a nonlinear simulation is, in general, not free since, given a minimum value of k_y ($k_y^{\min}$), the boundary conditions in the parallel direction of the flux tube restrict the allowed values of k_x. This restriction depends on certain quantities of the magnetic configuration considered, as it will be discussed in chapter 3. Therefore, in a nonlinear simulation, the domain in k_x and k_y is completely defined by specifying $k_y^{\min}$ and the total number of radial and binormal wavenumbers (N_{k_x} and N_{k_y}, respectively) included in them. It is important to note that the ion thermal Larmor radius

$$\rho_i = \frac{v_{th,i} m_i}{q_i B_a}, \tag{2.54}$$

will be used to normalize the wavector components throughout this thesis.

Among the input parameters available in `stella`, those most relevant to the simulations performed in this work are listed in table 2.1. This table also includes each parameter's name as it appears in the `stella` input file, along with its physical interpretation.

Input name	Quantity	Description
`vmec_filename`	Magnetic geometry	`VMEC` output file. Among other quantities, it gives the Fourier representation of the magnetic field, $\mathbf{B}$, the stellarator minor radius, a, the profile of ι, the plasma geometry and other geometric information.
`torflux`	$(r_0/a)^2$	Normalized value of r_0^2 that selects the center of the flux tube in the radial coordinate. For instance, `torflux`=0.36 indicates that the flux tube is centered with respect to $r_0/a = 0.6$
`alpha0`	α_0	Value of α_0 that selects the center of the flux tube in the coordinate α. For instance, `alpha0`=0 indicates that the flux tube is centered at $(\theta = 0, \zeta = 0)$, see expression (2.32)
`nzed`	N_ζ	Number of divisions in ζ
`nfield_periods`		Number of turns the flux tube makes in the toroidal direction in units of machine field periods. It relates with the number of poloidal turns through ι as $N_\theta = \iota \frac{\texttt{nfield\_periods}}{N_{fp}}$
`nmu`	N_μ	Number of divisions in μ
`nvgrid`	$N_{v_\parallel}$	Number of divisions in $v_\parallel$
`nine`	n_i/n_e	Ratio between ion and electron densities
`tite`	T_i/T_e	Ratio between ion and electron temperatures
`z`	q_s/q_i	Normalized charge of species s
`mass`	m_s/m_i	Normalized mass of species s
`temp`	T_s/T_i	Normalized temperature of species s
`dens`	n_s/n_i	Normalized density of species s
`tprim`	a/L_{T_s}	Normalized temperature gradient of species s
`nprim`	a/L_{n_s}	Normalized density gradient of species s
`delt`	$v_{th,i}\Delta t/a$	Normalized time step
`nakx, naky`	N_{kx}, N_{ky}	Number of radial and binormal wavenumbers in the ranges $[k_x^{\min}, k_x^{\max}]$ and $[k_y^{\min}, k_y^{\max}]$, respectively. Only for linear simulations
`nakx_min, naky_min`	$k_x^{\min}, k_y^{\min}$	Minimum value of normalized radial and binormal wavenumbers. Only for linear simulations

This table continues in the next page

Input name	**Quantity**	**Description**
`nakx_max`, `naky_max`	$k_x^{\max}, k_y^{\max}$	Maximum value of normalized radial and binormal wavenumbers. Only for linear simulations
`nx`	N_x	In nonlinear simulations, number of divisions of the flux tube along its radial extend. To prevent aliasing, it relates to the number of radial wavenumbers, N_{kx}, as $N_{k_x} = \frac{2(N_x-1)}{3} + 1$
`ny`	N_y	In nonlinear simulations, number of divisions of the flux tube along its binormal extend. To prevent aliasing, it relates to the number of binormal wavenumbers, N_{ky}, as $N_{k_y} = \frac{(N_y-1)}{3} + 1$
`y0`	L_y	In nonliner simulations, extension of the flux tube in the binormal direction in units of $2\pi\rho_i$. It relates with the minimum k_y value as $k_y^{\min}\rho_i = \texttt{y0}^{-1}$

Table 2.1: List of input parameters required for a standard simulation performed with `stella`. The first column lists the variable names as used in the `stella` input file; the second column corresponds to the associated physical quantities and the third column provides a brief description of the relationship between each physical quantity and its respective input parameter.

CHAPTER 3

Parallel boundary conditions in the code `stella`

The results presented in this chapter are original from this thesis work.

In this chapter, we will describe the different boundary conditions in the parallel direction employed by the code `stella`. As outlined in the description of the flux tube in section 2.3, this geometry extends over a finite length along the coordinate that measures distance along the magnetic field line. Equations (2.41) and (2.43) are then solved imposing boundary conditions in this direction. Specifically, in nonlinear simulations, the formulation of these boundary conditions relies on the assumption that turbulence is statistically periodic at geometrically identical points over the magnetic surface. As it will be shown below, this condition determines the maximum wavelengths allowed in the perpendicular directions in nonlinear simulations, or, equivalently, the size of our domain in k_x and k_y. In this context, we will present the commonly used *standard* twist-and-shift boundary conditions [33], which were already implemented in `stella` before the realization of this thesis, and the so-called *stellarator-symmetric* twist-and-shift boundary conditions [34], whose implementation is a significant contribution of the work developed for the present thesis. This implementation has been crucial because, as will be shown in this chapter, the constraints imposed by the standard twist-and-shift boundary conditions on the smallest k_x allowed or, equivalently, on the size of the our spatial domain in the radial direction, are particularly restrictive in devices such as W7-X. In fact, before the implementation of the stellarator-symmetric twist-and-shift boundary conditions, studying certain surfaces of this device was extremely expensive with `stella`.

3.1. Twist-and-shift boundary conditions in flux tube codes

The standard parallel boundary conditions within a flux tube geometry impose that any

fluctuating quantity, A, must be equal at the flux tube endpoints $z_+ = (x_+, y_+, \zeta_+)$ and $z_- = (x_-, y_-, \zeta_-)$. In other words

$$[A]_{z_-} = [A]_{z_+}, \tag{3.1}$$

where $[A]_z$ means that the quantity A is evaluated at the position z. Underlying this hypothesis is the fact that, given two geometrically identical points on a flux surface that are sufficiently separated along the parallel coordinate, turbulence is statistically periodic. Concerning the first point, in the stellarator geometry, the geometric identity of the endpoints occurs only in field lines with stellarator symmetry [35], whereas, in a tokamak, it occurs between points separated by an integer number of poloidal turns.

If we denote the position of the magnetic field line by $\mathbf{r}_0(x_0, y_0, \zeta)$, any point in the flux tube can be labeled with coordinates $(x = x_0 + \Delta x,\, y = y_0 + \Delta y, \zeta)$, such that the position vector $\mathbf{r}$ can be written as

$$\mathbf{r}(x, y, \zeta) \approx \mathbf{r}_0(\zeta) + \mathbf{e}_x \Delta x + \mathbf{e}_y \Delta y, \tag{3.2}$$

where $\mathbf{e}_x = \frac{\partial \mathbf{r}}{\partial x}$ and $\mathbf{e}_y = \frac{\partial \mathbf{r}}{\partial y}$ denote a set of perpendicular basis vectors. Alternatively, we can also parametrize any fluctuating quantity A in coordinates (u, v), defining the orthonormal vectors perpendicular to $\mathbf{B}$

$$\mathbf{e}_u = \frac{\nabla x}{|\nabla x|}, \qquad\qquad \mathbf{e}_v = \frac{\hat{\mathbf{b}} \times \nabla x}{|\nabla x|}, \tag{3.3}$$

being it possible to relate the coordinates (u, v) with (x, y) as

$$u = (\mathbf{r} - \mathbf{r}_0) \cdot \mathbf{e}_u, \qquad\qquad v = (\mathbf{r} - \mathbf{r}_0) \cdot \mathbf{e}_v. \tag{3.4}$$

Therefore, by substituting (3.2) and (3.3) into (3.4) and using the expression (2.48) for the magnetic field, we can write explicitly (x, y) as a function of (u, v) as

$$x = u|\nabla x|, \qquad\qquad y = \frac{\nabla x \cdot \nabla y}{|\nabla x|} u + \frac{B}{B_a |\nabla x|} v. \tag{3.5}$$

As stated in section 2.3 (see expressions (2.34)), in the flux tube approach, fluctuating quantities can be expressed in Fourier series as

$$A(x, y, \zeta, t) = \sum_{k_x, k_y} \hat{A}_{k_x k_y}(\zeta, t) \exp\left(\mathrm{i} k_x x + \mathrm{i} k_y y\right). \tag{3.6}$$

Accordingly, they can be written in coordinates (u, v) as

$$A = \sum_{k_x, k_y} \hat{A}_{k_x k_y} \exp\left\{ \mathrm{i} \left[\left(|\nabla x| k_x + \frac{\nabla x \cdot \nabla y}{|\nabla x|} k_y \right) u + \left(\frac{B}{B_a |\nabla x|} k_y \right) v \right] \right\}. \tag{3.7}$$

Imposing the condition expressed in equation (3.1) yields the following constraints for the different factors present in the exponent of (3.7):

$$\begin{aligned}\left[\hat{A}_{k_x k_y}\right]_{z_+} &= \left[\hat{A}_{k_x k_y}\right]_{z_-}, \\ \left[\left(|\nabla x| k_x + \frac{\nabla x \cdot \nabla y}{|\nabla x|} k_y\right)\right]_{z_+} &= \left[\left(|\nabla x| k_x + \frac{\nabla x \cdot \nabla y}{|\nabla x|} k_y\right)\right]_{z_-}, \\ \left[\frac{B}{B_a |\nabla x|} k_y\right]_{z_+} &= \left[\frac{B}{B_a |\nabla x|} k_y\right]_{z_-},\end{aligned} \tag{3.8}$$

which are general expressions for twist-and-shift boundary conditions in a flux tube. It is typically assumed that, in addition,

$$[B]_{z_+} = [B]_{z_-}, \qquad [|\nabla x|]_{z_+} = [|\nabla x|]_{z_-}, \tag{3.9}$$

reducing expressions (3.8) to

$$[k_x]_{z_+} - [k_x]_{z_-} = \frac{k_y}{[|\nabla x|^2]_{z+}} \left([\nabla x \cdot \nabla y]_{z_-} - [\nabla x \cdot \nabla y]_{z_+}\right), \tag{3.10}$$

where $|\nabla x|$ can be evaluated at either z_+ or z_-, as we have considered $[\nabla x]_{z_-} = [\nabla x]_{z_+}$, and k_y is not explicitly evaluated at $z_\pm$ because it remains constant throughout the entire domain.

Expression (3.10) indicates that each k_y value connects different values of k_x. Therefore, the left hand side of this expression constraints the largest step size in k_x allowed in a simulation, that we will denote as

$$\Delta k_x = [k_x]_{z_+} - [k_x]_{z_-}. \tag{3.11}$$

In `stella` the grid in k_y is equi-spaced and the first computed value is always $k_y = 0$, therefore, the grid spacing in k_y is equivalent to $k_y^{\min}$. In the same way, the grid spacing in k_x is equivalent to $|k_x|^{\min}$.

3.1.1. Standard twist-and-shift boundary conditions

The so-called standard twist-and-shift boundary conditions [33], impose that the flux tube ends are separated an integer number of poloidal turns, which implies that[1]

$$z_- = (x, y(\theta, \zeta), \theta), \qquad z_+ = (x, y(\theta + 2\pi N, \zeta), \theta + 2\pi N), \tag{3.12}$$

[1] If ζ is used as parallel coordinate instead of θ, as it is the case in `stella`, expressions (3.12) would take the form $z_- = (x, y(\theta, \zeta), \zeta)$ and $z_+ = (x, y(\theta, \zeta + 2\pi N), \zeta + 2\pi N)$. This is the definition for standard twist-and-shift boundary conditions considered for the following derivations

where N is an integer.

Therefore, using the definitions of coordinates x and y, see expressions (2.45), we have

$$\begin{aligned}
\left[\nabla x\cdot\nabla y\right]_{z_-} &= r_0\left(\nabla x\cdot\nabla\theta-\iota\nabla x\cdot\nabla\zeta-\zeta\frac{\mathrm{d}\iota}{\mathrm{d}x}|\nabla x|^2\right),\\
\left[\nabla x\cdot\nabla y\right]_{z_+} &= r_0\left(\nabla x\cdot\nabla\theta-\iota\nabla x\cdot\nabla\zeta-\zeta\frac{\mathrm{d}\iota}{\mathrm{d}x}|\nabla x|^2-2\pi N\frac{\mathrm{d}\iota}{\mathrm{d}x}|\nabla x|^2\right),
\end{aligned}\tag{3.13}$$

so that the shift of radial wavenumbers, see expression (3.10), can be written as

$$\Delta k_x = 2\pi N\iota|\hat{s}|k_y,\tag{3.14}$$

where the global magnetic shear[2]

$$\hat{s}=-\frac{r_0\mathrm{d}\iota}{\iota\mathrm{d}x}\tag{3.15}$$

has been introduced.

Expression (3.14) makes evident the problematic application of these boundary conditions when studying low shear devices. Since the grid spacing in k_x, or equivalently, $|k_x|^{\min}$, is proportional to the global magnetic shear, a low value of $\hat{s}$ requires to simulate significantly more values of k_x than of k_y.

Figure 3.1 illustrates these restrictions. For instance, in figure 3.1 (left), we see that $|k_x|^{\min}\approx 0.1k_y^{\min}$ for the surface labeled by $r_0/a=0.35$ in the standard configuration of W7-X, which has low magnetic shear. The shape of the global magnetic shear for this configuration of W7-X can be found in figure 3.1 (right), where it is represented as a function of the radial direction.

3.1.2. Stellarator symmetric twist-and-shift boundary conditions

On the other hand, stellarator symmetric twist-and-shift boundary conditions, formulated in [34] as an alternative to the standard twist-and-shift boundary conditions discussed in section 3.1.1, impose the flux tube endpoints to be stellarator symmetric points [35], therefore

$$z_-=(x,y(-\theta,-\zeta),\zeta)\,,\qquad\qquad z_+=(x,y(\theta,\zeta),\zeta)\,.\tag{3.16}$$

[2]Note that in expression (3.15) r_0 is the center of the flux tube in the radial direction (see expression (2.45)) and should not be taken to be as the modulus of $\mathbf{r}_0$ in expression (3.2).

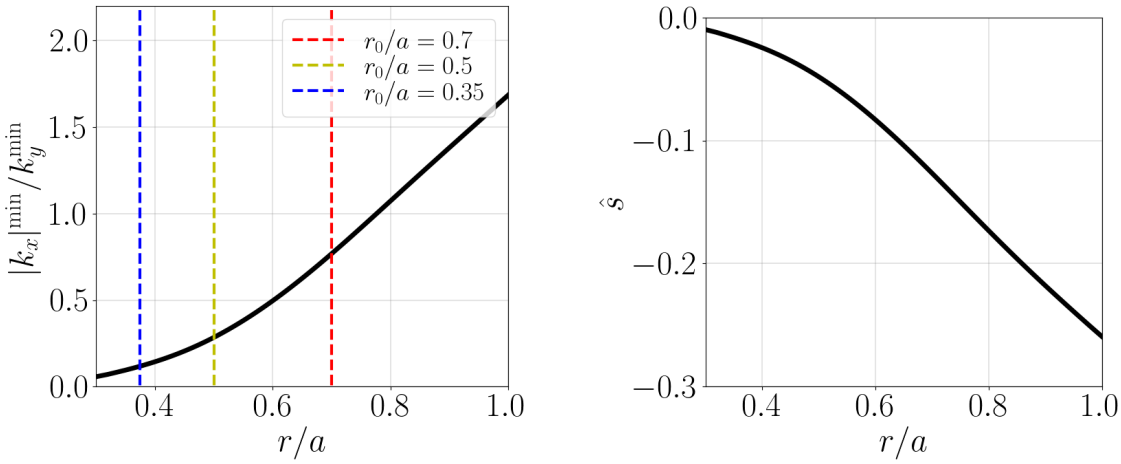

Figure 3.1: Left: ratio between $|k_x|^{\min}$ and $k_y^{\min}$, or equivalently, between the grid spacing in k_x and k_y for the standard configuration of W7-X as a function of the radial direction, computed using standard twist-and-shift boundary conditions. The vertical dashed lines indicate different radial positions, labeled by $r_0/a = 0.35$ in blue, $r_0/a = 0.5$ in yellow and $r_0/a = 0.7$ in red. Right: global magnetic shear (see expression (3.15)) as a function of the radial direction, computed for the W7-X configuration used for the calculations presented in the left figure.

Hence, by applying the definitions of perpendicular coordinates provided in equation (2.45), we obtain

$$\begin{aligned}
[\nabla x \cdot \nabla y]_{z_-} &= r_0 \left(-\nabla x \cdot \nabla \theta + \iota \nabla x \cdot \nabla \zeta + \zeta \frac{\mathrm{d}\iota}{\mathrm{d}x} |\nabla x|^2 \right), \\
[\nabla x \cdot \nabla y]_{z_+} &= r_0 \left(\nabla x \cdot \nabla \theta - \iota \nabla x \cdot \nabla \zeta - \zeta \frac{\mathrm{d}\iota}{\mathrm{d}x} |\nabla x|^2 \right)
\end{aligned} \tag{3.17}$$

and the following expression for the shift in the radial wavenumber

$$\Delta k_x = 2 \frac{[\nabla x \cdot \nabla y]_{z_+}}{[|\nabla x|^2]_{z+}} k_y = -2 \frac{[\nabla x \cdot \nabla y]_{z_-}}{[|\nabla x|^2]_{z-}} k_y. \tag{3.18}$$

Expression (3.18) reveals that, unlike standard twist-and-shift boundary conditions, Δk_x does not depend on $\hat{s}$ but on $[\nabla x \cdot \nabla y]_{z\pm}$ and on $|\nabla x|_{z\pm}$ when using the stellarator symmetric ones. This allows to adjust the flux tube length to set the grid spacing in k_x approximately equal to the grid spacing in k_y, or equivalently, to achieve $|k_x|^{\min} \approx k_y^{\min}$ as shown in figure 3.2. In fact, in this figure it can be observed, for three different radial locations, that within nearly one full toroidal turn of the flux tube, we can achieve $|k_x|^{\min}/k_y^{\min} \approx 1$ using these boundary conditions (the radial locations are the same as those depicted in figure 3.1 (left)). It is worth noting the result for the radial position

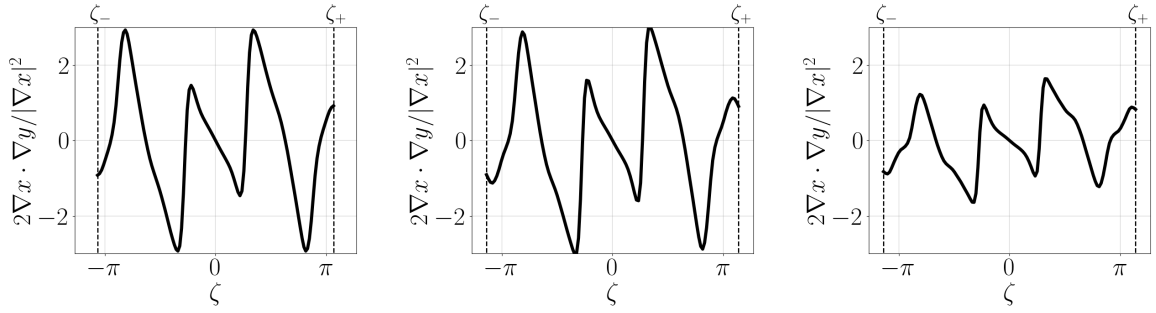

Figure 3.2: Factor that relates Δk_x and k_y when using stellarator symmetric twist-and-shift boundary conditions, see expression (3.18), represented as a function of the parallel coordinate, ζ, for the full flux tube length. Results computed for the standard configuration of W7-X in the radial positions labeled by $r_0/a = 0.35$ (left), $r_0/a = 0.5$ (center) and $r_0/a = 0.7$ (right).

$r_0/a = 0.35$, given that the standard twist-and-shift boundary conditions would impose $|k_x|^{\min}/k_y^{\min} \approx 0.1$. In summary, the choice of boundary conditions –stellarator symmetric versus standard twist-and-shift boundary conditions– at that particular position would result in a simulation requiring approximately 10 times fewer values of k_x to cover the same k_x range.

3.2. Stellarator symmetric twist-and-shift boundary conditions in `stella`

We perform a series of tests comparing the results obtained in similar simulations using standard and stellarator symmetric twist-and-shift boundary conditions considering different radii of the stellarator W7-X. With these simulations we want to probe not only the correct implementation[3] of stellarator symmetric twist-and-shift boundary

[3]In `stella`, the geometric quantities required to solve the gyrokinetic system of equations are obtained from a VMEC output through a dedicated geometry interface. These quantities are provided in the VMEC coordinate system and must be processed to obtain expression (3.18). Specifically, in these coordinates, expression (3.18) becomes

$$\Delta k_x = 2\frac{\psi(r_0)}{\psi_a}\frac{\left[\overline{\nabla\psi\cdot\nabla\alpha}\right]_{z+}}{\left[|\overline{\nabla\psi}|^2\right]_{z+}}k_y, \tag{3.19}$$

where the ends of the flux tube are those of the selected magnetic field line segment $z_+ = (r_0, \alpha_0, \zeta_+)$ and $\overline{A}$ denotes that the quantity A is normalized. In particular, the normalizations used are

$$\overline{\nabla\psi} = \frac{\nabla\psi}{aB_a}, \qquad\qquad \overline{\nabla\alpha} = a\nabla\alpha.$$

Expression (3.19) is the one we have coded for the implementation of the stellarator symmetric twist-and-shift boundary conditions in `stella`.

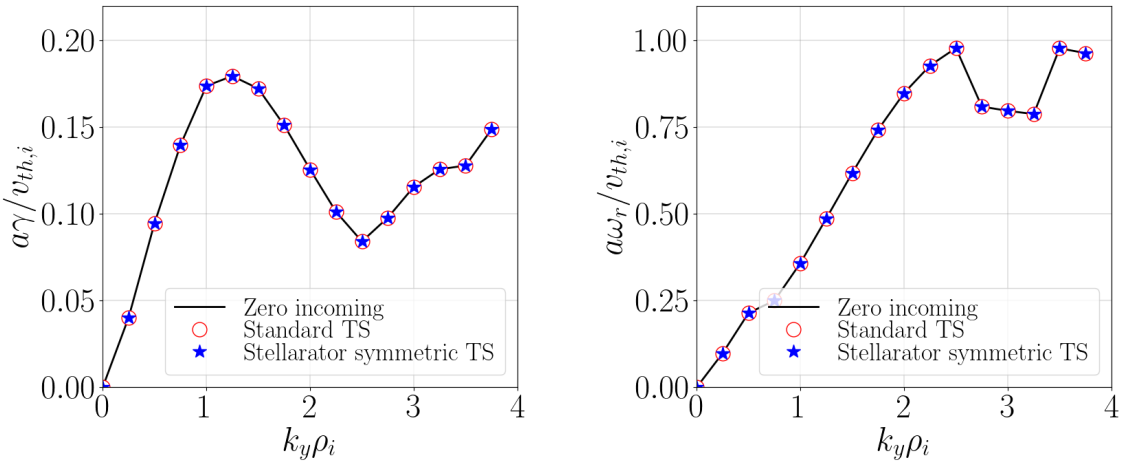

Figure 3.3: Normalized linear growth rates (left) and real frequencies (right) as a function of k_y for a fixed $k_x = 0$ for the surface labeled by $r_0/a = 0.7$ of the standard configuration of W7-X. Results obtained using zero incoming (solid black line), standard twist-and-shift (empty red circles) and stellarator symmetric twist-and-shift (blue stars) boundary conditions.

conditions, but also their advantages over the standard twist-and-shift ones and assess any differences in the results obtained with both choices. First, we start by comparing the results obtained in linear simulations performed with `stella` using zero incoming boundary conditions on the Fourier coefficients of the fluctuation distribution function $\left(\hat{g}^{tb}_{k_x k_y,s}(\zeta_-, v_\parallel > 0) = \hat{g}^{tb}_{k_x k_y,s}(\zeta_+, v_\parallel < 0) = 0)\right)$ and those obtained using standard and stellarator symmetric twist-and-shift boundary conditions. We would expect the results obtained when using these three boundary conditions to be identical since, as explained in section 2.4, in linear simulations the modes with different wavenumbers (k_x, k_y) are decoupled.

To explore this, we compute the linear spectra of the growth rate and the real frequency of an ion-temperatue-gradient (ITG) instability. For this, we have assumed hydrogen ions (H^+) as the main species, adiabatic electrons, normalized ion temperature gradient of $a/L_{T_i} = 4$ and a vanishing density gradient ($a/L_{n_i} = 0$) for the radial position $r_0/a = 0.7$ of the standard configuration of W7-X.

Figure 3.3 shows the results for the growth rate (left) and for the real frequency (right) as a function of k_y and for a fixed $k_x = 0$. It is important to remark that, when using both alternative choices of twist-and-shift boundary conditions, we have considered three values of the radial wavenumber to perform the connection between different values of k_x (see expression (3.10)), while only the central value, $k_x = 0$, is shown in the figure.

Additionally, for simulations with zero incoming boundary conditions, the amplitude of each Fourier coefficient must decay at the flux tube ends to ensure convergence. To achieve this, we have simulated nearby six full toroidal turns per flux tube. As expected, in this figure we find a perfect agreement between the calculations performed using the three different boundary conditions. Based on this initial verification, we can confidently conclude that the implementation of stellarator symmetric twist-and-shift boundary conditions is correct and has not introduce modifications where they are not expected.

We now turn our attention to the nonlinear simulations, where different boundary conditions can affect the computational demands of a simulation given that they determine the ratio $|k_x|^{\min}/k_y^{\min}$, as we have commented above.

As an initial nonlinear test, we simulate the same ITG case as in the linear check discussed above applying both standard and stellarator symmetric twist-and-shift boundary conditions. In addition, to ensure a fair comparison between the results obtained with both boundary conditions, we use identical grids of $\{126, 24, 12\}$ points in $\{\zeta, v_\parallel, \mu\}$. The radial position $r_0/a = 0.7$ is selected for this first nonlinear test given that, as shown in left figure 3.1 (red line), the ratio $|k_x|^{\min}/k_y^{\min} \approx 1$ imposed by standard twist-and-shift boundary conditions is comparable to that achieved with stellarator symmetric twist-and-shift boundary conditions in nearly one toroidal turn of the flux tube, as shown in figure 3.2 (right). These values are specified in table 3.1. Consequently, we do not anticipate significant differences neither in the performance nor in the simulations results when using the two different boundary conditions.

In figure 3.4 we show the time traces of the calculated ion heat fluxes, Q_i, which can be written as

$$Q_i = \frac{\pi \mathrm{sgn}(\psi_\mathrm{a})}{B_a} \left(\int_{\zeta_-}^{\zeta_+} \frac{\mathrm{d}\zeta}{(\mathbf{B}\cdot\nabla\zeta)} \right)^{-1} \int_{\zeta_-}^{\zeta_+} \mathrm{d}\zeta \int_{-\infty}^{\infty} \mathrm{d}v_\parallel \int_0^{\infty} \mathrm{d}\mu \left(v_\parallel^2 + \frac{2B\mu}{m_i} \right) \sum_{k_x,k_y} \mathrm{Im}\left(\hat{\varphi}^{tb}_{k_x k_y} \hat{g}^{tb}_{-k_x-k_y,i} \right) k_y J_0(k_\perp v_{\perp,i}/\Omega_i) \left(\hat{\mathbf{b}}\cdot\nabla\zeta \right)^{-1}, \tag{3.20}$$

and are represented normalized to the ion gyro-Bohm heat flux, $Q_{gB,i}$, defined as

$$Q_{gB,i} = n_i T_i v_{th,i} \left(\frac{\rho_i}{a} \right)^2. \tag{3.21}$$

In figure 3.4 it can be observed that the ion heat flux time traces obtained with each of the two boundary conditions choices are similar and the converged values, which are averaged over the grey shadowed region and collected in table 3.1, are comparable. The

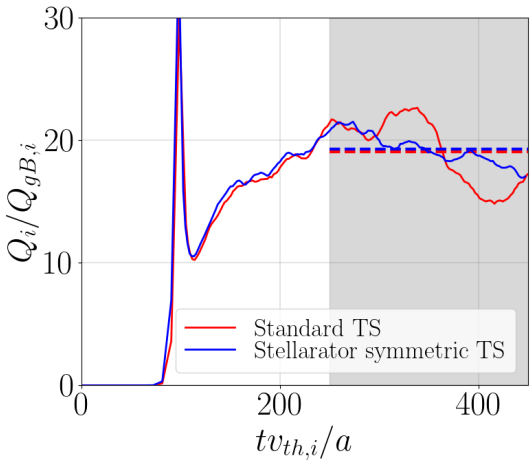

Figure 3.4: Time trace of the normalized ion heat flux computed using standard twist-and-shift boundary conditions (red) and stellarator symmetric twist-and-shift boundary conditions (blue) at the radial position $r_0/a = 0.7$ of the standard configuration of W7-X. The dashed lines show the time-averaged quantities over the shadowed time range.

Boundary condition	$(k_x^{\max}\rho_i, k_y^{\max}\rho_i)$	N_{k_x}	N_{k_y}	$\lvert k_x\rvert^{\min}/k_y^{\min}$	$Q_i/Q_{gB,i}$	t_{CPU} [h]
Standard	(1.0, 2.5)	53	51	0.81	19.1 ± 2.7	3456
Stell. symmetric	(1.0, 2.5)	47	51	0.89	19.3 ± 1.2	3325

Table 3.1: Parameters of the nonlinear simulations performed for the radial position $r_0/a = 0.7$ of the standard configuration of W7-X. From left to right: twist-and-shift boundary condition choice; maximum considered value of k_x and k_y; number of simulated values of k_x; number of simulated values of k_y; ratio between the grid spacing in k_x and k_y or, equivalently, between $\lvert k_x\rvert^{\min}$ and $k_y^{\min}$; value of the time-averaged ion heat flux and CPU time required to run the simulation.

values of CPU time required to complete each simulation are also indicated in this table. The minor discrepancies in the CPU hours are attributed to the fewer number of radial wavenumbers required to reach the same maximum k_x when using stellarator symmetric twist-and-shift boundary conditions, as shown in the same table 3.1.

As a second nonlinear test, we perform a similar comparison but for the radial position $r_0/a = 0.5$ of the standard configuration of W7-X. We have chosen this surface for the second test because, as shown in figure 3.1 (left) (see yellow line), the standard twist-and-shift boundary conditions limit the ratio $\lvert k_x\rvert^{\min}/k_y^{\min} \approx 0.3$. This constraint requires simulating approximately three times more values of k_x to cover the same range of radial wavenumbers as when using stellarator symmetric twist-and-shift boundary conditions,

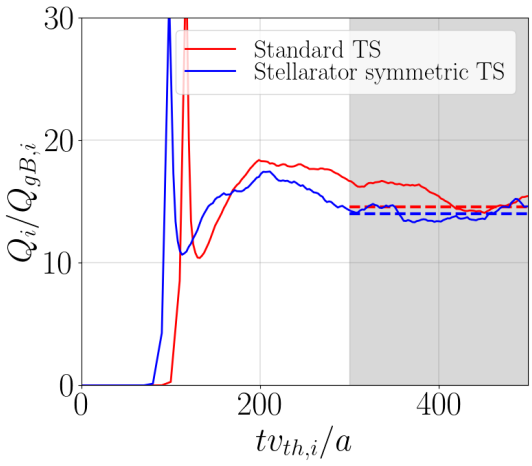

Figure 3.5: Time trace of the normalized ion heat flux computed using standard twist-and-shift boundary conditions (red) and stellarator symmetric twist-and-shift boundary conditions (blue) at the radial position $r_0/a = 0.5$ of the standard configuration of W7-X. The dashed lines show the time-averaged quantities over the shadowed time range.

Boundary condition	$(k_x^{\max}\rho_i, k_y^{\max}\rho_i)$	N_{k_x}	N_{k_y}	$\lvert k_x\rvert^{\min}/k_y^{\min}$	$Q_i/Q_{gB,i}$	t_{CPU} [h]
Standard	(1.0, 2.5)	135	51	0.30	14.6 ± 0.4	13248
Stell. symmetric	(1.0, 2.5)	47	51	0.89	15.0 ± 0.5	2880

Table 3.2: Parameters of the nonlinear simulations performed for the radial position $r_0/a = 0.5$ of the standard configuration of W7-X. From left to right: twist-and-shift boundary condition choice; maximum considered value of k_x and k_y; number of simulated values of k_x; number of simulated values of k_y; ratio between the grid spacing in k_x and k_y or, equivalently, between $\lvert k_x\rvert^{\min}$ and $k_y^{\min}$; value of the time-averaged ion heat flux and CPU time required to run the simulation.

with which the ratio $\lvert k_x\rvert^{\min}/k_y^{\min} \approx 1$ can be reached with roughly one toroidal turn of the flux tube (see figure 3.2 (center)). These specific values are listed in table 3.2. Additionally, simulating the large number of k_x values needed by the standard twist-and-shift boundary conditions has required to reduce the grid in ζ to keep computation times manageable. In particular, we have assumed grids of $\{96, 24, 12\}$ in $\{\zeta, v_\parallel, \mu\}$ for the simulations to perform this comparison.

The normalized ion heat flux time traces obtained from these simulations are represented in figure 3.5. This figure shows that, again, the converged results of ion heat flux computed with both twist-and-shift boundary conditions are similar. The heat flux values from this comparison, along with other simulation parameters, are presented in

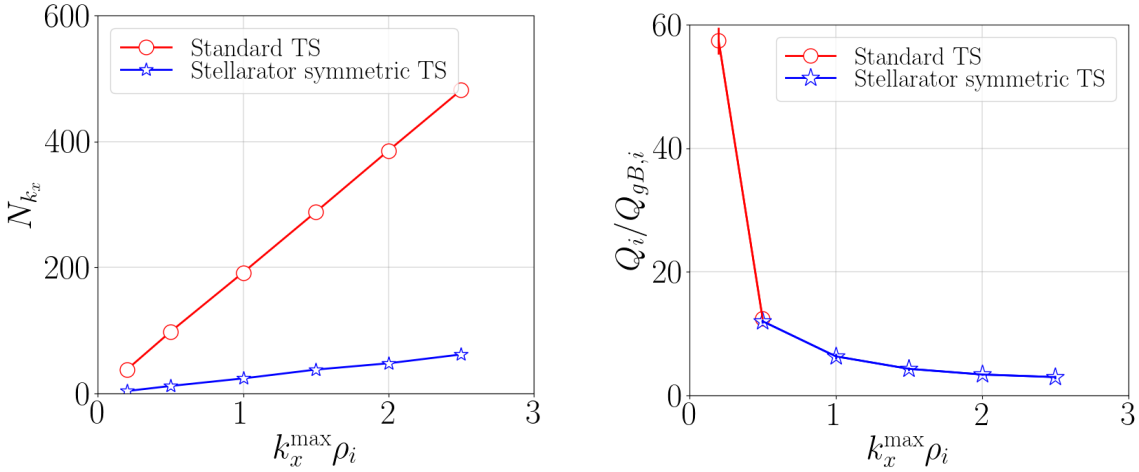

Figure 3.6: Left: Number of k_x values as a function of the maximum computed k_x using standard twist-and-shift (red empty circles) and stellarator symmetric twist-and-shift (blue empty stars) boundary conditions for flux tubes covering nearly one poloidal turn on the surface labeled by $r_0/a = 0.35$ of the standard configuration of W7-X. Right: time-averaged values of ion heat flux calculated for the surface $r_0/a = 0.35$ of the standard configuration of W7-X as a function of the maximum computed value of k_x using standard (empty red circles) and stellarator symmetric (empty blue stars) twist-and-shift boundary conditions.

table 3.2. In particular, it can be observed the CPU time required to complete each simulation, pointing out a significant performance advantage of the stellarator symmetric twist-and-shift boundary conditions, as they require approximately five times fewer CPU hours to achieve the same results compared to the standard twist-and-shift boundary conditions. Underlying the larger CPU time for the latter is the higher number of radial wavenumbers needed to cover the same range in k_y. The exact number of k_x values used for each simulation is also listed in table 3.2.

As a final nonlinear comparison, that underscores even more the significant computational disadvantages of using standard twist-and-shift boundary conditions, we conduct a similar test at the radial position $r_0/a = 0.35$ of the standard configuration of W7-X. At this location, see blue line in figure 3.1 (left), the ratio between the grid spacing in the radial and binormal directions allowed by the standard twist-and-shift boundary conditions is $|k_x|^{\min}/k_y^{\min} \approx 0.1$. In fact, figure 3.6 (left) shows the number of k_x values required to reach different values of $k_x^{\max}$ with both standard and stellarator symmetric twist-and-shift boundary conditions. It can be observed that, in order to cover the same range of radial wavenumbers, nearly one order of magnitude more modes are needed

Boundary condition	$(k_x^{\max}\rho_i, k_y^{\max}\rho_i)$	N_{k_x}	N_{k_y}	$\lvert k_x\rvert^{\min}/k_y^{\min}$	$Q_i/Q_{gB,i}$	t_{CPU} [h]
Standard	(2.0, 2.5)	386	51	0.12	-	$\gg$
Stell. symmetric	(2.0, 2.5)	47	51	0.93	3.4 ± 0.2	9936

Table 3.3: Parameters of the nonlinear simulations performed for the radial position $r_0/a = 0.35$ of the standard configuration of W7-X. From left to right: twist-and-shift boundary condition choice; maximum considered value of k_x and k_y; number of simulated values of k_x; number of simulated values of k_y; ratio between the grid spacing in k_x and k_y or, equivalently, between $|k_x|^{\min}$ and $k_y^{\min}$; value of the time-averaged ion heat flux and CPU time required to run the simulation.

for the standard than for the stellarator symmetric twist-and-shift boundary conditions, with which we maintain the ratio $|k_x|^{\min}/k_y^{\min} \approx 1$ with the range in ζ illustrated in figure 3.2 (left). This leads to a prohibitively high computational cost for the application of standard twist-and-shift boundary conditions.

Taking these restrictions into account, we calculate the ion heat flux for the surface $r_0/a = 0.35$ of the standard configuration of W7-X, with nearly identical parameters as those in previous cases. Figure 3.6 (right) presents the results obtained for the time-averaged ion heat fluxes, considering different ranges of k_x. As it can be observed, this figure only displays the results obtained using standard twist-and-shift boundary conditions up to $k_x\rho_i = 0.5$, since computing larger ranges requires simulating a number of k_x values (see figure 3.6 (left)) that exceeds the memory capacity allowed by the compute nodes. In contrast, the use of stellarator symmetric twist-and-shift boundary conditions allows the simulation of larger ranges of k_x until a converged value for the heat flux is achieved. This result, together with other parameters of the simulation, such as the CPU hours of computation are summarized in table 3.3.

To verify the accuracy of the converged ion heat flux obtained using stellarator symmetric twist-and-shift boundary conditions, we also perform a similar scan in $k_x^{\max}$ using *self-periodic* boundary conditions. This comparison, together with the description of these boundary conditions is addressed in the next section.

3.3. Self-periodic boundary conditions

We have shown that standard twist-and-shift boundary conditions impose that the global magnetic shear is proportional to Δk_x (see expression (3.14)). Therefore, a low value of $\hat{s}$ corresponds to a low value of Δk_x, or in other words, $|k_x|^{\min}$. When this value is very small, it is often approximated to zero, which leads to the imposition of self-periodicity

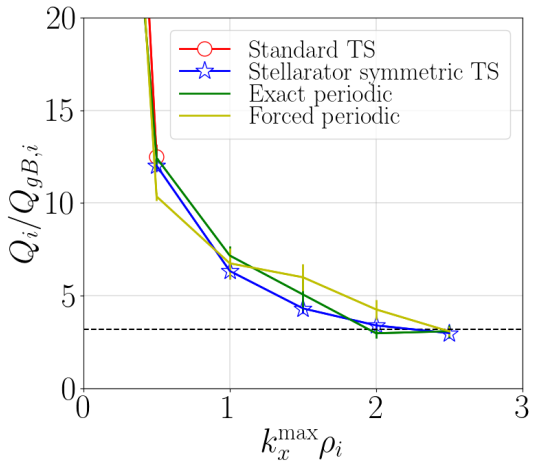

Figure 3.7: Right: zoom in to figure 3.6 (right), including the results obtained using exact periodic (in green) and forced periodic (in yellow) boundary conditions. The converged value is depicted as a dashed horizontal line.

for each mode with wavenumbers (k_x, k_y). These boundary conditions are referred to as *forced periodic* boundary conditions and, although they are formally incorrect, their use is widespread since they allow for the free specification of $|k_x|^{\min}$ and $k_y^{\min}$. We perform similar simulations to those depicted in figure 3.6 (right), but employing forced periodic boundary conditions. Their results are represented in figure 3.7.

On the other hand, in the context of stellarator symmetric twist-and-shift boundary conditions, it is also possible to adjust the extent of the flux tube in the parallel coordinate such that $|k_x|^{\min}/k_y^{\min} = 0$, as observed in expression (3.18), leading to the same condition of self-periodicity for each mode considered in the simulation without incurring any formal inaccuracies. These boundary conditions are referred to as *exact periodic* boundary conditions. In this context, we also perform similar simulations to those depicted in figure 3.6 (right), but employing exact periodic boundary conditions. Their results are represented in figure 3.7.

Therefore, In figure 3.7, which corresponds to a zoomed-in view of figure 3.6 (right), we have included the results obtained with the two self-periodic boundary conditions we described above. Hence, this figure presents the results for the normalized ion heat flux obtained with both self-periodic boundary conditions and both twist-and-shift boundary conditions analysed throughout this chapter. We observe that there are no appreciable qualitative differences between the converged values obtained for this flux.

3.4. Summary of this chapter

In this chapter, we have outlined the issues associated with the use of standard twist-and-shift boundary conditions [33] when simulating flux tubes on surfaces with a low value of global magnetic shear, $\hat{s}$. This problem becomes of critical importance when studying the inner radial positions of W7-X, since $\hat{s}$ decreases towards the core of the device, as shown in figure 3.1 (right), and becomes too small to perform simulations at a reasonable computational cost. This is because such boundary conditions force the connection of modes separated by very small distances in k_x, which is equivalent to set a very low value of $|k_x|^{\text{min}}$ (see expression 3.14).

Since one of the main goals of this thesis is to compare the results of our simulations with experimental measurements in W7-X, achieving effective resolution control in k_x and optimizing computational time have motivated us to adopt alternative boundary conditions, referred to as stellarator symmetric twist-and-shift. These were formulated in [34] and implemented in `stella` as part of the work undertaken in this thesis. We have tested this implementation and verified that using these boundary conditions improves the performance of the code when studying flux tubes at radial positions with $\hat{s} \ll 1$. Indeed, we have provided an example in which completing a simulation using standard twist-and-shift boundary conditions was not feasible, while a converged result for the ion heat flux was successfully obtained with the new implemented boundary conditions.

CHAPTER 4

Verification of `stella`. Benchmark between the codes `stella` and `GENE`

The results presented in this chapter are original from this thesis work and are mainly part of [1].

As introduced in section 1.3, the dominance of neoclassical losses in generic stellarators has traditionally led to significantly less attention being given to the study of turbulence in these devices than in tokamaks, where the turbulent channel is known to be the main source of energy and particle losses. With regard to the numerical description of microturbulent processes, while existing tokamak gyrokinetic codes ([36], [37], [38], [39], [25], [40], [41], [42]) have been extensively exploited and tested, less work has been carried out in the validation and verification of stellarator gyrokinetic codes ([43], [44], [45], [46], [47], [24], [48], [49]). In the context of verification between stellarator gyrokinetic codes, comparisons have also been reported. In [50] the growth rate of linear ion-temperature-gradient-driven modes in W7-X computed with the global particle-in-cell code `EUTERPE` and with the full flux surface version of `GENE` are compared. These simulations have later been reproduced with the global particle-in-cell code `XGC-S` in [47] and with the global version of `GENE`, `GENE-3D`, in [48]. Although valuable, as they account for global effects, these efforts are limited to linear cases and a single type of instability. In fact, at the time of undertaking this thesis, the stellarator community did not have a sufficiently comprehensive and well-documented set of benchmark tests for gyrokinetic simulations in the geometry of these devices. In this thesis, we have addressed this gap by the introduction of a reference benchmark case for stellarators. It consists on a set of linear and nonlinear gyrokinetic simulations in W7-X geometry against which present and future stellarator gyrokinetic codes can be tested and benchmarked (following the example of the tokamak community with the Cyclone Base Case

a [m]	R_0 [m]	r_0/a	B_a [T]	$\iota(r_0)$	$\hat{s}(r_0)$
0.494	5.485	0.8	2.604	0.910	-0.107

Table 4.1: Basic quantities of the magnetic configuration at the radial position selected for the simulations. From left to right: minor radius; major radius; selected radial position; reference magnetic field given by (2.47); rotational transform and global magnetic shear.

[51]). This reference case is presented in the form of a comprehensive benchmark between the flux-tube gyrokinetic code `stella` and the well-established code `GENE` [25] in W7-X geometry, standing as the verification of `stella` in a stellarator geometry.

4.1. Configuration and parameters

Despite the flux tube version of `stella` and `GENE` solve the same equations (2.41) and (2.43), presented in chapter 2, there are some differences between both codes when implementing them. Here, we will only mention the most relevant one, refering interested readers to [24] and [52] for further details. It lies on the treatment of the parallel streaming and acceleration terms in equation (2.41). As commented in section 2.4, for electrons, these terms of the gyrokinetic Vlasov equation scale up to a factor $\sqrt{m_i/m_e}$ with respect to the other terms. `GENE` treats these terms explicitly, while `stella` computes them implicitly, allowing to handle kinetic electrons using a time step size only slightly smaller than the one employed in simulations with adiabatic electrons, greatly reducing the computational cost. This will be clearly shown in section 4.2, where simulations with kinetic electrons are presented. Additionally, since at the time this study was conducted `GENE` had implemented standard twist-and-shift boundary conditions, these boundary conditions are used for both linear and nonlinear simulations performed with this code. In contrast, for `stella`, we employ a zero incoming boundary condition on the fluctuating distribution function for linear simulations[1] and standard twist-and-shift boundary conditions for the nonlinear calculations. For a comprehensive description of the twist-and-shift boundary conditions see chapter 3.

For this benchmark set of cases, we consider a high-mirror configuration, where the magnetic geometry used as input for the simulations is provided by the ideal MHD equilibrium code `VMEC` [53]. Some basic quantities of this magnetic configuration and the flux surface selected for our simulations are listed in table 4.1.

[1] In chapter 3 we showed the results of linear simulations using zero incoming boundary conditions are identical to those obtained using standard twist-and-shift boundary conditions.

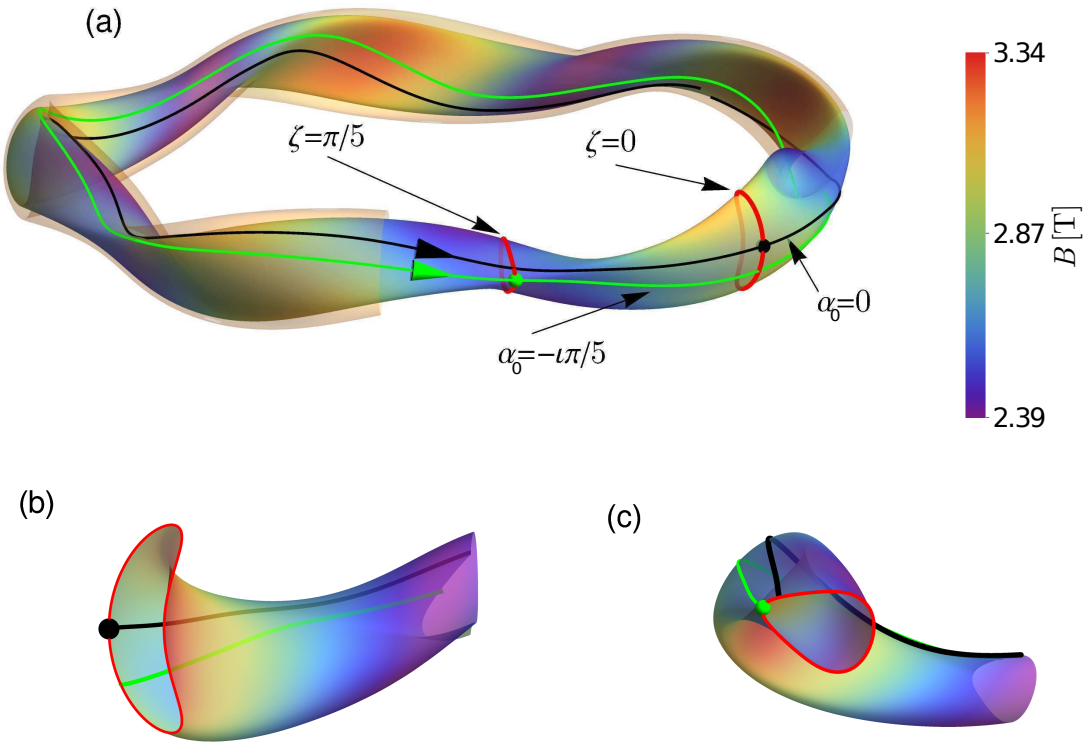

Figure 4.1: 3D view of the surface $r_0/a = 0.8$ (a), together with the field line $\alpha_0 = 0$ (solid black line), the field line $\alpha_0 = -\iota\pi/5$ (solid green line) and the last closed flux surface $r_0 = a$ as a semi-transparent halo. Details of two toroidal cuts of the flux surface $r_0/a = 0.8$ are also given, showing a bean-shaped section (b) and a triangular section (c).

Due to the flux tube geometry (see section 2.3), gyrokinetic simulations that run on different flux tubes (in general) lead to different result. Therefore, this benchmark case includes simulations in two different flux tubes, the one that extends along the widely simulated field line $\alpha_0 = 0$ and the less common choice $\alpha_0 = -\iota\pi/5$. The field line $\alpha_0 = 0$ is centered with respect to the so-called equatorial plane, $\theta = 0$, and the bean-shaped toroidal plane $\zeta = 0$, hence the name bean flux tube. The field line $\alpha_0 = -\iota\pi/5$ is centered with respect to the equatorial plane and the triangular toroidal plane $\zeta = \pi/5$, hence the name triangular flux tube. A 3D view of the flux surface $r_0/a = 0.8$ is shown in figure 4.1 (a) together with the field lines $\alpha_0 = 0$ and $\alpha_0 = -\iota\pi/5$. Figures 4.1 (b) and 4.1 (c) show some details of figure 4.1 (a). In addition, a schematic view of these field lines for the studied flux surface is given in figure 4.2, where they are represented on a

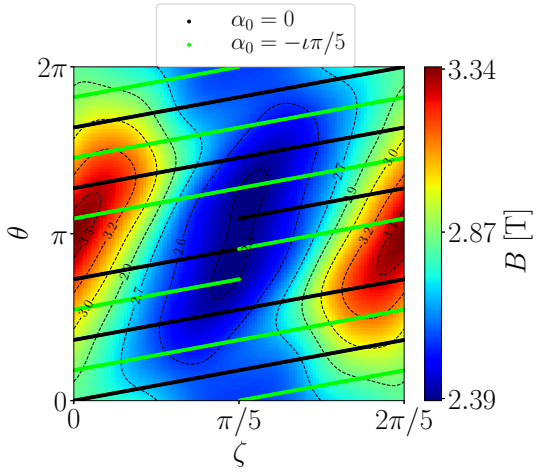

Figure 4.2: Schematic view of the magnetic field lines $\alpha_0 = 0$ (solid black line) and $\alpha_0 = -\iota\pi/5$ (solid green line) extended along the five field periods of W7-X. The magnetic field strength is represented in the background.

(θ, ζ) plane with the magnetic field strength referred to the color scale.

The geometric quantities required to solve equations (2.41) and (2.43) for the mentioned flux tubes are represented against the ζ coordinate, centered with respect to $\zeta_0 = \zeta(\theta = 0)$, in figures 4.3 (a)-(e). In figure 4.3 (a) it is observed that the magnetic field strength is symmetric with respect to $\zeta = \zeta_0$. This symmetry is also seen in the quantities $\left(\hat{\mathbf{b}} \times \nabla B\right) \cdot \nabla y$ and $(\mathbf{B} \times \boldsymbol{\kappa}) \cdot \nabla y$, which are represented in figures 4.3 (b) and 4.3 (c), respectively. In figures 4.3 (d) and 4.3 (e) we see that $(\mathbf{B} \times \boldsymbol{\kappa}) \cdot \nabla x = \left(\hat{\mathbf{b}} \times \nabla B\right) \cdot \nabla x$, as is the case for any ideal MHD equilibria.

The description of the flux tubes is complete with the specification of their length, for which we have considered the number of poloidal turns N_θ (see table 2.1). This length is chosen to correctly resolve the modes of the fluctuating electrostatic potential, $\hat{\varphi}^{tb}_{k_x k_y}$, along the flux tube. Since the localization of the electrostatic potential varies with the wavenumber, different values of N_θ have been considered in each test. The maximum and minimum values of N_θ, N_θ^M and N_θ^m, respectively, needed in each test are indicated in table 4.2, together with other parameters set for the simulations. These include the normalized ion temperature and density gradients $(a/L_{T_i}, a/L_{n_i})$, the number of divisions in the velocity grid $(N_{v_\parallel}, N_\mu)$, the time step size used for the calculation of the most unstable mode in each simulation and the different quantities compared in each test. It is important to remark that we have used $N_\zeta = 128 \times N_\theta$ divisions in the ζ domain in all simulations. Finally, the main ion species considered in every test is H^+ and $T_i/T_e = 1$.

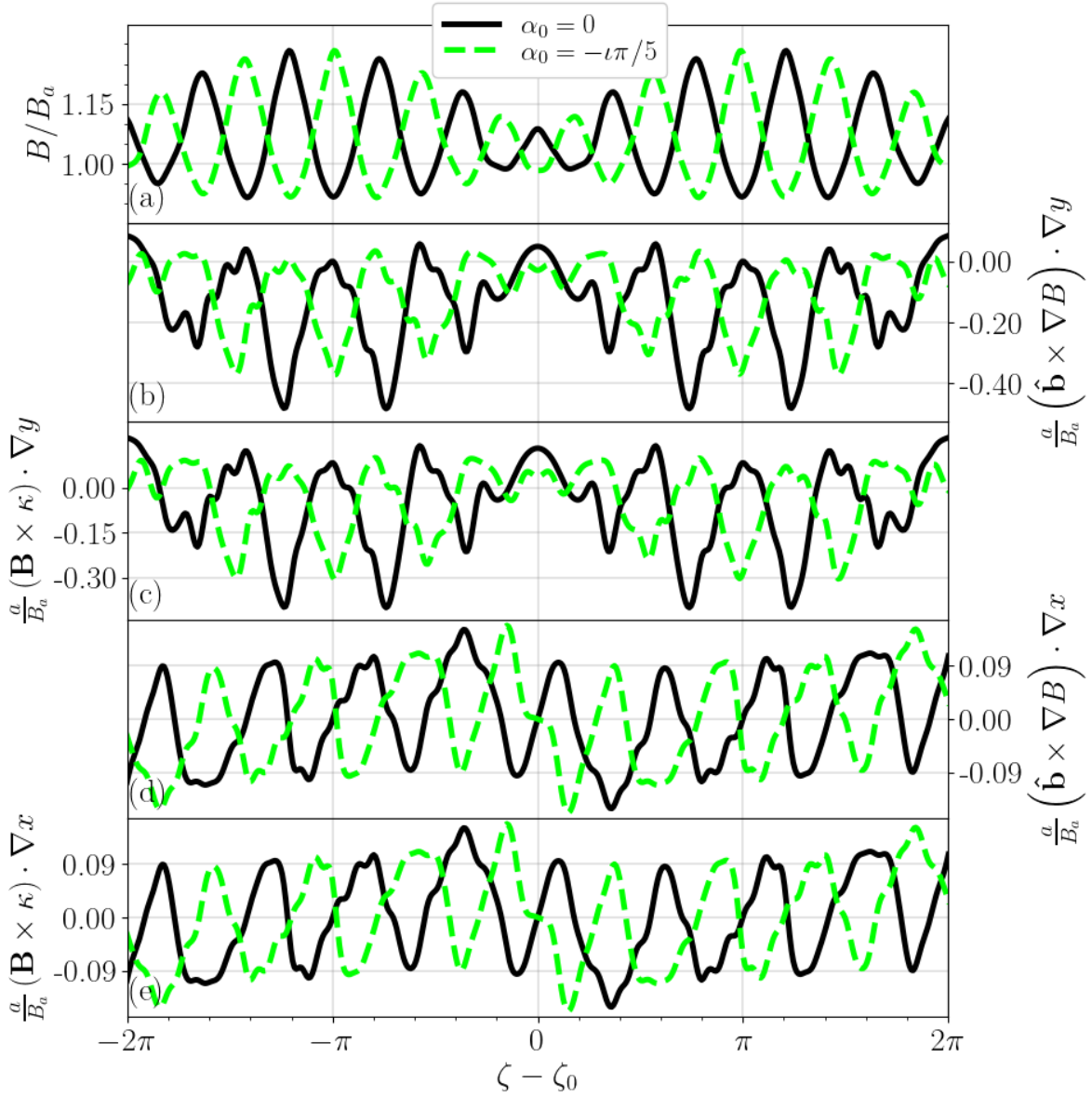

Figure 4.3: Normalized geometric quantities in the range $\zeta - \zeta_0 = [-2\pi, 2\pi]$ for the surface $r_0/a = 0.8$ along the field lines $\alpha_0 = 0$ (solid black line) and $\alpha_0 = -\iota\pi/5$ (dashed green line). The magnetic field strength is represented in (a); the projections of $\hat{\mathbf{b}} \times \nabla B$ and $\mathbf{B} \times \boldsymbol{\kappa}$ along the binormal direction are represented in (b) and (c), respectively; the projections of $\hat{\mathbf{b}} \times \nabla B$ and $\mathbf{B} \times \boldsymbol{\kappa}$ along the radial direction are represented in (d) and (e), respectively.

Test	**Flux tube**	$[N_{fp}^m, N_{fp}^M]$	a/L_{T_i}	a/L_{n_i}	$N_{v_\|\|}$	N_μ	$\Delta t v_{th,i}/a$	Compared
1.	bean	[1 , 6]	3	1	36	24	`stella` 0.15 `GENE` 0.14	$\gamma(k_x)$, $\omega_r(k_x)$ $\gamma(k_y)$, $\omega_r(k_y)$
2.	triangular	[4 , 6]	3	1	36	24	`stella` 0.15 `GENE` 0.14	$\gamma(k_x)$, $\omega_r(k_x)$
3.	bean	[2 , 8]	0	3	36	24	`stella` 0.04 `GENE` 0.004	$\gamma(k_y)$, $\omega_r(k_y)$ $\lvert\hat{\varphi}^{tb}_{k_x k_y}\rvert(\zeta)$
4.	bean	[4 , 4]	0	0	256	32	`stella` 0.15 `GENE` 0.1	$\langle\hat{\varphi}^{tb}_{k_x k_y}\rangle_\zeta(t)$
5.	bean	[1 , 1]	3	1	60	24	`stella` 0.09 `GENE` 0.09	$Q_i(t)$ $\sum_{k_y} Q_i(k_x, k_y)$ $\sum_{k_x} Q_i(k_x, k_y)$

Table 4.2: Set of parameters used in each test. From left to right: flux tube, minimum and maximum number of N_{fp}, normalized ion temperature and density gradients, number of divisions in the grid of $v_{||}$ and μ, time step size and quantities compared with both codes.

4.2. Linear Simulations

Here we present the four linear tests included in our reference case. In tests 1 and 2, ion-temperature-gradient-driven modes (ITGs) are simulated. In test 3, density-gradient-driven trapped-electron-modes (TEMs) are computed. Finally, the simulations of test 4 include the collisionless relaxation of a zonal electrostatic potential.

The linear properties of ITGs and TEMs in stellarators have been reported in a large number of studies by means of linear gyrokinetic simulations. [43] studied the ITG structure and its stability in W7-X with the global particle-in-cell code `EUTERPE`. This code has also been used to model the effects of radial electric fields on ITG modes for the geometries of W7-X and the Large Helical Device (LHD) in [54]. [45] and [55] used the code `GENE` to study the effect of changes in the density gradient and temperature ratio on ITGs and TEMs and to look at the stability properties of W7-X, comparing with other devices. `GENE` has also been used in [56] to investigate how stellarators can be optimized with respect to TEMs and in [57] to analyze the growth rate of the instability as a function of the temperature and density scales for different configurations of W7-X. A theoretical study about the effects of ITGs and TEMs in non-axisymmetric devices and, particularly in W7-X is summerized in [50]. Recently, in [30], the codes `EUTERPE`, `GENE`, `stella` and `GENE-3D` have been compared in order to assess the differences on

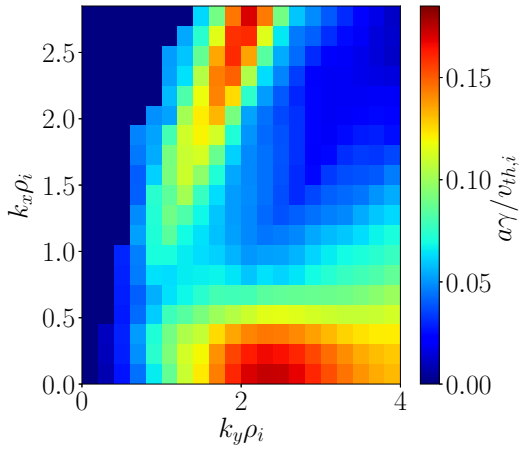

Figure 4.4: ITG stability map corresponding to test 1. It shows the growth rate computed with the code `stella` in the bean flux tube as a function of k_x and k_y.

the linear properties of ITGs and the zonal flow relaxation that arise when different computational domains, namely, flux tube, full flux surface and radially global domain, are considered.

4.2.1. Test 1. Linear ITG simulations in the bean flux tube

In this test, a linear ITG driven by a normalized ion temperature gradient $a/L_{T_i} = 3$ with a normalized ion density gradient $a/L_{n_i} = 1$ and adiabatic electrons is simulated in the bean flux tube (see table 4.2). In order to find the most unstable mode, a map containing the growth rate values γ as a function of the radial and binormal wavenumbers has been produced with `stella` and shown in figure 4.4.

Two regions of large growth rate can be observed in this map. While $N_\theta = 1$ is enough to simulate the region with $k_x\rho_i \lesssim 0.5$, $N_\theta = 6$[1] is required to simulate the one including $k_x\rho_i \gtrsim 2$ due to the localization of the mode far from the center of the flux tube. The maximum growth rate found in this map is localized at $k_y\rho_i = 2.1$. The codes `GENE` and `stella` have been used to compare the spectrum along k_y for fixed k_x and vice-versa, containing this wavenumber in both scans.

The comparison of growth rates and real frequencies as a function of k_y for fixed $k_x = 0$ is given in figures 4.5 (left) and 4.5 (right), respectively. These figures show an excellent agreement between `stella` and `GENE`. In figure 4.5 (right) it is seen that the frequency is positive for every simulated mode. ITG-driven modes are expected

[1]These lengths are the required ones if the flux tube is centered at $\zeta = 0$.

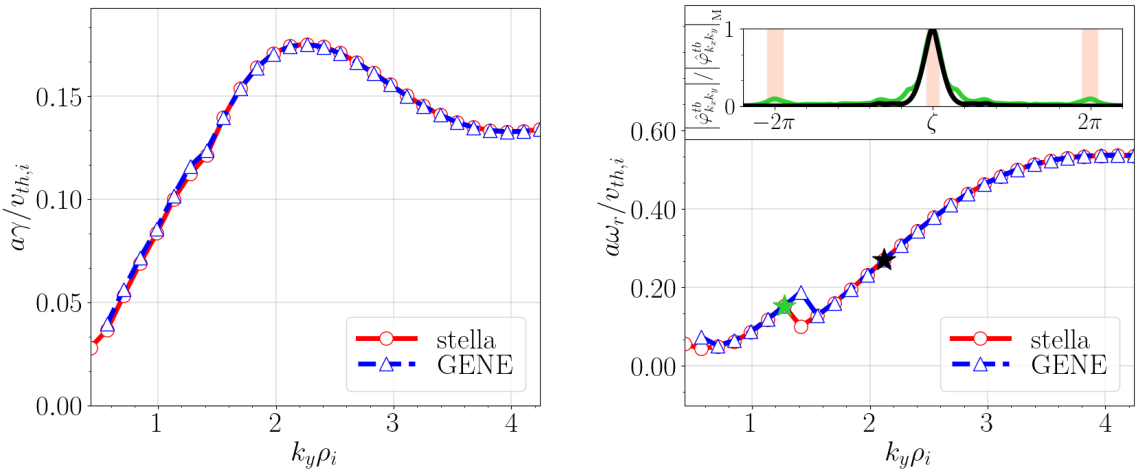

Figure 4.5: Linear growth rate (left) and real frequency (right) as a function of k_y obtained for the ITG scenario studied in test 1 using `stella` (open circles linked by a solid red line) and `GENE` (open triangles linked by a dashed blue line) in the bean flux tube. The inset of figure (right) shows the structure of the modes $(k_x\rho_i, k_y\rho_i) = (0, 1.3)$ (green line) and $(k_x\rho_i, k_y\rho_i) = (0, 2.1)$ (black line) together with some bad curvature regions (shaded in red).

to propagate in the ion diamagnetic direction, i.e. $\omega_r\omega_{*i} > 0$, where ω_{*i} is the ion diamagnetic frequency, given by

$$\omega_{*i} = -\mathrm{sgn}(\psi_a)\frac{T_i k_y}{q_i B_a L_{n_i}}. \tag{4.1}$$

As only positive values of k_y are explored in this scan, $L_{n_i} > 0$ (see table 4.2) and $\psi_a < 0$ for the selected configuration, we have $\omega_{*i} > 0$. This proves that, indeed, in this test $\omega_r\omega_{*i} > 0$, thus the studied ITG-driven modes propagate in the ion diamagnetic direction. A closer look at figure 4.5 (right) shows a discontinuity in the frequency, which is associated with a change in the mode structure, defining two different branches of the ITG instability. This can be observed in the inset of figure 4.5 (right), which represents, as a function of ζ, computations of `stella` for the modulus of the fluctuating electrostatic potential normalized to its maximum value $\left(|\hat{\varphi}^{tb}_{k_xk_y}|/|\hat{\varphi}^{tb}_{k_xk_y}|_\mathrm{M}\right)$ for the modes with $k_y\rho_i = \{1.3, 2.1\}$. These modes are strongly localized in the highlighted red bands, which correspond to *bad curvature* regions, defined as those that satisfy

$$\mathrm{sgn}(\psi_a)\frac{k_y}{B_a}\frac{\mathrm{d}T_i}{\mathrm{d}x}\left(\hat{\mathbf{b}}\times\nabla B\right)\cdot\mathbf{k}_\perp > 0. \tag{4.2}$$

If $k_x = 0$ and $k_y > 0$ these regions are the ones where the quantity shown in figure 4.3 (b), which is proportinal to $\left(\hat{\mathbf{b}}\times\nabla B\right)\cdot\nabla y$, takes positive values. This behavior of the

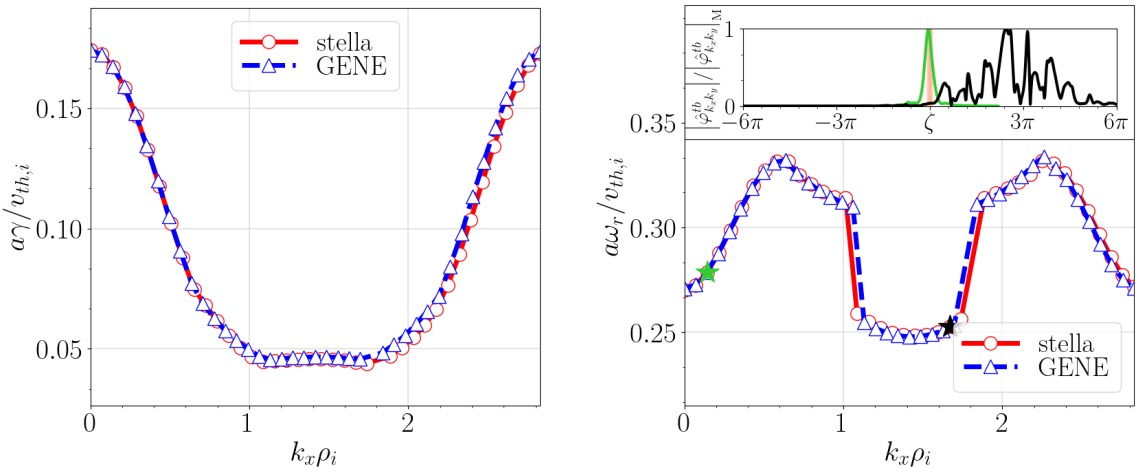

Figure 4.6: Linear growth rate (left) and real frequency (right) as a function of k_x obtained for the ITG scenario studied in test 1 using `stella` (open circles linked by a solid red line) and `GENE` (open triangles linked by a dashed blue line) in the bean flux tube. The inset of figure (right) shows the structure of the modes $(k_x\rho_i, k_y\rho_i) = (0.2, 2.1)$ (green line) and $(k_x\rho_i, k_y\rho_i) = (1.7, 2.1)$ (black line), together with a bad curvature region (shaded in red).

parallel structure of the modes is the expected one for toroidal ITG-driven modes.

The growth rates and real frequencies as a function of k_x, keeping $k_y\rho_i = 2.1$, can be seen in figures 4.6 (left) and 4.6 (right), respectively. As in the k_y-spectra, every mode studied in this scan propagates in the ion diamagnetic direction, as it can be observed in figure 4.6 (right). This figure also shows a discontinuity in the frequency, giving rise to three different branches, located at $k_x\rho_i \in (0, 1.0]$, $k_x\rho_i \in (1.0, 1.8)$ and $k_x\rho_i \in [1.8, 2.7)$. In the inset of figure 4.6 (right), the structure of the modes with $k_x\rho_i = \{0.2, 1.7\}$ computed with `stella`, belonging to the first and central branches, respectively, are represented as a function of ζ. As observed in this inset, the electrostatic potential associated to the first branch is strongly localized and $N_\theta = 1$ has been sufficient to capture the parallel structure of this mode. On the other hand, the electrostatic potential associated to the central branch spreads along ζ, making it necessary to extend the flux tube length up to $N_\theta = 6$.

4.2.2. Test 2. Linear ITG simulations in the triangular flux tube

In this test, a linear ITG instability driven by a normalized ion temperature gradient $a/L_{T_i} = 3$ with a normalized ion density gradient $a/L_{n_i} = 1$ and adiabatic electrons is simulated in the triangular flux tube (see table 4.2) .

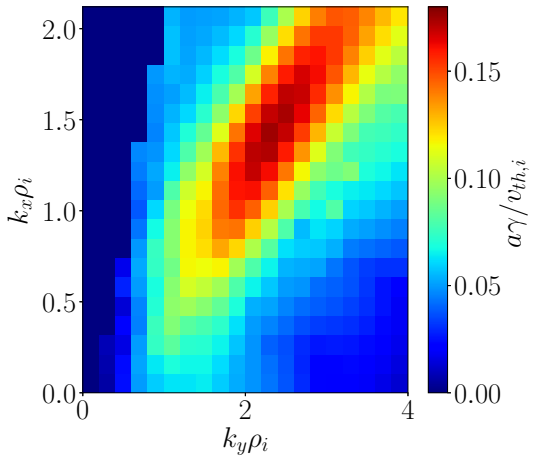

Figure 4.7: ITG stability map corresponding to test 2. It shows the growth rate computed with the code `stella` in the triangular flux tube as a function of k_x and k_y.

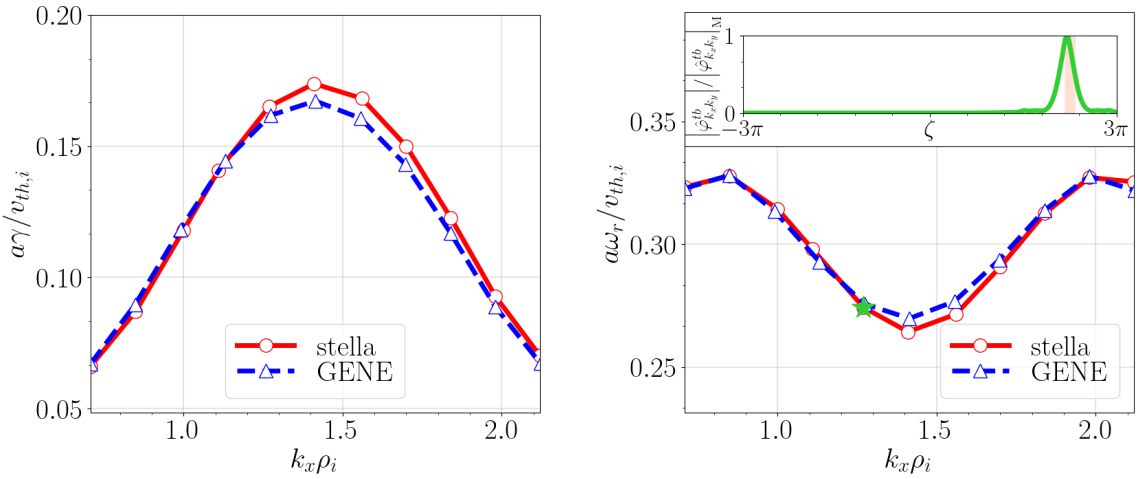

Figure 4.8: Linear growth rate (left) and real frequency (right) as a function of k_x obtained for the ITG scenario studied in test 2 using `stella` (open circles linked by a solid red line) and `GENE` (open triangles linked by a dashed blue line) in the triangular flux tube. The inset of figure (right) shows the structure of the mode $(k_x\rho_i, k_y\rho_i) = (1.2, 2.1)$ (green line) together with a bad curvature region (shaded in red).

As in the previous test, in order to find the most unstable mode, a map of the growth rate for each pair (k_x, k_y) has been produced with `stella`, see figure 4.7. As in the bean flux tube, the most unstable mode in this map is localized at $k_y\rho_i = 2.1$. Interestingly, unlike in the bean flux tube, the maximum growth rate does not correspond to a mode with $k_x = 0$. This figure also shows the triangular flux tube to be equally unstable as the bean one as $\gamma^{\max}_{\text{bean}}/\gamma^{\max}_{\text{triang}} \simeq 1$. The different localization in k_x of the most unstable modes found in figures 4.4 and 4.7 implies that special care must be taken when comparing the linear stability properties of different flux tubes.

A scan along k_x, keeping $k_y\rho_i = 2.1$, has been performed with both codes, representing the growth rates and real frequencies in figures 4.8 (left) and 4.8 (right), respectively. Although not as close as in the bean flux tube, the agreement between `stella` and `GENE` is still remarkable. As in the previous test, these modes propagate in the ion diamagnetic direction. In this scan, the localization of the electrostatic potential moves to higher values of ζ when increasing k_x, making it necessary to extend the flux tube length up to $N_\theta = 6$. The inset of figure 4.8 (right) includes the parallel structure of the Fourier coefficient with $k_x\rho_i = 1.2$ obtained with `stella`, together with the bad curvature region where this mode is localized.

4.2.3. Test 3. Linear density-gradient-driven TEM simulations in the bean flux tube

In the third test, kinetic electrons are included. Here, we study linear instabilities driven by normalized electron and ion density gradients $a/L_{n_e} = a/L_{n_i} = 3$. In order to avoid the presence of temperature gradient driven modes, the electron and ion temperature gradients have been set to zero, $a/L_{T_e} = a/L_{T_i} = 0$ (see table 4.2). Therefore, we will refer to modes studied in this test as density-gradient-driven TEMs. It is worth noting (see $\Delta t v_{\text{th},i}/a$ in table 4.2) how the mixed implicit-explicit method employed by `stella` allows a larger time step in these simulations than the explicit scheme used in `GENE`. This difference in the time step size results in a clear reduction of the total simulated time. In fact, while `GENE` has required 703 total CPU hours (5.49 hours running in 128 processors) to complete the whole simulation, `stella` has needed 76 total CPU hours (0.53 hours running in 144 processors) to simulate the same modes. The growth rate and real frequency values as a function of k_y, keeping $k_x = 0$, are shown in figures 4.9 (left) and 4.9 (right), respectively. As observed in these figures, there is a remarkable agreement between the results obtained with `stella` and `GENE`. In figure 4.9 (right) it

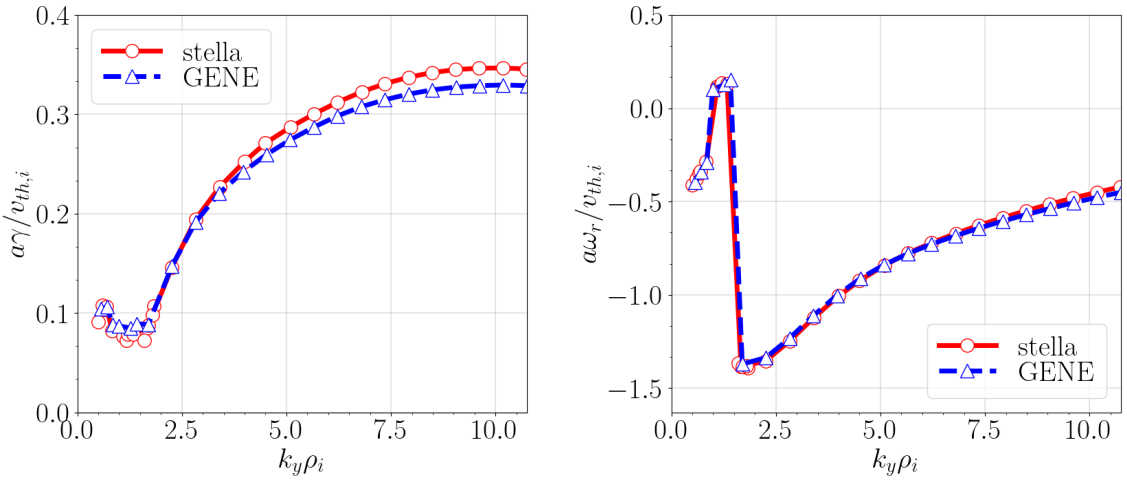

Figure 4.9: Linear growth rate (left) and real frequency (right) as a function of k_y obtained for the instabilities studied in test 3 using `stella` (open circles linked by a solid red line) and `GENE` (open triangles linked by a dashed blue line) in the bean flux tube.

can be seen that these modes can propagate both in the electron[2] and ion diamagnetic directions, depending on the wavenumber. A closer look at this figure allows to clearly distinguish three different branches. The electrostatic potential associated to the modes with $k_y\rho_i = \{0.7, 1.2, 4.7\}$, belonging each one to a different branch, are represented as a function of ζ for the whole length of the flux tube in figures 4.10 (a), (c) and (e), obtaining a good agreement between both codes. The same structures found in figures 4.10 (a), (c) and (e) are represented in figures 4.10 (b), (d) and (f), respectively, in a narrower ζ range, together with the normalized magnetic field strength and the bad curvature regions. The parallel structure of the modes belonging to the first branch, in the range $k_y\rho_i = (0, 1.1]$, has a particular shape (figures 4.10 (a) and 4.10 (b)), which can be identified with some structures discussed in [58]. To resolve this electrostatic potential we have increased the flux tube length up to $N_\theta = 8$ with both codes. In order to study the second branch, in the narrow range of $k_y\rho_i = (1.0, 1.5)$, the flux tube has been extended up to $N_\theta = 4$. Finally, $N_\theta = 2$ has been sufficient for the study of the third branch, covering from $k_y\rho_i = 1.4$ to the end of the simulated range.

4.2.4. Test 4. Linear zonal-flow relaxation in the bean flux tube

Finally, as the last linear test presented in this reference case, we perform the so-called Rosenbluth-Hinton test [59], which consists on the study of the linear collisionless time

[2]Since $q_i = e$, $q_e = -e$ and $T_i/T_e = 1$, we have $\omega_{*e} = -\omega_{*i}$, see equation (4.1).

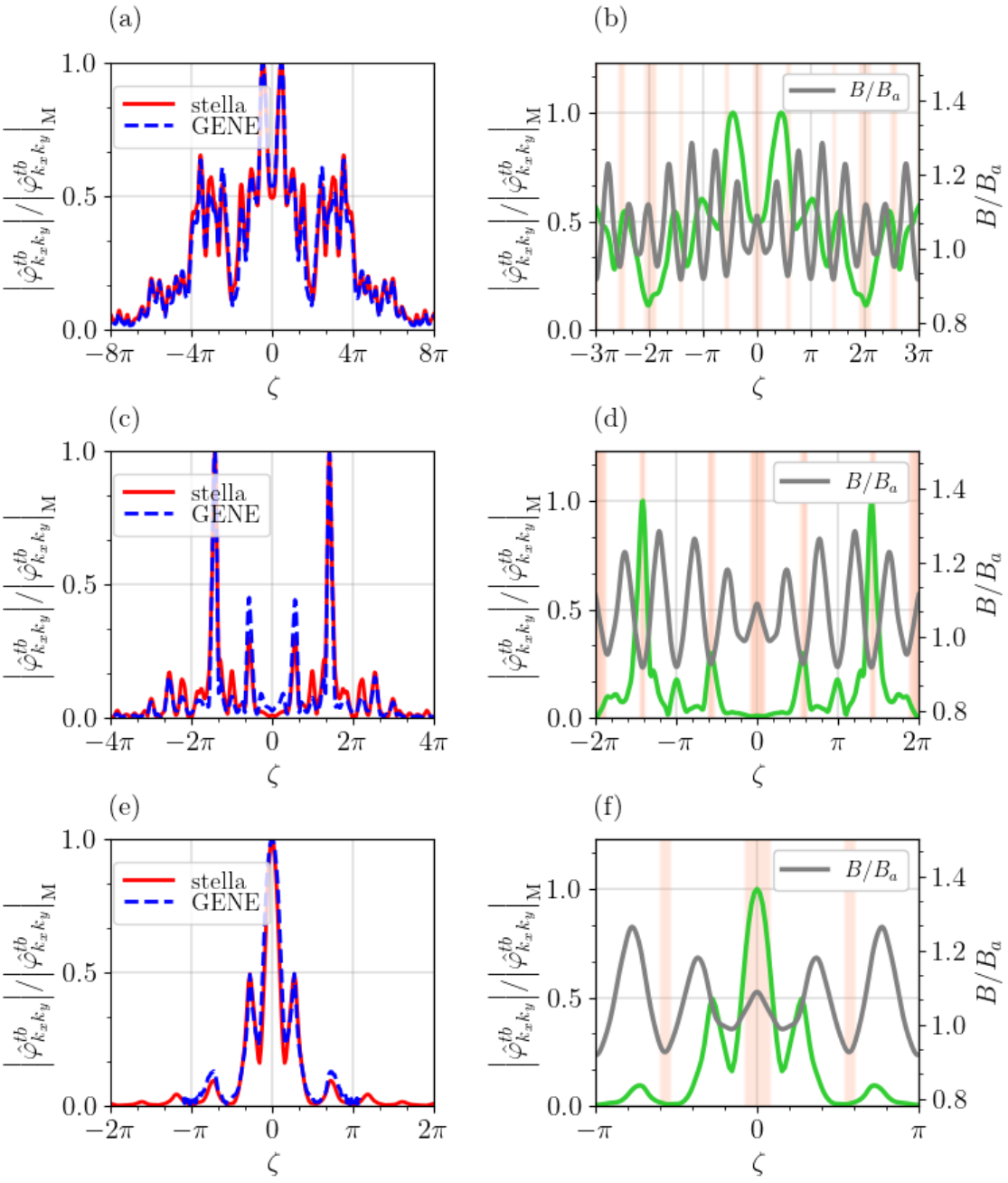

Figure 4.10: Normalized modulus of the electrostatic potential computed with `stella` (solid red line) and `GENE` (dashed blue line) as a function of ζ over the entire length of the flux tube for some modes simulated in test 3; specifically, we are representing the modes $(k_x\rho_i, k_y\rho_i) = (0, 0.7)$ (a), $(0, 1.2)$ (c) and $(0, 4.7)$ (e). The structures calculated with `stella` are shown as solid green lines in narrower ζ ranges in figures (b), (d) and (f), respectively, together with the normalized magnetic field strength (grey line) and the bad curvature regions (shaded in red).

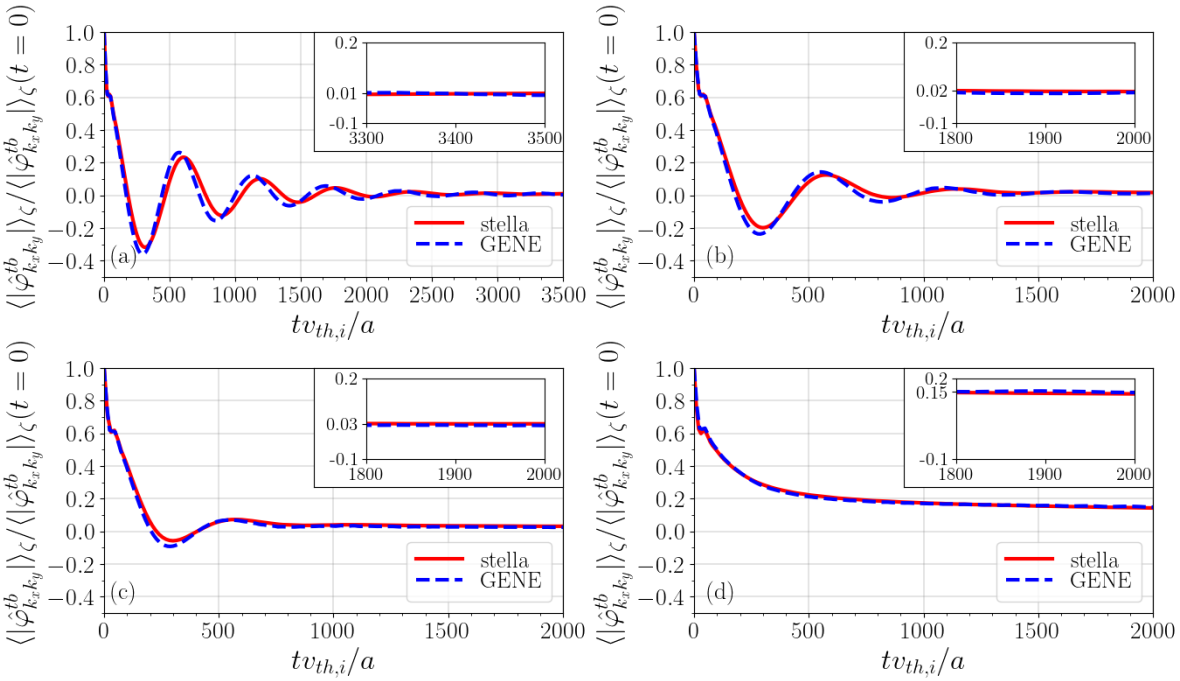

Figure 4.11: For test 4, time trace of the flux-surface averaged electrostatic potential normalized to its maximum value computed with `stella` (solid red line) and with `GENE` (dashed blue line) for the pairs $(k_x\rho_i, k_y\rho_i) = (0.05, 0)$ (a), $(k_x\rho_i, k_y\rho_i) = (0.07, 0)$ (b), $(k_x\rho_i, k_y\rho_i) = (0.1, 0)$ (c) and $(k_x\rho_i, k_y\rho_i) = (0.3, 0)$ (d). The insets show a detail of each trace at large times.

evolution of the zonal components of the electrostatic potential from their value at the initial time $t = 0$ to their value when $t \to \infty$. The zonal perturbations of the electrostatic potential φ^{tb} are constant on flux surfaces and have only radial structure. Hence, in the flux tube scheme, they correspond to the Fourier components of the potential with $k_y = 0$ and finite k_x. The theoretical study of the zonal flow response in stellarators has been addressed in [60]; [61]; [62]; [63]; [64] and [65]. In non-axisymmetric devices, the relaxation of a zonal potential perturbation typically shows a damped oscillation, reaching a stationary residual level at $t \to \infty$. The damped oscillation involves two different frequencies with different time scales: the geodesic acoustic mode (GAM) oscillation (which is also found in tokamaks) and a low frequency oscillation characteristic of the non-axisymmetric geometry of the stellarator. This characteristic low frequency oscillation of the time evolution of the potential, only predicted for $k_x\rho_i \ll 1$ ([61]; [62]; [64]), has been experimentally identified in the TJ-II stellarator in [66].

For simplicity, in the simulations included in this test $a/L_{T_i} = a/L_{n_i} = 0$ have been considered. In addition, as initial condition we have imposed $\hat{\varphi}^{tb}_{k_xk_y}(t = 0)$ to be a

Gaussian function centered in the center of the flux tube in the parallel coordinate. Four time traces of the field line-averaged electrostatic potential[3] normalized to its value at $t = 0$ have been computed and represented in figures 4.11 (a)-(d). In these figures, it can be observed how the results obtained with both codes for $k_x\rho_i \in \{0.05, 0.07, 0.1, 0.3\}$ match remarkably well. As already mentioned, the four time traces show an initial GAM oscillation at $tv_{th,i}/a \lesssim 100$, followed, except for figure 4.11 (d), by a lower-frequency damped oscillation. As observed in these figures, the frequency of the damped oscillation decreases with increasing k_x, in fact, for $k_x\rho_i = 0.3$, represented in figure 4.11 (d), this frequency is missing. The residual level of each time trace is given in the insets of these figures. These plots show that the residual value of the time traces increases with k_x.

4.3. Nonlinear simulations

As outlined in section 2.3, in flux tube nonlinear simulations, gyrokinetic codes solve equations (2.41) and (2.43) within a flux tube that extends in the radial and binormal directions, coupling the different Fourier components $\hat{\varphi}^{tb}_{k_xk_y}$. To add some context to the use of non-linear gyrokinetic simulations in the W7-X geometry, it is worth noting that the first nonlinear gyrokinetic simulations were reported by [67], where `GENE` was used to study the nonlinear ITG-driven heat flux. Since then, `GENE` has been widely used to look at the nonlinear properties of turbulence in W7-X ([68]; [50]). Then, in [69], the effects of ITG turbulent transport in different configurations of W7-X have been investigated with the global version of `GENE`, `GENE-3D` [48]. In [70] the ITG-driven heat flux has been studied using realistic plasma parameters with the global particle-in-cell gyrokinectic code `EUTERPE`. Finally, simulations carried out with `stella` with all species treated kinetically have been employed to look at the transport of impurities driven by ITG and TEM turbulence in W7-X [71] and with the aim of explaining the shape of the density profiles obtained in this device in [72].

4.3.1. Test 5. Nonlinear ITG-driven heat flux

The parameters that define the flux tube for the nonlinear test presented in this section (corresponding with the test 5 of this reference case) are listed in table 4.3. In this test, a nonlinear calculation of the ITG-driven ion heat flux, Q_i, defined by expression (3.20) is carried out considering adiabatic electrons. In addition, a normalized ion temperature gradient $a/L_{T_i} = 3$ and a normalized ion density gradient $a/L_{n_i} = 1$ are assumed (see

[3]Here, the field line average is defined as $\langle\cdot\rangle_\zeta = \int_{\zeta_{\min}}^{\zeta_{\max}}(\hat{\mathbf{b}}\cdot\nabla\zeta)^{-1}(\cdot)\mathrm{d}\zeta / \int_{\zeta_{\min}}^{\zeta_{\max}}(\hat{\mathbf{b}}\cdot\nabla\zeta)^{-1}\mathrm{d}\zeta$.

Test 5.	N_{k_x}	N_{k_y}	$\lvert k_x\rvert^{\min}\rho_i$	$k_y^{\min}\rho_i$
`stella`	51	64	0.067	0.100
`GENE`	101	64	0.047	0.071

Table 4.3: Parameters used by `stella` and `GENE` to define the flux tube in test 5. From left to right: number of modes in the radial (N_{k_x}) and binormal (N_{k_y}) directions; smallest positive wavenumber in the radial ($\lvert k_x\rvert^{\min}$) and binormal ($k_y^{\min}$) directions.

tables 4.2 and 4.3 for the values of the simulation parameters). The time trace of the ITG-driven ion heat flux computed with both codes and normalized to the ion gyro-Bohm heat flux, defined by expression (3.21), is shown in figure 4.12. Despite the different initial evolution, both traces converge to very similar values. To quantify the difference between the saturated ITG-driven heat flux obtained with each code, an average over the time interval $tv_{th,i}/a = [1500, 1900]$ has been taken and represented in the inset of figure 4.12. The results for the normalized time-averaged ITG-driven heat flux computed with `stella`, which is $Q_i/Q_{gB,i} = 2.26$ and `GENE`, which is $Q_i/Q_{gB,i} = 2.47$, represent a difference around 8.5%. This slight difference may be caused by the different resolution in the flux tube used by each code, see table 4.3.

In order to provide a more comprehensive study of these results, `stella` has been used to compute the contribution of each pair (k_x, k_y) to the time-averaged ITG-driven heat flux. In figure 4.13, it can be observed that the modes which contribute the most to the heat flux are those with $k_y\rho_i \lesssim 2.0$ and $|k_x\rho_i| \lesssim 0.5$. To compare these results with `GENE` calculations, the time-averaged ITG-driven heat flux is represented as a function of k_y, summing over k_x, in figure 4.14 (left), and as function of k_x, summing over k_y, in figure 4.14 (right). These figures show a satisfactory agreement between both codes.

Finally, for the sake of completeness, a simulation in the triangular flux tube performed with `stella` has been included in this section. The parameters selected to carry this simulation out are the ones collected in tables 4.2 and 4.3 for test 5. The time trace of the normalized ITG-driven heat flux and the contribution of each mode are represented in figures 4.15 (left) and 4.15 (right), respectively. Figure 4.15 (right) shows the saturated ITG-driven heat flux in the triangular flux tube to be $Q_i/Q_{gB,i} = 2.22$. This value is very similar to the one obtained in the bean flux tube using `stella`. The main differences between nonlinear ITG-driven heat flux calculations in both flux tubes are found in their spectrum, as it can be seen by comparing the maps given in figures 4.13 and 4.15 (right). As in the bean flux tube, the modes in the binormal direction which contribute the most to the total heat flux in the triangular flux tube are those with

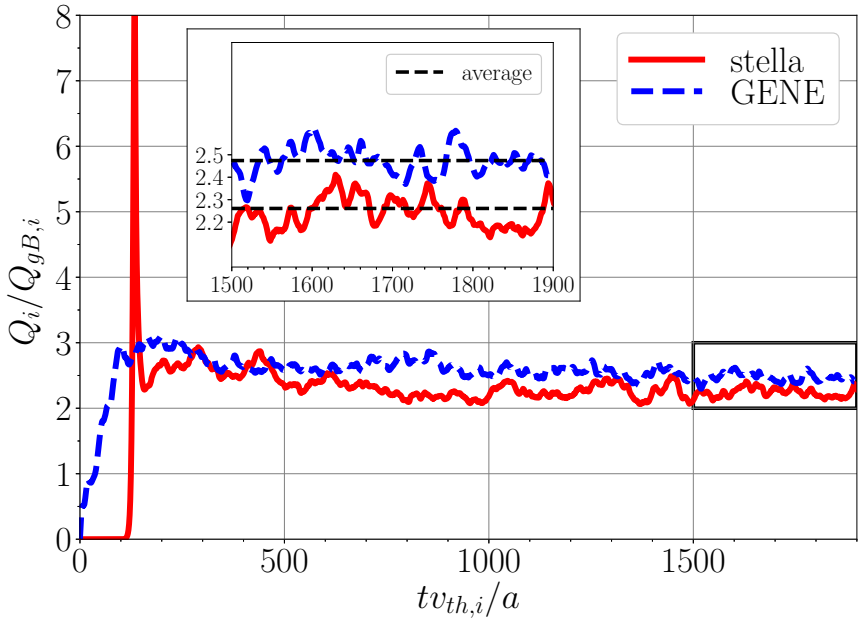

Figure 4.12: Time trace of the normalized ITG-driven heat flux computed with `stella` (solid red line) and `GENE` (dashed blue line) in the bean flux tube for the test 5 scenario. The inset shows a detail of the time interval $tv_{th,i}/a = [1500, 1900]$, with the heat flux time average given by the black dashed lines.

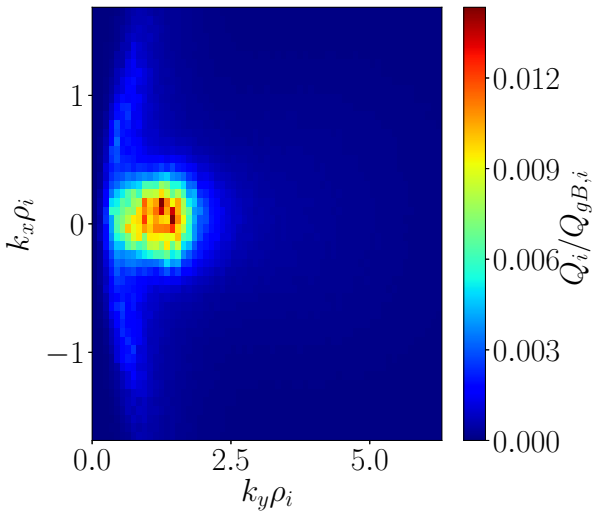

Figure 4.13: Normalized nonlinear ITG-driven heat flux computed with `stella` in the bean flux tube, averaged over the time interval $tv_{th,i}/a = [1500, 1900]$ and represented as a function of k_x and k_y.

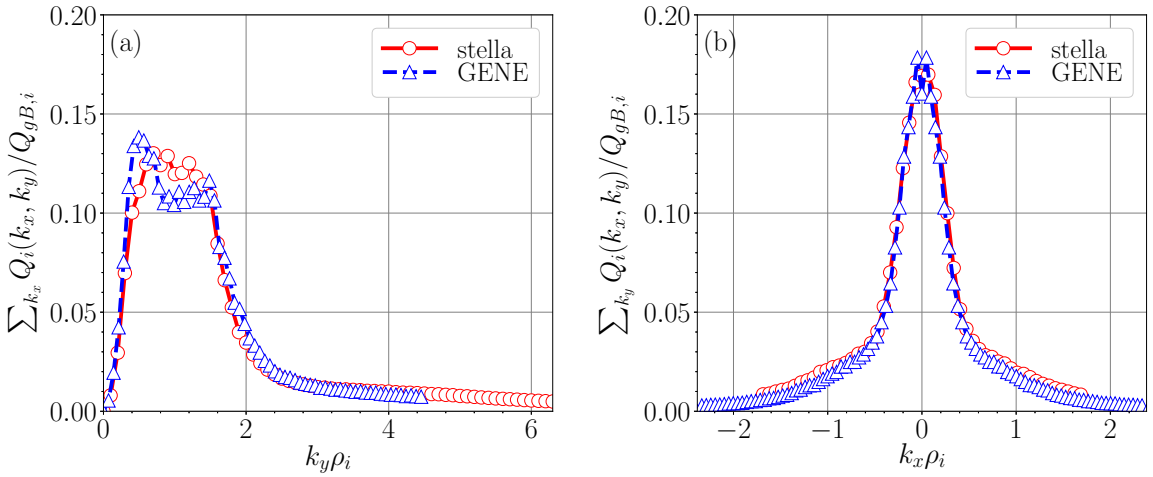

Figure 4.14: Normalized ITG-driven heat flux averaged over the time interval $tv_{th,i}/a = [1500, 1900]$ computed with `stella` (open circles linked by a solid red line) and `GENE` (open triangles linked by a dashed blue line) in the bean flux tube. It is represented as a function of k_y, summing over k_x (left) and as a function of k_x, summing over k_y (right).

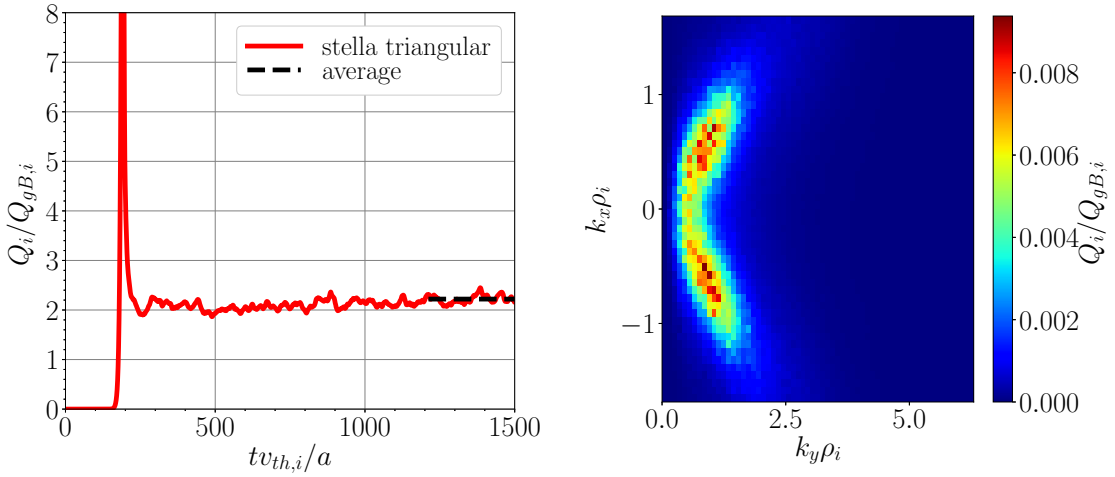

Figure 4.15: Left: time trace of the normalized ITG-driven heat flux computed with `stella` in the triangular flux tube, together with the heat flux time average over $tv_{th,i}/a = [1200, 1500]$, represented with a black dashed line. Right: this time-averaged ITG-driven heat flux is also represented as a function of k_x and k_y.

Flux tube	$t_{\mathrm{wall-clock}}$ [h]	N_{proc}	t_{CPU} [h]
Bean	`stella` 161 `GENE` 24	`stella` 288 `GENE` 1920	`stella` 46368 `GENE` 46080
Triangular	`stella` 115	`stella` 288	`stella` 33120

Table 4.4: Time required to run the nonlinear simulations with `GENE` in the bean flux tube and with `stella` in the bean and triangular flux tubes. From left to right: simulation wall-clock time in hours, number of processors and total CPU time in hours.

$k_y\rho_i \lesssim 2.0$. However, in contrast with the results obtained for the bean flux tube, modes in the radial direction with $0.5 \lesssim |k_x\rho_i| \lesssim 1.5$ give a large contribution to the total heat flux in the triangular flux tube.

For a complete view of these nonlinear simulations, we have indicated in table 4.4 the simulation wall-clock time ($t_{\mathrm{wall-clock}}$) required to produce these results. This table also includes the number of processors (N_{proc}) in which the codes have been running and the total CPU time (t_{CPU}) that each simulation has taken, defined as $t_{\mathrm{CPU}} = N_{\mathrm{proc}} \times t_{\mathrm{wall-clock}}$. As expected, since we have assumed adiabatic electrons in these nonlinear calculations, both codes require similar t_{CPU} to perform the presented nonlinear test, as it is shown in table 4.4. On the other hand, the time difference when simulating the triangular and bean flux tubes with `stella` is attributable to the different time ranges explored with each simulation, see figures 4.12 and 4.15 (left).

4.4. Summary of this chapter

Due to the increasing interest in stellarator gyrokinetic modelling, fostered by the results of W7-X first experimental campaigns, it is desirable to have a sufficiently complete, documented and well verified set of linear and nonlinear gyrokinetic simulations in W7-X geometry against which present and future stellarator gyrokinetic codes can be tested and benchmarked. Such a set of simulations has been provided in this thesis in the form of a comprehensive benchmark between the codes `stella` and `GENE`.

This benchmark, consisting of five different tests, has been carried out in a fixed-boundary high-mirror configuration of W7-X. The linear part of the benchmark has been presented in tests 1 to 4. ITG instabilities have been studied in the bean and triangular flux tubes of W7-X in tests 1 and 2, respectively. Comparing these results, it can be concluded that both flux tubes are equally unstable, but the largest growth

rates are found at different radial wavenumbers. TEM instabilities driven by density gradients have been studied in test 3, where it has been shown how the mixed implicit-explicit method used by `stella` allows to use larger time steps than explicit codes for simulations with kinetic electrons, resulting in a clear reduction of the total CPU time. In these three tests, the structure of the electrostatic potential associated with each instability has been given and the growth rate and real frequency values obtained with `stella` and `GENE` have been successfully compared. In test 4, different time traces of the zonal electrostatic potential relaxation have been compared. Finally, the nonlinear ITG-driven heat flux and its spectrum have been calculated in test 5 in the bean flux tube with both codes and, for completeness, in the triangular flux tube with `stella`. The computed energy fluxes are similar in both flux tubes, although the radial modes that give the largest contribution to the total heat flux are different.

The results presented in this section verify successfully the code `stella` in the stellarator geometry. This verification increases the confidence in the code to address problems like those discussed in chapter 5. They include comparisons between the code results and experimental measurements and predictions of quantities that are valuable for future experimental campaigns.

CHAPTER 5

Comparison of local gyrokinetic simulations with Doppler reflectometry (DR) measurements in W7-X

The results presented in this chapter are original from this thesis work and are mainly part of [2].

With the code `stella` verified through the benchmark presented in chapter 4 and with the succesful implementation of stellarator symmetric twist-and-shift boundary conditions presented in chapter 3, we can use the code to compute experimentally relevant quantities. This allows, on one hand, the interpretation of experiments and, on the other hand, the validation of the gyrokinetic theory underlying the simulations. Furthermore, given the limited number of studies that directly compare numerical gyrokinetic simulations with measurements of turbulent fluctuations in stellarators and, in particular, in W7-X, it is interesting to address a comprehensive study of these fluctuations. Specifically, we present a numerical characterization of the turbulent electrostatic fluctuations in W7-X and compare the results with the existing experimental measurements [73] obtained with the Doppler reflectometer (DR) system [74, 73, 75, 76] installed in this device.

In addition, we will offer predictions for quantities that can be compared in the future, including the frequency spectra of density fluctuations and those of the zonal components of turbulent $E \times B$ flows. Finally, apart from the objective of comparing the simulations results against the DR measurements, we will perform comparisons between linear and nonlinear simulations and discuss their similarities and differences.

5.1. The DR system in W7-X. Correspondence between k_y and $k_\perp^{DR}$

The Doppler Reflectometry system (DR) is a diagnostic capable of providing a measure of the amplitude of density fluctuations ($|\delta n|$)[1] and rotation velocity ($u_\perp$) for a selected perpendicular wavenumber ($k_\perp^{\mathrm{DR}}$). In what concerns to the amplitude of density fluctuations, the DR system measures the backscattered power, denoted by S, of a microwave beam whose point of reflection at the so-called cut-off density determines the specific point of measurement. For low turbulence levels, this backscattered power is proportional to the squared amplitude of the density fluctuations $S \propto (\delta n)^2$ [77]. On the other hand, the measure of the perpendicular rotation velocity, $u_\perp$, can be inferred from the shifted frequency of the backscattered wave due to the Doppler effect.

Particularizing to the W7-X stellarator, the DR system installed in this device employs a fixed line-of-sight geometry, meaning that the direction of the microwave beam relative to the plasma is constant. Radial resolution is achieved by varying the microwave frequency, which changes the cut-off layer location within the plasma, thereby selecting different radial positions of measurement. During the first operational phase (OP1) of W7-X, the DR system has been limited to measure in regions close to the bean-shaped toroidal plane ($\zeta = 0$) of the plasma. Although this limits the spatial coverage, it provides valuable insights into the plasma behaviour at this specific region. A typical DR microwave launching direction, the accessed measurement points (determined using ray-tracing techniques), a schematic representation of one of the reflected rays, and the poloidal cross-section of the plasma where the DR system is installed are depicted in figure 5.1.

To enable a comprehensive comparison between the quantities measured by the DR system on W7-X (in particular $|\delta n|$ nearby $\zeta = 0$) and the results obtained with `stella`, it is necessary to establish a correspondence between the perpendicular wavenumbers measured by the DR ($k_\perp^{DR}$) and those computed with the code. Given that the direction of measurement of the DR system is perpendicular both to the radial direction and to the magnetic field [73], an unitary vector pointing along the direction of measurement can be defined as $\mathbf{e}^{\mathrm{DR}} = \mathbf{B} \times \nabla x / |\mathbf{B} \times \nabla x|$. Consequently, the perpendicular wavenumber of measurement can expressed as

$$k_\perp^{\mathrm{DR}} = \mathbf{k}_\perp \cdot \mathbf{e}^{\mathrm{DR}} = \mathbf{k}_\perp \cdot \frac{\mathbf{B} \times \nabla x}{|\mathbf{B} \times \nabla x|}, \tag{5.1}$$

[1] It is worth noting that, with the aim of avoiding multiple superscripts on a single quantity, we have used the symbol δ to denote fluctuations in this chapter, rather than the superscript tb used throughout this thesis.

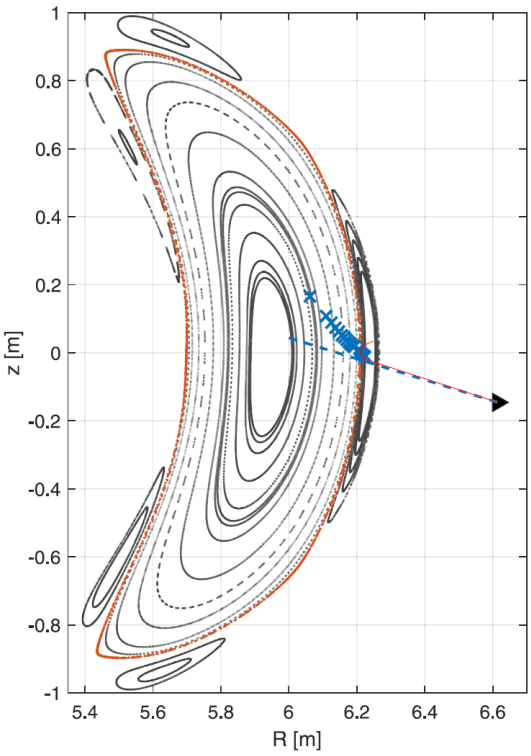

Figure 5.1: Bean cross section of the standard configuration of W7-X. The DR antenna position is represented as a black triangle and the launching direction of the microwave beam as a dashed blue line. The set of points marked with blue crosses indicates the positions where the beam is reflected and the DR diagnostic performs its measurements. These points can be obtained applying ray-tracing techniques. Figure taken from [73].

or, in terms of the coordinates and normalizations used by the code (see expressions (2.35) and (2.45))

$$k_y \rho_i = \sqrt{2 m_i T_i} \frac{|\nabla x|}{eB} k_\perp^{\mathrm{DR}}, \tag{5.2}$$

where, as usually in this thesis, we have taken into account that the wavenumbers defined in `stella` are normalized with the ion thermal gyroradius given by (2.54). Expression (5.2) implies that, given a certain set of plasma profiles and a certain wavelength of the microwave beam launched by the DR system, the corresponding value of the normalized binormal component of the wavevector defined by the code changes with the spatial location. This is due to the modification from point to point of the geometric quantities $|\nabla x|$ and B, as well of $T_i(x)$.

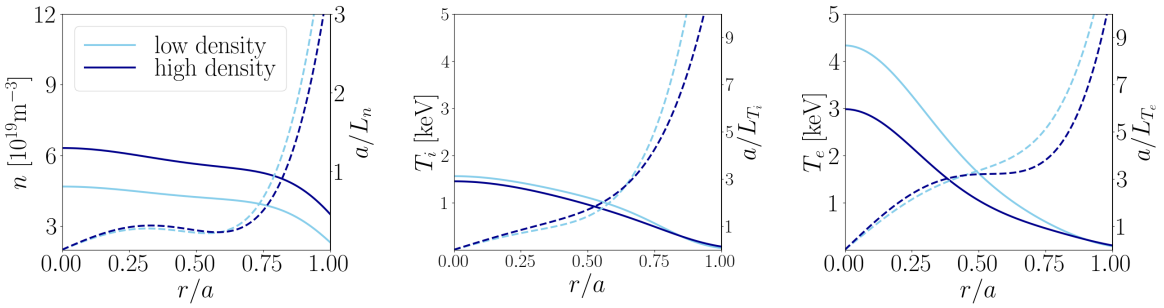

Figure 5.2: Radial profiles for the low (light blue) and high (dark blue) density scenarios. From left to right: density (solid line) and its normalized gradient (dashed line), ion temperature (solid line) and its normalized gradient (dashed line), electron temperature (solid line) and its normalized gradient (dashed line).

5.2. Plasma scenario and simulation settings

The selected plasma parameters for this study correspond to two gas puff-fueled electron cyclotron resonance heated (ECRH) scenarios, without neutral bean injection (NBI) for heating, from the OP1.2b campaign of W7-X. We have chosen these specific discharges given that analyses of the amplitude of the fluctuations measured with the DR system have been presented in [73], which allows a straightforward comparison of the calculations obtained with `stella` and those already published. These discharges are labeled by #180920.13 and #180920.17, both using the same heating power of $P_{ECRH} \simeq 4.7$ MW without electron cyclotron current drive (ECCD) and with the former featuring a lower density than the latter. Hence, they will be referred to as *low density scenario* (#180920.13) and *high density scenario* (#180920.17).

The profiles of density (n), ion temperature (T_i) and electron temperature (T_e) of these two scenarios, obtained as fits to the experimental data, are represented in figure 5.2. In this figure, the normalized gradients of these quantities (see expression (2.53)) are also depicted. In order to cover the radial range of measurement of the DR system reported in [73], five radial positions, labeled by $r_0/a = \{0.5, 0.6, 0.7, 0.8, 0.9\}$, have been considered for the simulations. The specific values of the plasma profiles and their normalized gradients for the selected radial locations are listed in table 5.1.

The magnetic geometry used as input for the simulations is provided by the ideal MHD equilibrium code `VMEC` [53]. This configuration is an example of a standard W7-X equilibrium with effective minor radius $a = 0.514$ m, major radius $R_0 = 5.513$ m, and, for normalization purposes, see equation (2.47), $B_a = 2.28$ T. In addition, the global shear, defined as it is in (3.15) and ι (see equation (2.30)) profiles corresponding to this config-

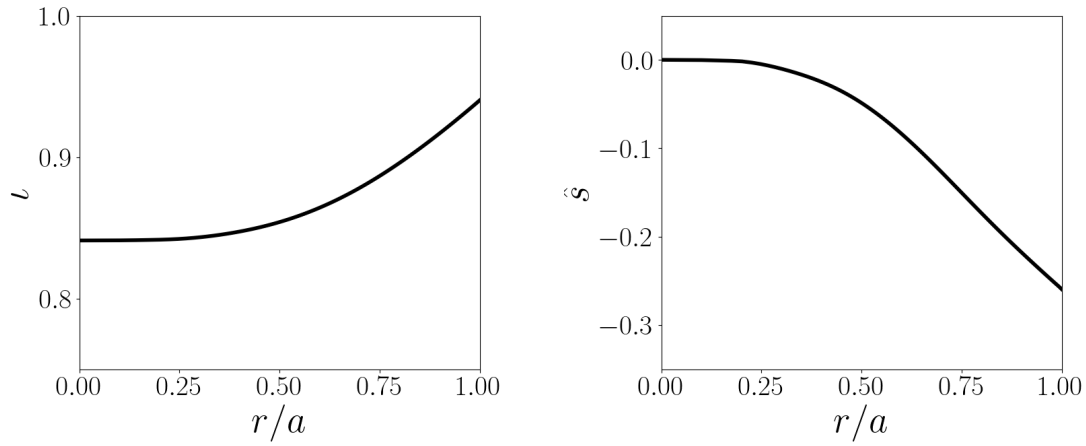

Figure 5.3: Radial profiles of ι (left) and $\hat{s}$ (right) of the standard configuration considered throughout this study.

uration are represented in figure 5.3. As anticipated in chapter 3, it is shown that as one moves towards the magnetic axis of this device, the global magnetic shear represented in figure 5.3 (right) becomes critically low. To avoid the restrictions imposed by the standard twist-and-shift boundary conditions (see expression (3.14) and related discussion), the implementation of the stellarator symmetric twist-and-shift boundary conditions has been indispensable. Consequently, these boundary conditions are employed in this study.

In figure 5.4, the measurement positions for the high density scenario[2] at the radial locations considered in the gyrokinetic simulations, obtained using the ray-tracing code `TRAVIS` [78], are represented with stars. The restrictions of the flux tube formalism and the boundary conditions used in this study to access those measurement locations should also be noted. As described in chapter 3, the use of stellarator symmetric twist-and-shift boundary conditions restricts the selected flux tubes to stellarator symmetric ones, i.e. those fulfilling $B(\theta, \zeta) = B(-\theta, -\zeta)$. In W7-X, the suitable flux tubes are then the bean and the triangular flux tubes, see section 4.1 for a description of these flux tubes. The intersections of these two flux tubes, assuming they extend one turn in the toroidal direction, with the bean-shaped toroidal plane of W7-X can also be found in figure 5.4. The bean flux tube position $(\theta, \zeta) = (0, 0)$ provides the spatial location nearest to the positions of measurements of the DR system. Therefore, the information to compare against the measurements of the DR system will be extracted from that flux tube at $(\theta, \zeta) = (0, 0)$. In addition, concerning the perpendicular wavenumber of measurement,

[2]The measurement positions for the low density scenario are very close to those represented in figure 5.4.

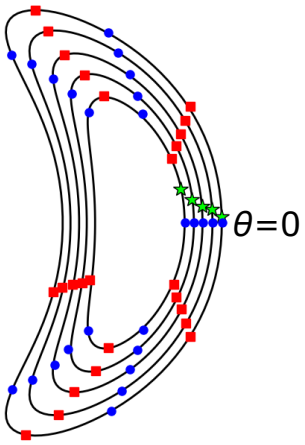

Figure 5.4: Points belonging to the bean (blue dots) and triangular (red squares) flux tubes of W7-X that lay on the plane $\zeta = 0$. The measurement positions for the high density scenario, obtained with `TRAVIS` for the radial locations considered in the gyrokinetic simulations, are represented as stars.

the relationship between $k_\perp^{\mathrm{DR}}$ and $k_y\rho_i$ (see expression (5.2)) is represented as a function of the radial coordinate in figure 5.5 for a wide range of $k_\perp^{\mathrm{DR}}$. The $k_\perp^{\mathrm{DR}}$ values selected in the experiment (included in table 5.1 and reported in [73]) are indicated in figure 5.5 with white squares.

Finally, for the simulations performed in this chapter, we have considered a phase space grid of $\{92 \times 36 \times 12 \times 59 \times 45\}$ points in $\{\zeta, v_\parallel, \mu, k_x, k_y\}$ and maximum and minimum values of k_x and k_y, $(k_x^{\max}\rho_i, k_y^{\max}\rho_i) \simeq (2.5, 4.5)$, and $(|k_x|^{\min}\rho_i, k_y^{\min}\rho_i) \simeq (0.1, 0.1)$, respectively.

5.3. Radial dependence of density fluctuations: comparison between `stella` results and DR measurements

As introduced at the beginning of this chapter, the amplitude of the density fluctuations measured by the DR system is one of the quantities suitable to be compared against the calculations carried out with `stella` since the code provides, at each instant and each position along the flux tube, the decomposition in Fourier space of the density fluctuations (δn) on the plane perpendicular to the magnetic field. Thus, as any fluctuating quantity, the density fluctuations over the plane of the flux tube perpendicular to the

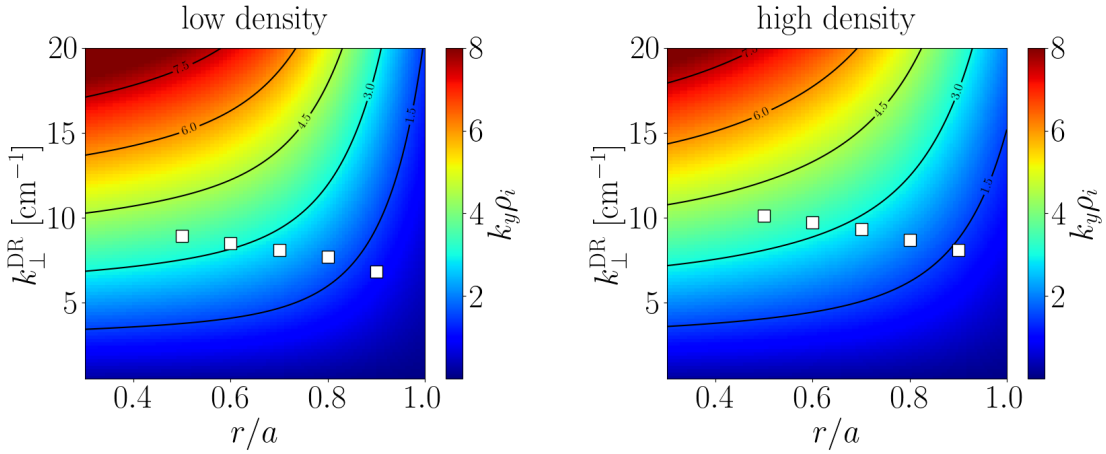

Figure 5.5: Relation between $k_y\rho_i$ and $k_\perp^{\mathrm{DR}}$ as a function of the radial position for a wide range of $k_\perp^{\mathrm{DR}}$. These plots are the result of evaluating expression (5.2) at $(\theta, \zeta) = (0, 0)$ considering the T_i profiles represented in figure 5.2 for the low (left) and high (right) density scenarios. The white squares represent the perpendicular wavenumbers measured by the DR system at each radial location.

r_0/a	discharge	n [10^{19}m^{-3}]	a/L_n	T_i [keV]	a/L_{T_i}	T_e [keV]	a/L_{T_e}	$k_\perp^{\mathrm{DR}}$ [cm^{-1}]
0.5	low	4.23	0.22	1.11	1.41	1.62	3.35	8.9
	high	5.63	0.25	0.96	1.70	1.04	3.20	10.1
0.6	low	4.14	0.23	0.93	2.18	1.13	3.78	8.5
	high	5.51	0.22	0.78	2.33	0.75	3.23	9.7
0.7	low	4.01	0.43	0.70	3.75	0.75	4.51	8.1
	high	5.36	0.34	0.59	3.43	0.54	3.47	9.3
0.8	low	3.75	1.02	0.42	6.70	0.45	5.97	7.7
	high	5.09	0.76	0.39	5.32	0.37	4.37	8.7
0.9	low	3.21	2.25	0.17	11.81	0.22	8.73	6.8
	high	4.52	1.73	0.20	8.48	0.22	6.63	8.1

Table 5.1: Local parameters used in the simulations at each radial position for the low and high density scenarios. From left to right: density, normalized density gradient, ion temperature, normalized ion temperature gradient, electron temperature, normalized electron temperature gradient and perpendicular wavenumber measured by the DR system.

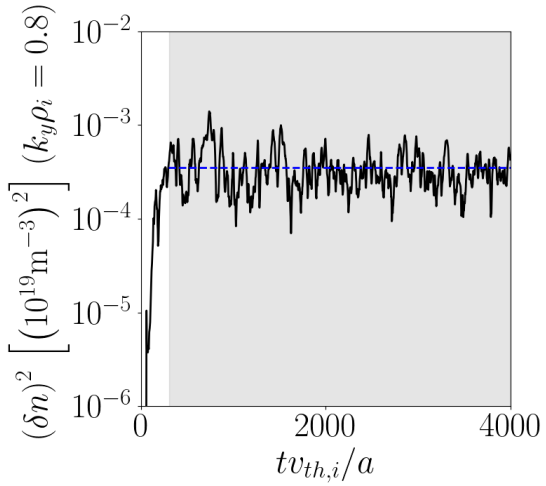

Figure 5.6: Time evolution of $(\delta n)^2(k_y\rho_i = 0.8)$ at $r_0/a = 0.6$ in the high density scenario. The range considered for the time-average is represented by the shadowed area and the mean value of this quantity is indicated with the horizontal dashed line.

magnetic field centered with respect to r_0 and α_0 can be expressed as

$$\delta n\,(x, y, \zeta, t) = \sum_{k_x, k_y} \widehat{\delta n}_{k_x k_y}(\zeta, t) \exp[\mathrm{i}(k_x x + k_y y)]. \tag{5.3}$$

As depicted in section 5.2, the simulated positions nearest to the measurement locations are those of the bean flux tube with $\zeta = 0$. Once $|\widehat{\delta n}_{k_x k_y}|^2(\zeta = 0, t)$ is obtained from the simulations, the quantity to compare against the DR system measurements is post-processed as follows. First, for each pair of wavenumbers (k_x, k_y), the spectrum in k_y is obtained by summing over k_x as

$$(\delta n)^2\,(k_y, t) = \sum_{k_x} \left|\widehat{\delta n}_{k_x k_y}\right|^2 (\zeta = 0, t). \tag{5.4}$$

Second, we time-average each $(\delta n)^2(k_y, t)$ over the saturated nonlinear phase, obtaining the time-averaged squared density fluctuations, $\langle(\delta n)^2\rangle_t(k_y)$. For illustrative purposes, figure 5.6 shows the time trace of $(\delta n)^2$ for the mode $k_y\rho_i = 0.8$, which is the one with the largest amplitude at $r_0/a = 0.6$ in the high density scenario.

In figure 5.7, the results obtained for $\langle(\delta n)^2\rangle_t$ for the five scanned radial positions and for the two scenarios are represented as a function of $k_y\rho_i$. The values of k_y that correspond to the wavenumbers of measurement of the DR system, that we denote by $k_y^{\mathrm{DR}} = k_y(k_\perp^{\mathrm{DR}})$, are also indicated with vertical dashed lines in these plots. It can be observed that the DR system, depending on the radial location, measures very disparate

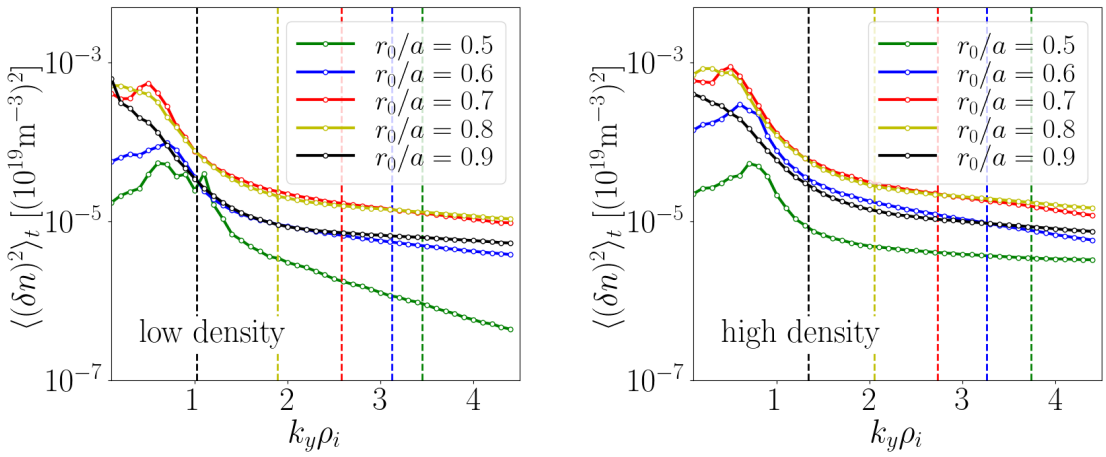

Figure 5.7: k_y spectrum of the time-averaged squared density fluctuations, $\langle(\delta n)^2\rangle_t$, obtained with `stella` for the low (left) and high (right) density scenarios. The dashed vertical lines indicate the wavenumber measured by the DR system, $k_\perp^{\mathrm{DR}}$, at each radial position.

values of $k_y\rho_i$. Whereas at $r_0/a = 0.9$ the system accesses nearly scales with $k_y\rho_i \sim 1$, as r_0 decreases it explores different regions of the spectrum, reaching up to $k_y\rho_i \sim 3.5$.

Finally, considering the squared density fluctuations for each radial location at the specific value of k_y accessed by the diagnostic,

$$(\delta n)^2_{\mathrm{DR}} = \langle(\delta n)^2\rangle_t(k_y = k_y^{\mathrm{DR}}), \tag{5.5}$$

the comparison against the backscattered power, S (which we recall, is proportional to $(\delta n)^2_{DR}$) can be carried out. In figure 5.8 (left), the numerical results obtained with `stella`, $(\delta n)^2_{\mathrm{DR}}$, are represented as a function of the radial coordinate, while in figure 5.8 (right), the measurements of S obtained with the DR system (reported in [73]) can be found. It is important to note that the DR measurements represented in figure 5.8 (right) are expressed in dB, but the reference normalization value is unknown. Hence, S [dB] $\propto 10\log_{10}(\delta n)^2_{\mathrm{DR}} + C$, with C an arbitrary constant. For this comparison, C has been chosen to make $S\,(r_0/a = 0.5) = 10\log_{10}(\delta n)^2_{\mathrm{DR}}\,(r_0/a = 0.5) + C$ or, equivalently, to set the lowest value of the numerical and experimental results at the same level. It can be observed that the numerical results shown in figure 5.8 (left) and the measurements in figure 5.8 (right) exhibit a monotonic increase of the squared density fluctuations with r/a. In addition, the difference between their minimum and maximum values is approximately 15 dB in both cases. Finally, the numerical and experimental results corresponding to the low density scenario show lower turbulent fluctuations than those

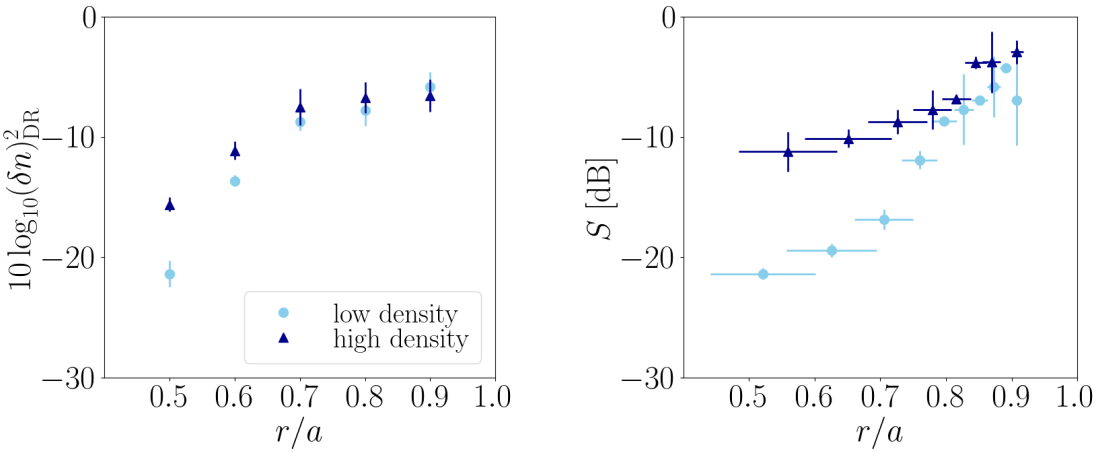

Figure 5.8: Squared amplitude of the density fluctuations as a function of the radial coordinate for the low (light blue circles) and high (dark blue triangles) density scenarios. Left: Numerical results of $(\delta n)^2_{\mathrm{DR}}$ obtained with `stella`. The error bars represent the standard deviation from the mean value evaluated over the saturated nonlinear phase. Right: backscattered power measured by the DR system.

of the high density scenario. These features, in particular the monotonic increase of the density fluctuations towards the edge, result, partially, from the fact that the DR system measures, as the radial position changes, at different locations of the k_y spectrum, as we anticipated in figure 5.7 and related discussion. Indeed, the density fluctuations integrated both in k_x and k_y, i.e $\delta n = \sqrt{\sum_{k_y} \langle (\delta n)^2 \rangle_t}$, loses the monotonic increasing behaviour with r/a, as figure 5.9 illustrates, for the two discharges analyzed. In that figure, one can observe that the integrated density fluctuations have a maximum at nearly $r_0/a = 0.8$ and ranges between 2 and 8×10^{19} m^{-3}. This picture aligns remarkably well with what Phase Contrast Imaging (PCI) techniques and `GENE` [25] simulations have reported for similar plasmas in W7-X [79].

Returning to the comparison between `stella` calculations and DR measurements of figure 5.8, the numerical results do not exhibit the significant reduction that the measurements do for the low density scenario in the range $r/a \sim [0.6, 0.7]$. A possible source of discrepancy could be that the bean flux tube at $\zeta = 0$ does not correspond to the exact spatial measurement position of the DR system (see figure 5.4). We have addressed this aspect computing poloidal profiles of $(\delta n)^2_{DR}$ by interpolating its value at the points of the plane $\zeta = 0$ crossed by the been and triangular flux tubes (see figure 5.4). These interpolations are represented in figure 5.10. In this figure it is shown that, when the poloidal deviation from the bean flux tube at $\zeta = 0$ is considered, the

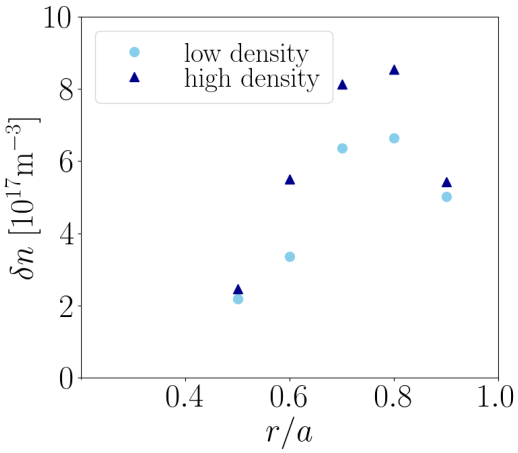

Figure 5.9: Amplitude of the density fluctuations integrated over k_x and k_y computed with `stella` as a function of the radial coordinate for the low (light blue circles) and high (dark blue triangles) density scenarios.

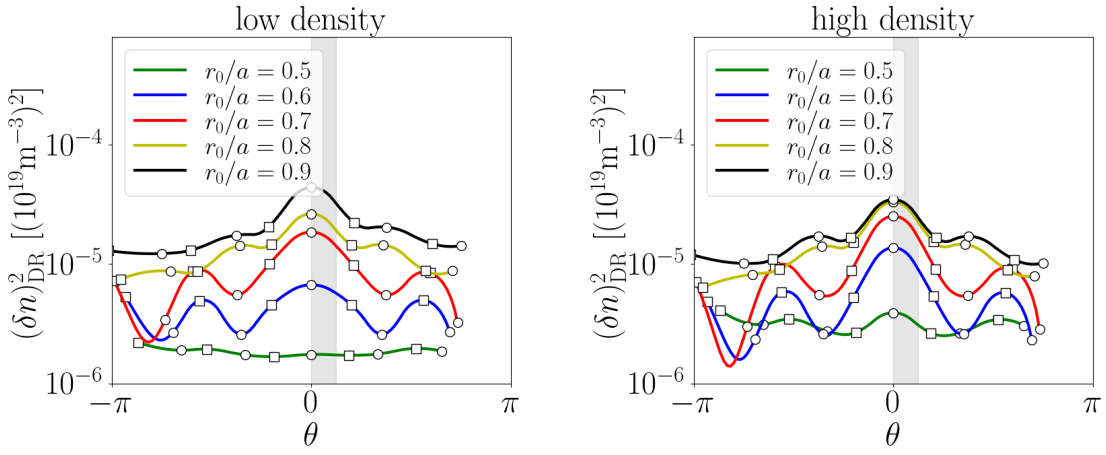

Figure 5.10: $(\delta n)^2_{\mathrm{DR}}$ as a function of the poloidal coordinate θ for a fixed $\zeta = 0$ for the low (left) and high (right) density scenarios. Computed as an interpolation of the $(\delta n)^2_{\mathrm{DR}}$ calculated for the bean (circles) and triangular (squares) flux tubes. The shadowed region shows approximately the maximum deviation of the DR measurement position from $\theta = 0$.

numerical results do not change more than a 20% between $(\delta n)^2_{\mathrm{DR}}$ evaluated at the exact measurement location and that at $(\theta, \zeta) = (0, 0)$. Such differences are negligible compared to the quantitative discrepancy between the simulations and the experimental measurements shown in figure 5.8. With respect to the model used, possible extensions, such that accounting for the full flux surface geometry [76] and, in that case, including the radial electric field as well, might be worth addressing in order to attempt in the future a better agreement. With regard to collisions, which, as in every simulation presented in this thesis, have been neglected, the normalized ion collision frequency between $r/a = 0.5 - 0.8$ (considering ions and electrons with one thermal speed) is $a\nu_i/v_{th,i} \sim 1.3 \times 10^{-3} - 1 \times 10^{-2}$. This value is significantly smaller than the growth rates of most unstable electrostatic instabilities, typically of a few tenths in units of $a/v_{th,i}$. Exceptionally, at the position $r/a = 0.9$, $a\nu_i/v_{th,i} \sim 3.5 \times 10^{-2}$ in both scenarios. Electron collision frequencies are higher though ($a\nu_e/v_{th,i} \sim 0.1 - 3$), nevertheless electrons do not seem to play a prominent role except at the innermost studied position (see section 5.5).

5.4. Numerical characterization of fluctuations in the frequency domain. Predictions for future analysis with the DR system

With the density fluctuations already compared in the real space, we extend our analysis to the frequency domain. The aim is to complete the characterization of the fluctuations with features that can be inferred from the time evolution of S and $u_\perp$ measured by the DR system. In particular, these features correspond to the frequency spectrum of the squared amplitude of density fluctuations, that will be presented in section 5.4.1, and the frequency spectrum of the zonal component of the $E \times B$ flow, discussed in section 5.4.2. Future analyses, that automate the measurement of highly time-resolved traces of S, will enable a straightforward comparison against the fluctuation frequency spectra provided in section 5.4.1. On the other hand, the installation in a different toroidal sector of a second DR system —whose data acquisition and analysis will extend during the second W7-X operation phase (OP2)— will allow to identify oscillations in $u_\perp$ of zonal origin to be verified against the spectra presented in section 5.4.2.

5.4.1. Frequency spectra of density fluctuations

In section 5.3, we have addressed the comparison between the radial dependence of the squared amplitude of the density fluctuations computed with `stella` and those measured by the DR system. In that case, a time average of $(\delta n)^2(k_y, t)$ was performed.

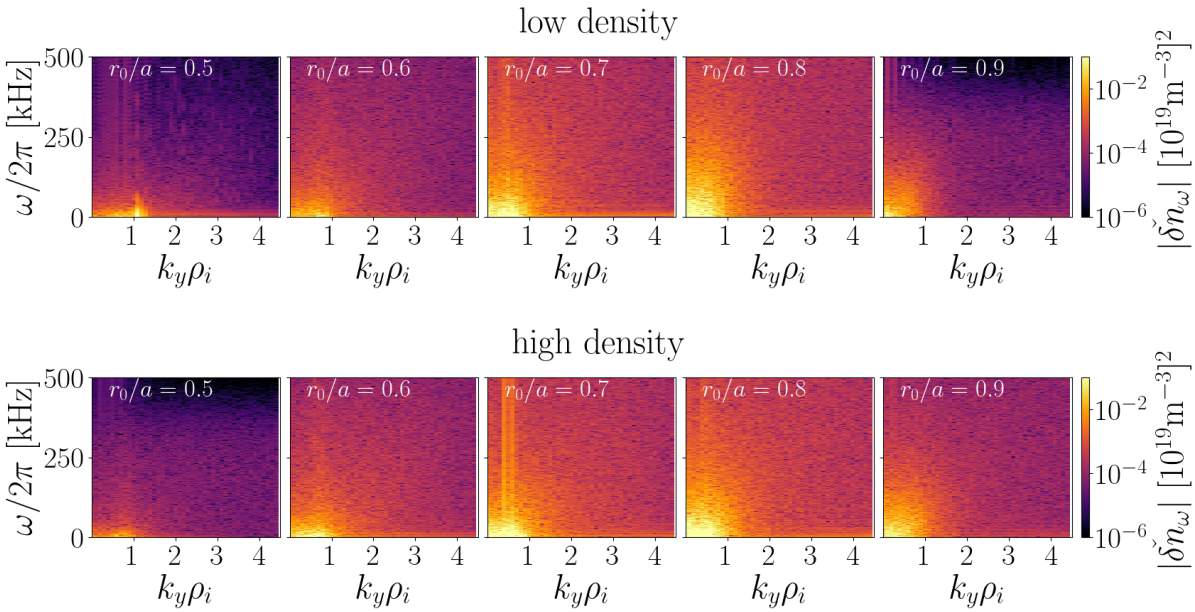

Figure 5.11: Frequency spectra of $(\delta n)^2$ for the low (top) and high (bottom) density scenarios computed with `stella` as function of k_y.

If, instead, the time dependent squared density fluctuations, $(\delta n)^2(k_y, t)$, are considered and a Fourier transform in t is taken[3], we can write

$$(\delta n)^2(k_y, t) = \sum_\omega \check{\delta n}_\omega(k_y) \exp(-\mathrm{i}\omega t), \tag{5.6}$$

leading to the frequency spectrum of the squared density fluctuations. Note that the obtained frequency spectrum differs from the power spectral density of δn. In this section, we assume that once the time evolution of the backscattered power $S(t)$ of the beam launched by the system is known —since $S(t)$ is proportional to the $(\delta n)^2$— the comparison of the frequency spectra of the experimental signal S and the numerically obtained $(\delta n)^2$ is straightforward. In figure 5.11, the amplitude of $\check{\delta n}_\omega$ is represented as a function of the frequency ω and k_y. We define the amplitude of the Fourier harmonics $\check{\delta n}_\omega$ for $k_y = k_y^{\mathrm{DR}}$ as

$$\check{\delta n}_{\mathrm{DR}}(\omega) = \left|\check{\delta n}_\omega\right|(k_y = k_y^{\mathrm{DR}}). \tag{5.7}$$

Figure 5.12 shows $\check{\delta n}_{\mathrm{DR}}(\omega)$ for the two scenarios under consideration. In general, for all radial positions, the spectrum is broad and extends a few hundreds of kHz. Above frequencies of that order of magnitude, an abrupt drop of the amplitude is observed.

[3]Following the definitions introduced in section 2.4, the coefficients of the Fourier expansions in t are expressed as $\check{A}$. On the other hand, the coefficients of the expansions in (x, y) are expressed as $\hat{A}$.

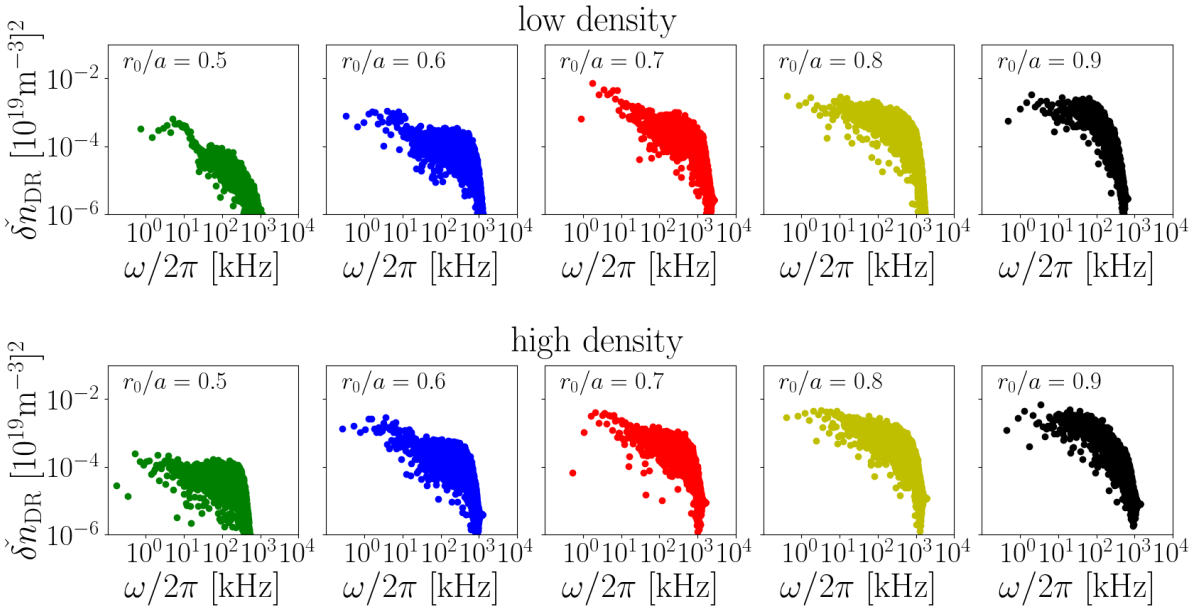

Figure 5.12: Density spectra of $\delta\check{n}_{\mathrm{DR}}$ computed with `stella` for the low (top) and high (bottom) density scenarios for the case $k_y = k_y^{\mathrm{DR}}$.

Below $\omega/2\pi \sim 100$ kHz, the spectra are rather flat. However, for some radial positions — $r_0/a = \{0.5, 0.6, 0.7\}$ in the low density scenario and $r_0/a = \{0.6, 0.7\}$ in the high density one— peak values of the amplitude are observed for frequencies such that $\omega/2\pi \lesssim 10$ kHz. After a similar Fourier analysis of $S(t)$, the experimental frequency spectra could be compared against those represented in figure 5.12.

5.4.2. Frequency spectra of zonal flow fluctuations

Since the zonal perturbations of the electrostatic potential are constant on flux surfaces (see section 4.2.4), with a second Doppler reflectometer looking on the same flux surface as the first one but at a different toroidal location, it would be possible to identify zonal oscillations in W7-X. Specifically, common frequencies found in the time evolution of $u_\perp(t)$ obtained by each DR could be identified with zonal $E \times B$ flow fluctuations projected along the measurement direction of the system, $\mathbf{e}^{\mathrm{DR}}$. In this subsection we address the characterization of these frequencies.

Following the convections used in this thesis, in which the fluctuating component of the $E \times B$ velocity is defined by expression (2.14) and the fluctuating electrostatic potential in a flux tube can be expressed, for each radial position, as (2.34), the zonal

fluctuating $E \times B$ velocity reads

$$\delta \mathbf{v}_E^{ZF}(x,\zeta,t) = \frac{(\mathbf{B}\times\nabla x)}{B^2}\sum_{k_x} \mathrm{i}k_x \widehat{\varphi}^{tb}_{k_x k_y=0}(\zeta,t)\exp(\mathrm{i}k_x x). \tag{5.8}$$

In order to obtain this expression, we have considered the zonal modes of the potential, i.e., those with $k_y = 0$. Taking the projection of $\delta\mathbf{v}_E^{ZF}$ along the direction of measurement of the DR diagnostic, $\mathbf{e}^{\mathrm{DR}}$, we can compute the zonal flow fluctuations expected to contribute to the total perpendicular flow measured by the DR system, $\delta v_\perp^{\mathrm{ZF}} = \langle \delta\mathbf{v}_E^{ZF}\cdot \mathbf{e}^{\mathrm{DR}}\rangle_\zeta$. Explicitly

$$\delta v_\perp^{\mathrm{ZF}}(x,t) = \mathrm{i}\sum_{k_x} k_x \left\langle \frac{|\nabla x|}{B}\widehat{\varphi}^{tb}_{k_x k_y=0}(\zeta,t)\right\rangle_\zeta \exp(\mathrm{i}k_x x). \tag{5.9}$$

Taking a Fourier transform of $\delta v_\perp^{\mathrm{ZF}}(x,t)$ in t,

$$\delta v_\perp^{\mathrm{ZF}}(x,t) = \sum_\omega \check{\delta v}_{\perp\omega}(x)\exp(-\mathrm{i}\omega t), \tag{5.10}$$

allows us to obtain the frequency spectrum, $\check{\delta v}_{\perp\omega}$, for each x position of our flux tube. To improve the statistics of our results, we perform an average along x, defined for each frequency of the spectrum as

$$\check{\delta v}^{\mathrm{ZF}}_{\perp\omega} = \frac{1}{N_{k_x}}\sum_j \check{\delta v}_{\perp\omega}(x_j). \tag{5.11}$$

Figure 5.13 shows the amplitudes of $\check{\delta v}^{\mathrm{ZF}}_{\perp\omega}$ normalized to their maximum value, eliminating the mode $\omega = 0$ (which corresponds to the time-averaged value). For the radial positions $r_0/a = \{0.7, 0.8, 0.9\}$ dominant frequencies cluster in the range $\omega/2\pi \sim [5, 10]$ kHz. For the innermost positions, $r_0/a = \{0.5, 0.6\}$, dominant frequencies group around the lower boundary of ω with no clear peak in the spectra. In figure 5.13, we have also depicted with vertical dashed lines the frequency ω_0 above which the amplitude $|\check{\delta v}^{\mathrm{ZF}}_{\perp\omega}|$ is always smaller than half the maximum value in each case. It can be observed that, for all radial positions, frequencies $\omega_0/2\pi \leq 20$ kHz dominate the spectrum of the fluctuating zonal $E \times B$ flow.

5.5. Comparisons between linear and nonlinear calculations of φ^{tb}

The analysis presented in this study has focused, so far, on numerical quantities that can be directly compared against DR measurements. Nevertheless, aspects beyond that

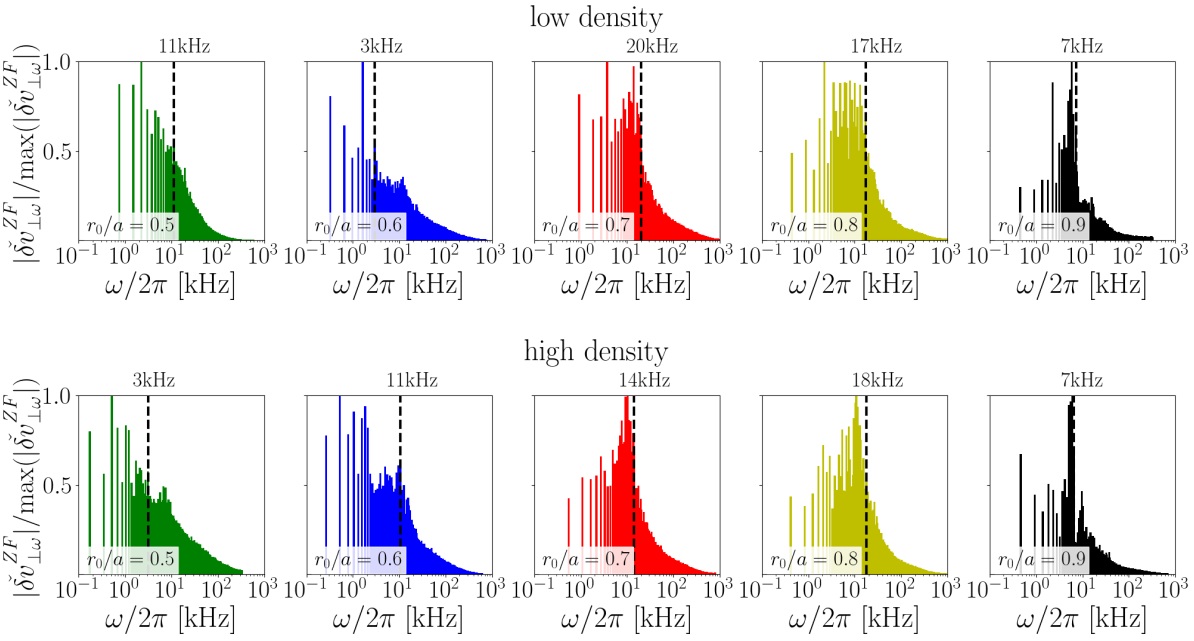

Figure 5.13: Normalized amplitudes $|\delta\check{v}^{\mathrm{ZF}}_{\perp\omega}|$ computed with `stella` and represented as a function of the frequency ω for the low (top) and high (bottom) density scenarios. The dashed vertical lines indicate the frequency ω_0 such that $|\delta\check{v}^{ZF}_{\perp\omega_0}| < \max(|\delta\check{v}^{ZF}_{\perp\omega}|)/2$ for all $\omega > \omega_0$.

comparison, like the nature of the background turbulence, its localization along the flux tube or its linear properties have not been discussed yet. In the present section we briefly address some of these characteristics, comparing the linear and nonlinear frequency spectra of the fluctuating electrostatic potential in order to assess to what extent linear frequencies remain during the nonlinear phase.

From the saturated phase obtained from nonlinear simulations, we can calculate the frequency spectrum for each k_y mode of $\langle\varphi^{tb}\rangle_\zeta$, summing over all k_x components as

$$\sum_{k_x}\langle\widehat{\varphi}^{tb}_{k_x k_y}\rangle_\zeta(t) = \sum_{\omega}\check{\varphi}_\omega(k_y)\exp(-\mathrm{i}\omega t). \tag{5.12}$$

This Fourier decomposition allows a direct comparison between the nonlinear frequency spectrum of $\langle\varphi^{tb}\rangle_\zeta$ and the real frequencies ω_r obtained from linear simulations. Figure 5.14 shows, as a function of ω, the amplitude of $\check{\varphi}_\omega$ normalized to the largest value found (at a certain $\omega = \omega^M$) for each k_y, i.e.

$$\overline{|\varphi_\omega|}(k_y) = \frac{|\check{\varphi}_\omega|(k_y)}{|\check{\varphi}_{\omega=\omega^M}|(k_y)}. \tag{5.13}$$

In addition, this figure also depicts the linear frequencies obtained from k_y scans for a

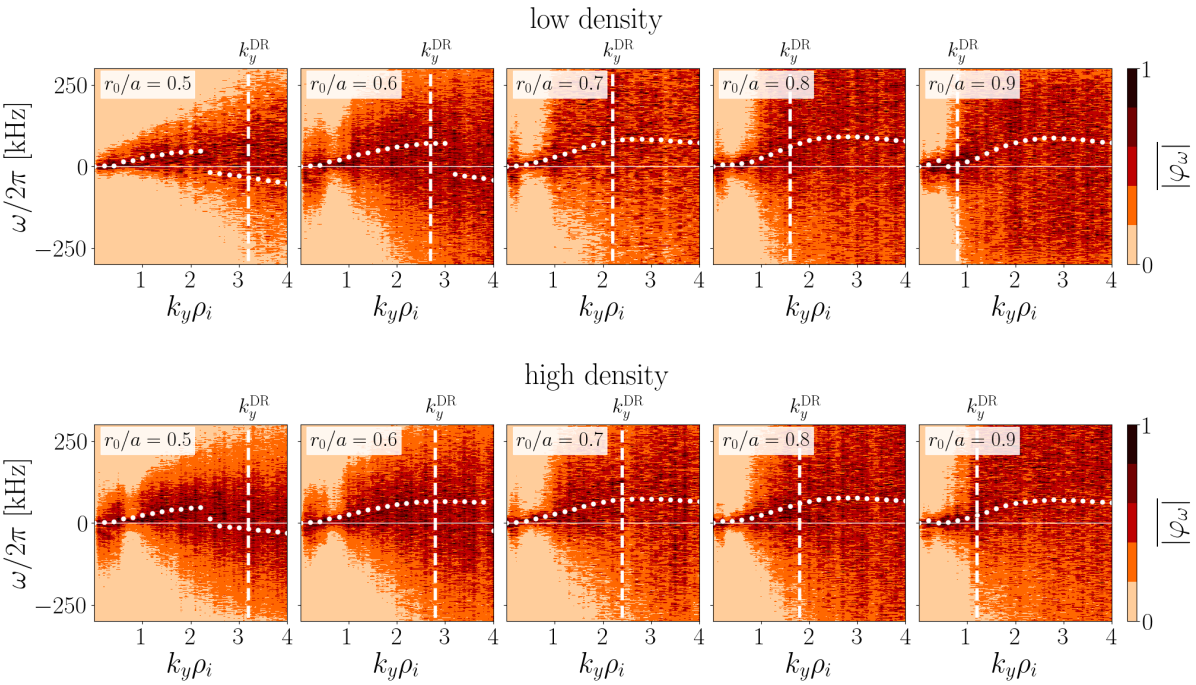

Figure 5.14: Nonlinear frequency spectrum of $\sum_{k_x}\langle\widehat{\varphi}^{tb}_{k_xk_y}\rangle$ for the low (top) and high (bottom) density scenarios computed with `stella` as a function of k_y. The amplitudes $|\check{\varphi}_\omega|$ are normalized to their maximum value at each k_y. The white dots are the results of linear k_y scans assuming $k_x = 0$ and the vertical dashed lines indicates de value that k_y^{DR} takes in each situation.

fixed $k_x = 0$. Since the modes $\widehat{\varphi}^{tb}_{k_xk_y}$ are complex values, we do not expect a symmetry in $|\check{\varphi}_\omega|$ with respect to $\omega = 0$ and, in contrast to section 5.4, we have represented both positive and negative values of ω in figure 5.14. It can be seen that at high k_y, the frequency spectra broadens and a dominant frequency in the nonlinear spectra is lacking. It is interesting though that for the wavenumbers measured by the DR system, changes in the sign of the linear frequency, ω_r, take place. Specifically, for the two analyzed scenarios, the linear frequency is negative for $r_0/a = 0.5$ at $k_y = k_y^{\mathrm{DR}}$, whereas it is positive for all other radii, which points out to a change in the propagation direction of the drift waves driving the instability. On the other hand, for low k_y, the linear frequency values are reasonably close to those of the dominant nonlinear ones, which correspond with the darkest regions of the maps in figure 5.14. This fact can be more clearly observed in figure 5.15, where the normalized amplitudes $\overline{|\varphi_\omega|}(k_y)$ are represented as a function of ω for $k_y\rho_i = 0.6$. In that case, the linear frequency, indicated by a triangle in the figure, is located fairly close to the peak of the nonlinear frequency spectrum for every radial position analyzed. Similar agreements have been reported for the ASDEX Upgrade

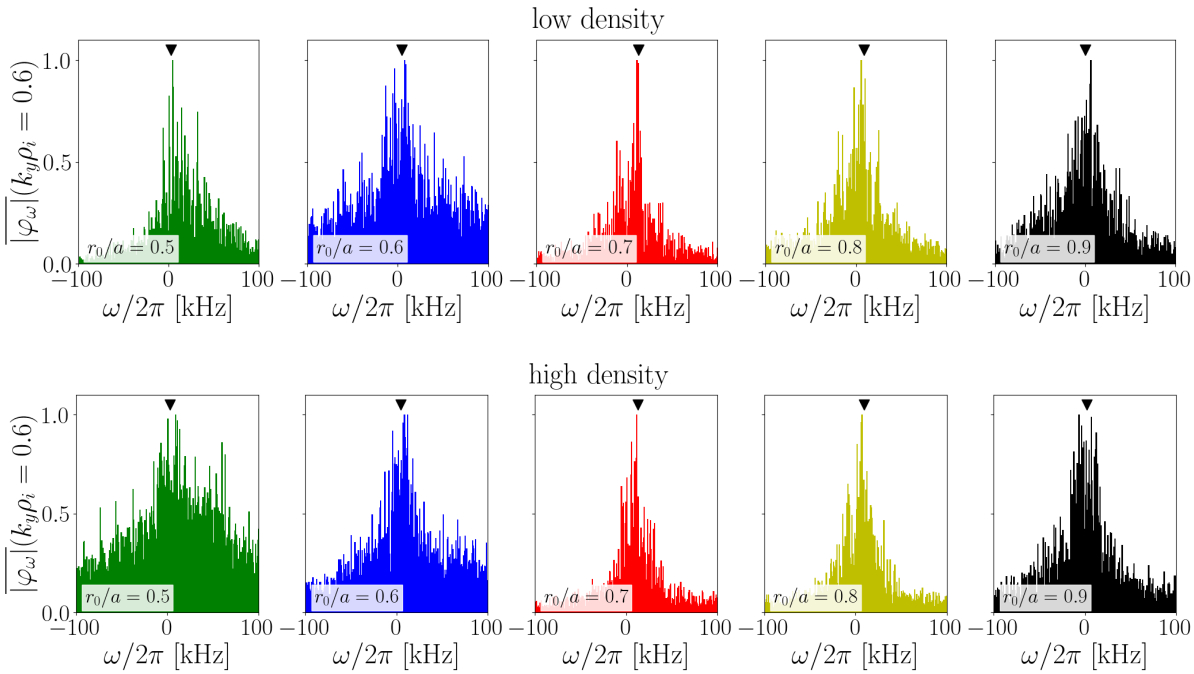

Figure 5.15: Nonlinear results of $\overline{|\varphi_\omega|}$ for the low (top) and high (bottom) density scenarios, evaluated at $k_y\rho_i = 0.6$. The linear result for the mode $(k_x\rho_i, k_y\rho_i) = (0, 0.6)$ is represented as a black triangle in every situation.

tokamak in [80], comparing linear and nonlinear simulations carried out with `GENE`.

Finally, we analyze the localization of the fluctuating electrostatic potential along the flux tube for the wavenumber explored by the DR system. In particular, in figure 5.16 we represent the time-averaged squared amplitude of φ^{tb} evaluated at $k_y = k_y^{\mathrm{DR}}$, this is

$$\left(\varphi^{tb}\right)^2_{\mathrm{DR}}(\zeta) = \left\langle \sum_{k_x} \left| \widehat{\varphi}^{tb}_{k_x k_y = k_y^{\mathrm{DR}}} \right|^2 (\zeta, t) \right\rangle_t . \tag{5.14}$$

To assess the correlation between the structure of nonlinear modes at k_y^{DR} and those computed for the most linearly unstable mode for the same k_y^{DR} (generally located and obtained at $k_x = 0$), we have depicted the parallel structure of the electrostatic potential from these linear simulations in figure 5.17. It is observed that both linear and nonlinear results exhibit similar structures, with slight differences possibly due to the contribution of every k_x mode considered in the nonlinear analysis and, of course, nonlinear effects. In particular, $(\varphi^{tb})^2_{\mathrm{DR}}$ is strongly localized around the center of the flux tube, $\zeta = 0$, for every radial position except at $r_0/a = 0.5$. That localization in ζ overlaps with regions of bad curvature in this configuration of W7-X (see expression 4.2). This suggests that ion-temperature-gradient (ITG) modes [81] play a leading role at $r_0/a > 0.5$. In addition, we can conclude that the linear modes at $k_y = k_y^{\mathrm{DR}}$ propagate in the ion diamagnetic

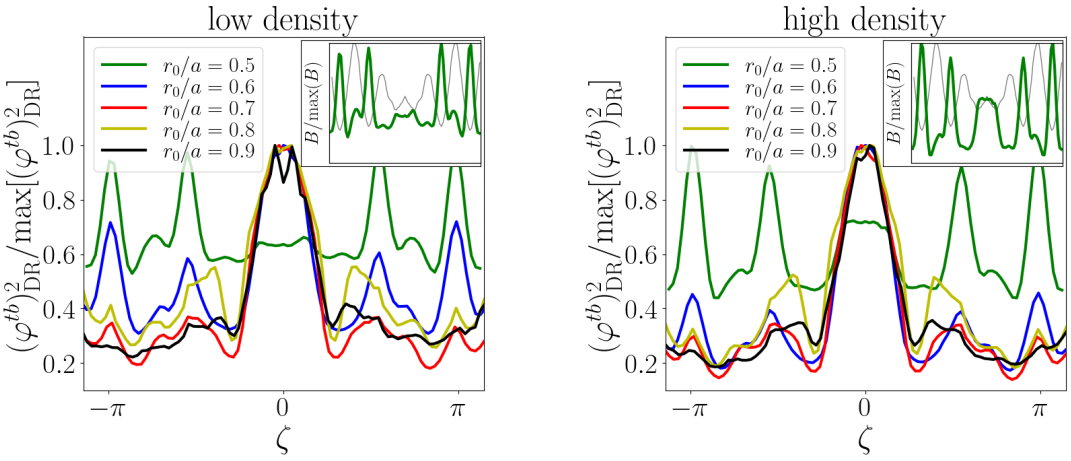

Figure 5.16: Normalized $(\varphi^{tb})^2_{\mathrm{DR}}$ as a function of ζ, computed with `stella` for the low (left) and high (right) density scenarios. The insets show the results corresponding to $r_0/a = 0.5$, together with the magnetic field strength as a gray solid line.

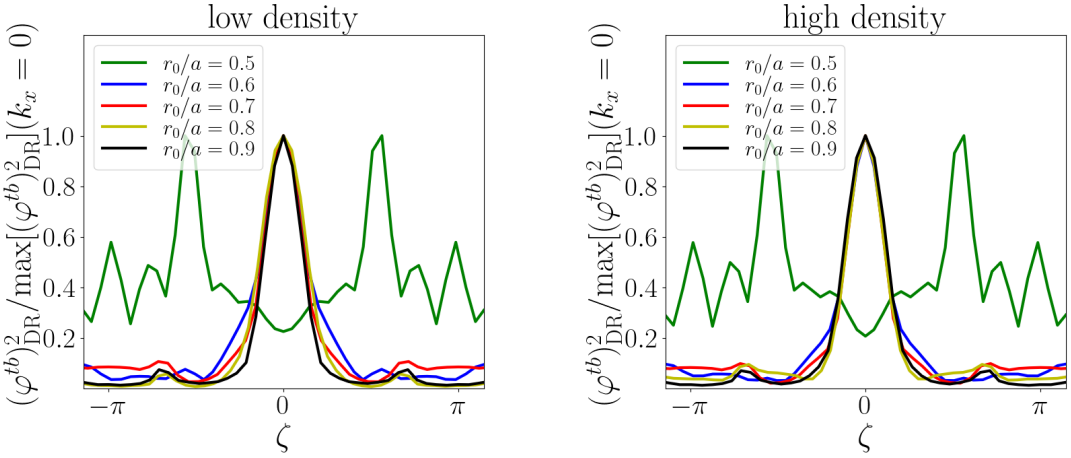

Figure 5.17: Normalized $(\varphi^{tb})^2_{\mathrm{DR}}$ for the linearly unstable mode with $k_x = 0$ as a function of ζ, computed with `stella` for the low (left) and high (right) density scenarios.

direction, which in the present work correspond with positive values of ω (see white dots in figure 5.14), as it is expected for ITG modes. On the other hand, the fluctuating electrostatic potential for the position $r_0/a = 0.5$ is localized at regions of magnetic field wells (see the insets of figure 5.16, where the structure of this fluctuating electrostatic potential is represented together with the magnetic field strength). This fact, and the change in the sign of the linear frequency, points out to a prominent role of trapped electrons on the turbulence at $r_0/a = 0.5$. In summary, looking at $k_y = k_y^{\mathrm{DR}}$, where the standard linear stability analysis finds a change in the sign of the frequency, a very different localization of the turbulent electrostatic potential is found nonlinearly.

5.6. Summary of this chapter

In this chapter, we have used the code `stella` with the aim of calculating turbulent quantities that can be directly compared with Doppler reflectometry measurements in the W7-X stellarator. Five radial positions of two ECRH discharges corresponding to the first operation phase (OP1) of W7-X have been considered with this objective. In the first place, nonlinear simulations have been carried out to compute the amplitude of the density fluctuations at the spatial region and perpendicular wavenumbers explored by the DR system. Numerical results and DR measurements of the squared density fluctuations cover a range of about 15 dB and feature in both cases a monotonic increase with the radial coordinate. This is due to the different regions of the wavenumber spectrum accessed by the diagnostic at each radial location. Discrepancies between the numerical and experimental results in the different fluctuation levels between the two scenarios have also been observed.

To expand the numerical characterization of the turbulence towards other quantities measurable by DR, the frequency spectra of the density fluctuations and of the zonal flow fluctuations have been provided. With regard to the density fluctuations, in general, the largest amplitudes are found for frequencies around a few tens of kHz. For higher frequencies, a slight decrease follows up to approximate $\omega/2\pi = 500$ kHz, where an abrupt fall of the amplitude is found. Concerning the frequency spectra of the zonal flow fluctuations, they are dominated by frequencies with $\omega/2\pi \leq 20$ kHz and find their peak values for $\omega/2\pi \leq 10$ kHz at most radial positions. Future highly time-resolved characterization of the backscattered power and measurements of $u_\perp$ fluctuations at distant locations over the same flux surface will allow to validate these numerical findings.

Finally, the turbulent electrostatic potential has been provided and compared against linear simulations, showing, for low k_y values, that the dominant frequencies of the

nonlinear spectrum cluster nearly around the frequency of the most unstable mode linearly. In addition, these results have also shown that, at $r_0/a = 0.5$, trapped electrons seem to play a leading role on the background turbulence.

CHAPTER 6

Conclusions and main results of this thesis

This research has focused on the simulation of electrostatic turbulence in the stellarator Wendelstein 7-X (W7-X) using the gyrokinetic code `stella`. In particular, the two main objectives of this work have been the correct verification of the code `stella` in the geometry of W7-X and the comparison of experimental measurements obtained during the first experimental campaign of this device with the results obtained from the code.

As outlined in chapter 1, turbulent transport arises to a large extent from microinstabilities caused by plasma fluctuations with wavelengths on the order of the gyroradius (1.3) and frequencies significantly lower than the gyrofrequency (1.4) of the plasma species. This is the dominant transport mechanism in tokamaks. Traditionally, in stellarators, turbulent transport has been studied in less detail due to the predominance of neoclassical transport in low collisionality plasmas. However, this has changed with the advent of neoclassically optimized stellarators. In the first experimental campaigns of W7-X, the first large stellarator optimized for neoclassical transport, it has been shown that in standard plasmas (see figure 1.6) there is a significant discrepancy — approximately of an order of magnitude— between the sum of neoclassical fluxes (for both ions and electrons) combined with radiated power and the input power. This difference has been attributed to turbulence-driven mechanisms, intensifying the interest in studying turbulence, modelled with gyrokinetic theory, in fusion-grade stellarator plasmas.

Gyrokinetic theory, concisely summarized in its electrostatic, collisionless, flux tube version in chapter 2, is used for the study of turbulent transport in strongly magnetized plasmas. It exploits the scale separation between the background magnetic field and plasma profiles, and the much smaller plasma fluctuations, on the order of the Larmor radius. This scale separation is addressed by systematically expanding the Vlasov (2.6)

and quasineutrality (2.1) equations in the small parameter ρ_*, defined by expression (2.8), and averaging them over the fast gyromotion, reducing the dimensionality of the phase-space variables from six to five. In this thesis, we have relied on the δf-gyrokinetic theory, which, in addition, assumes the splitting of the distribution function into a mean component, which up to the lowest order in ρ_* is a Maxwellian distribution, and a fluctuating (or turbulent) component. With the aforementioned considerations, in section 2.2, we have presented the electrostatic and collisionless gyrokinetic system of equations, which consists of the gyrokinetic Vlasov (2.11) and quasineutrality (2.27) equations. Then, in section 2.3, we have particularized them to the flux tube geometry, which fully exploits the differences between scales perpendicular and parallel to the magnetic field $\left(k_\parallel/k_\perp \ll 1\right)$ and serves as the computational domain for `stella`, the code employed in this thesis to solve the gyrokinetic system of equations. The flux tube geometry, illustrated in figure 2.2, allows for the Fourier expansion of the turbulent quantities in terms of the fast perpendicular variations, enabling the representation of the flux tube version of the gyrokinetic equations as (2.41) and (2.43), which is the form in which they are implemented in `stella`. As specified in section 2.4, in order to solve the gyrokinetic system, `stella` employs a mixed explicit-explicit scheme, which offers a significant advantage over purely explicit methods when accounting for the electron dynamics.

The first objective of this work, concerning the verification of gyrokinetic codes, is addressed in chapter 4. Prior to this research, the stellarator community lacked a sufficiently, comprehensive and well-documented set of benchmark tests for gyrokinetic simulations specific to the geometry of these devices. It is worth noting here that, unlike the stellarator community, the tokamak community already had the so-called Cyclone Base Case (CBC) for code verification since the development of the first gyrokinetic codes, thought for the tokamak geometry. In this chapter, we have aimed to fill this gap by proposing a reference benchmark case in the geometry of W7-X. The benchmark described in this chapter has been presented as an extensive comparison between the code `stella` and the well-established code `GENE` in the geometry of W7-X, serving, also, as the verification of `stella` in the stellarator geometry. The benchmark includes a series of linear and nonlinear gyrokinetic simulations against which present and future stellarator gyrokinetic codes can be tested and verified with each other. The linear part of this reference case is covered by tests 1 to 4 (see section 4.2). In the first two tests, we have studied ITG instabilities in two different flux tubes of W7-X, referred to as bean and triangular flux tubes. Test 3 has focused on the study of TEM instabilities driven

by density gradients, where it has been shown that the mixed implicit-explicit method employed by `stella` enables the use of larger time steps compared to fully explicit codes when simulating kinetic electrons, resulting in a significant reduction in the total CPU time spent. This is illustrated in table 4.2 and discussed in subsection 4.2.3. In these three tests, the structure of the electrostatic potential associated with each instability has been provided, and the growth rate and real frequency values obtained with `stella` and `GENE` have been successfully compared (see figures 4.5, 4.6, 4.8 and 4.9 and related discussion). In the last linear test, labeled as test 4, different time traces of the relaxation of the zonal electrostatic potential have been successfully compared with both codes, as shown in figure 4.11. Finally, in test 5, we have computed the nonlinear ITG-driven heat flux and its spectrum in the bean flux tube using both codes (see figures 4.12 and 4.14) and, for completeness, in the triangular flux tube using `stella` (see figure 4.15). As illustrated in table 4.4, the energy fluxes computed in both flux tubes are comparable, with only the radial modes contributing most significantly to the total heat flux differing slightly, as confirmed by figures 4.13 and 4.15 (right).

Before the realization of this thesis, `stella` could only consider the standard twist-and-shift boundary conditions in the coordinate along magnetic field lines for nonlinear simulations. However, as discussed extensively in chapter 3 (specifically in subsection 3.1.1), these boundary conditions impose significant limitations when studying radial positions with low magnetic shear. This issue becomes particularly critical when analyzing the inner radial regions of W7-X, where $|\hat{s}|$ decreases towards the core, as shown in figure 3.1 (right), and becomes too small to perform simulations at a reasonable computational cost. Given that the second objective of this thesis involves the comparison of the results of the simulation against experimental measurements in W7-X, achieving resolution control over the range of wavenumbers and optimizing computational resources have motivated us to adopt alternative boundary conditions, referred to as stellarator symmetric twist-and-shift. These alternative boundary conditions are detailed in subsection 3.1.2, and their implementation in `stella` has been a major contribution of this thesis. We have tested this implementation at three different radial positions of W7-X (see figures 3.4, 3.5, 3.6 and related discussion) and confirmed that employing these boundary conditions improves the code performance when examining flux tubes at radial locations where $\hat{s} \ll 1$, as clearly demonstrated in tables 3.2 and 3.3. In fact, figure 3.6 illustrates an example where completing a simulation using standard twist-and-shift boundary conditions was unfeasible, whereas a converged result for the ion heat flux was successfully obtained with the new implemented stellarator symetric twist-and-shift

boundary conditions.

Finally, with the implementation of the stellarator symmetric twist-and-shift boundary conditions, we have been able to tackle the second objective of this work: comparing the results obtained with `stella` against experimental measurements. Therefore, in chapter 5, we have used the code to calculate turbulent quantities suitable for a direct comparison against Doppler reflectometry (DR) measurements in the W7-X stellarator. For this purpose, five radial positions from two ECRH discharges belonging to the first operational phase (OP1) of W7-X have been selected. The values of the profiles of these discharges at the analyzed positions can be found in table 5.1. In section 5.3, nonlinear simulations have been conducted to evaluate the amplitude of density fluctuations at the spatial regions and perpendicular wavenumbers where the DR system measures. Figure 5.8 illustrates how the numerical results and DR measurements of squared density fluctuations span a range of approximately 15 dB, both exhibiting a monotonic increase with the radial coordinate. This trend arises from the different wavenumbers accessed by the diagnostic at each radial location, as described in figure 5.7 and the discussion of figure 5.9. To extend the numerical characterization of turbulence to other DR-measurable quantities, the frequency spectra of density and zonal flow fluctuations have been provided in section 5.4. Our objective is for these results to serve as predictions for future experimental campaigns of W7-X. As shown in figure 5.12, regarding density fluctuations, the highest amplitudes are typically found at frequencies around several tens of kHz. Beyond this range, a gradual decline is observed up to approximately $\omega/2\pi = 500$ kHz, where the amplitude sharply decreases. Regarding the zonal flow fluctuation spectra, figure 5.13 demonstrates that they are predominantly governed by frequencies of $\omega/2\pi \leq 20$ kHz, peaking at $\omega/2\pi \leq 10$ kHz across most radial positions. Future time-resolved measurements of backscattered power and rotation velocity fluctuations at varying points on the same flux surface will be essential to validate these numerical predictions.

As a general conclusion, the two main objectives of this thesis —the verification and validation of the gyrokinetic code `stella` in the W7-X geometry— have been successfully achieved. Additionally, we have also provided predictions for turbulent quantities that will be valuable for the upcoming experimental campaigns of this stellarator.

Bibliography

[1] A. González-Jerez, P. Xanthopoulos, J.M. García-Regaña, I. Calvo, J. Alcusón, A. Bañón Navarro, M. Barnes, F.I. Parra, and J. Geiger.
Electrostatic gyrokinetic simulations in Wendelstein 7-X geometry: benchmark between the codes stella and GENE.
Journal of Plasma Physics, 88(3), June 2022.
doi: 10.1017/s0022377822000393.
URL https://doi.org/10.1017/s0022377822000393.

[2] A. González-Jerez, J.M. García-Regaña, I. Calvo, D. Carralero, T. Estrada, E. Sanchez, and M. Barnes.
Electrostatic microturbulence in W7-X: comparison of local gyrokinetic simulations with doppler reflectometry measurements.
Nuclear Fusion, April 2024.
ISSN 1741-4326.
doi: 10.1088/1741-4326/ad411a.
URL http://dx.doi.org/10.1088/1741-4326/ad411a.

[3] *Teachers' Institutional Graphics Educational REsource webpage.*
URL https://www.dlt.ncssm.edu/tiger/physics.htm.

[4] D. Petkow, G. Herdrich, R. Laufer, R. Gabrielli, and O. Zeile.
Comparative investigation of fusion reactions for space propulsion applications.
Transactions of the Japan society for aeronautical and space sciences, 7(ists26), 2009.
ISSN 1347-3840.
doi: 10.2322/tstj.7.pb-59.
URL http://dx.doi.org/10.2322/tstj.7.Pb_59.

[5] J.D. Jackson.

Classical electrodynamics.
Wiley, New York, NY, 3rd ed. edition, 1999.
ISBN 9780471309321.
URL http://cdsweb.cern.ch/record/490457.

[6] S.E. Wurzel and S.C. Hsu.
Progress toward fusion energy breakeven and gain as measured against the lawson criterion.
Physics of Plasmas, 29(6), June 2022.
ISSN 1089-7674.
doi: 10.1063/5.0083990.
URL http://dx.doi.org/10.1063/5.0083990.

[7] J.D. Lawson.
Some criteria for a power producing thermonuclear reactor.
Proceedings of the Physical Society. Section B, 70(1):6–10, January 1957.
doi: 10.1088/0370-1301/70/1/303.
URL https://doi.org/10.1088/0370-1301/70/1/303.

[8] P. Helander.
Theory of plasma confinement in non-axisymmetric magnetic fields.
Reports on Progress in Physics, 77(8):087001, July 2014.
doi: 10.1088/0034-4885/77/8/087001.
URL https://doi.org/10.1088/0034-4885/77/8/087001.

[9] J. Mailloux, N. Abid, K. Abraham, P. Abreu, O. Adabonyan, P. Adrich, V. Afanasev, M. Afzal, T. Ahlgren, L. Aho-Mantila, N. Aiba, M. Airila, M. Akhtar, R. Albanese, M. Alderson-Martin, D. Alegre, S. Aleiferis, A. Aleksa, A.G. Alekseev, E. Alessi, P. Aleynikov, J. Algualcil, M. Ali, M. Allinson, B. Alper, E. Alves, G. Ambrosino, R. Ambrosino, V. Amosov, E.Andersson Sundén, P. Andrew, B.M. Angelini, C. Angioni, I. Antoniou, L.C. Appel, C. Appelbee, S. Aria, M. Ariola, G. Artaserse, W. Arter, V. Artigues, N. Asakura, A. Ash, N. Ashikawa, V. Aslanyan, M. Astrain, O. Asztalos, D. Auld, F. Auriemma, Y. Austin, L. Avotina, E. Aymerich, A. Baciero, F. Bairaktaris, J. Balbin, L. Balbinot, I. Balboa, M. Balden, C. Balshaw, N. Balshaw, V.K. Bandaru, J. Banks, Yu.F. Baranov, C. Barcellona, A. Barnard, M. Barnard, R. Barnsley, A. Barth, M. Baruzzo, S. Barwell, M. Bassan, A. Batista, P. Batistoni,

L. Baumane, B. Bauvir, L. Baylor, P.S. Beaumont, D. Beckett, A. Begolli, M. Beidler, N. Bekris, M. Beldishevski, E. Belli, F. Belli, É. Belonohy, M. Ben Yaala, J. Benayas, J. Bentley, H. Bergsåker, J. Bernardo, M. Bernert, M. Berry, L. Bertalot, H. Betar, M. Beurskens, S. Bickerton, B. Bieg, J. Bielecki, A. Bierwage, T. Biewer, R. Bilato, P. Bílková, G. Birkenmeier, H. Bishop, J.P.S. Bizarro, J. Blackburn, P. Blanchard, P. Blatchford, V. Bobkov, A. Boboc, P. Bohm, T. Bohm, I. Bolshakova, T. Bolzonella, N. Bonanomi, D. Bonfiglio, X. Bonnin, P. Bonofiglo, S. Boocock, A. Booth, J. Booth, D. Borba, D. Borodin, I. Borodkina, C. Boulbe, C. Bourdelle, M. Bowden, K. Boyd, I.Božičević Mihalić, S.C. Bradnam, V. Braic, L. Brandt, R. Bravanec, B. Breizman, A. Brett, S. Brezinsek, M. Brix, K. Bromley, B. Brown, D. Brunetti, R. Buckingham, M. Buckley, R. Budny, J. Buermans, H. Bufferand, P. Buratti, A. Burgess, A. Buscarino, A. Busse, D. Butcher, E.de la Cal, G. Calabrò, L. Calacci, R. Calado, Y. Camenen, G. Canal, B. Cannas, M. Cappelli, S. Carcangiu, P. Card, A. Cardinali, P. Carman, D. Carnevale, M. Carr, D. Carralero, L. Carraro, I.S. Carvalho, P. Carvalho, I. Casiraghi, F.J. Casson, C. Castaldo, J.P. Catalan, N. Catarino, F. Causa, M. Cavedon, M. Cecconello, C.D. Challis, B. Chamberlain, C.S. Chang, A. Chankin, B. Chapman, M. Chernyshova, A. Chiariello, P. Chmielewski, A. Chomiczewska, L. Chone, G. Ciraolo, D. Ciric, J. Citrin, Ł. Ciupinski, M. Clark, R. Clarkson, C. Clements, M. Cleverly, J.P. Coad, P. Coates, A. Cobalt, V. Coccorese, R. Coelho, J.W. Coenen, I.H. Coffey, A. Colangeli, L. Colas, C. Collins, J. Collins, S. Collins, D. Conka, S. Conroy, B. Conway, N.J. Conway, D. Coombs, P. Cooper, S. Cooper, C. Corradino, G. Corrigan, D. Coster, P. Cox, T. Craciunescu, S. Cramp, C. Crapper, D. Craven, R. Craven, M.Crialesi Esposito, G. Croci, D. Croft, A. Croitoru, K. Crombé, T. Cronin, N. Cruz, C. Crystal, G. Cseh, A. Cufar, A. Cullen, M. Curuia, T. Czarski, H. Dabirikhah, A.Dal Molin, E. Dale, P. Dalgliesh, S. Dalley, J. Dankowski, P. David, A. Davies, S. Davies, G. Davis, K. Dawson, S. Dawson, I.E. Day, M. De Bock, G. De Temmerman, G. De Tommasi, K. Deakin, J. Deane, R. Dejarnac, D. Del Sarto, E. Delabie, D. Del-Castillo-Negrete, A. Dempsey, R.O. Dendy, P. Devynck, A. Di Siena, C. Di Troia, T. Dickson, P. Dinca, T. Dittmar, J. Dobrashian, R.P. Doerner, A.J.H. Donné, S. Dorling, S. Dormido-Canto, D. Douai, S. Dowson, R. Doyle, M. Dreval, P. Drewelow, P. Drews, G. Drummond, Ph. Duckworth, H. Dudding, R. Dumont, P. Dumortier, D. Dunai, T. Dunatov, M. Dunne, I. Ďuran, F. Durodié,

R. Dux, A. Dvornova, R. Eastham, J. Edwards, Th. Eich, A. Eichorn, N. Eidietis, A. Eksaeva, H. El Haroun, G. Ellwood, C. Elsmore, O. Embreus, S. Emery, G. Ericsson, B. Eriksson, F. Eriksson, J. Eriksson, L.G. Eriksson, S. Ertmer, S. Esquembri, A.L. Esquisabel, T. Estrada, G. Evans, S. Evans, E. Fable, D. Fagan, M. Faitsch, M. Falessi, A. Fanni, A. Farahani, I. Farquhar, A. Fasoli, B. Faugeras, S. Fazinić, F. Felici, R. Felton, A. Fernandes, H. Fernandes, J. Ferrand, D.R. Ferreira, J. Ferreira, G. Ferrò, J. Fessey, O. Ficker, A.R. Field, A. Figueiredo, J. Figueiredo, A. Fil, N. Fil, P. Finburg, D. Fiorucci, U. Fischer, G. Fishpool, L. Fittill, M. Fitzgerald, D. Flammini, J. Flanagan, K. Flinders, S. Foley, N. Fonnesu, M. Fontana, J.M. Fontdecaba, S. Forbes, A. Formisano, T. Fornal, L. Fortuna, E. Fortuna-Zalesna, M. Fortune, C. Fowler, E. Fransson, L. Frassinetti, M. Freisinger, R. Fresa, R. Fridström, D. Frigione, T. Fülöp, M. Furseman, V. Fusco, S. Futatani, D. Gadariya, K. Gál, D. Galassi, K. Galkazka, S. Galeani, D. Gallart, R. Galvão, Y. Gao, J. Garcia, M. García-Muñoz, M. Gardener, L. Garzotti, J. Gaspar, R. Gatto, P. Gaudio, D. Gear, T. Gebhart, S. Gee, M. Gelfusa, R. George, S.N. Gerasimov, G. Gervasini, M. Gethins, Z. Ghani, M. Gherendi, F. Ghezzi, J.C. Giacalone, L. Giacomelli, G. Giacometti, C. Gibson, K.J. Gibson, L. Gil, A. Gillgren, D. Gin, E. Giovannozzi, C. Giroud, R. Glen, S. Glöggler, J. Goff, P. Gohil, V. Goloborodko, R. Gomes, B. Gonçalves, M. Goniche, A. Goodyear, S. Gore, G. Gorini, T. Görler, N. Gotts, R. Goulding, E. Gow, B. Graham, J.P. Graves, H. Greuner, B. Grierson, J. Griffiths, S. Griph, D. Grist, W. Gromelski, M. Groth, R. Grove, M. Gruca, D. Guard, N. Gupta, C. Gurl, A. Gusarov, L. Hackett, S. Hacquin, R. Hager, L. Hägg, A. Hakola, M. Halitovs, S. Hall, S.A. Hall, S. Hallworth-Cook, C.J. Ham, D. Hamaguchi, M. Hamed, C. Hamlyn-Harris, K. Hammond, E. Harford, J.R. Harrison, D. Harting, Y. Hatano, D.R. Hatch, T. Haupt, J. Hawes, N.C. Hawkes, J. Hawkins, T. Hayashi, S. Hazael, S. Hazel, P. Heesterman, B. Heidbrink, W. Helou, O. Hemming, S.S. Henderson, R.B. Henriques, D. Hepple, J. Herfindal, G. Hermon, J. Hill, J.C. Hillesheim, K. Hizanidis, A. Hjalmarsson, A. Ho, J. Hobirk, O. Hoenen, C. Hogben, A. Hollingsworth, S. Hollis, E. Hollmann, M. Hölzl, B. Homan, M. Hook, D. Hopley, J. Horáček, D. Horsley, N. Horsten, A. Horton, L.D. Horton, L. Horvath, S. Hotchin, R. Howell, Z. Hu, A. Huber, V. Huber, T. Huddleston, G.T.A. Huijsmans, P. Huynh, A. Hynes, M. Iliasova, D. Imrie, M. Imríšek, J. Ingleby, P. Innocente, K. Insulander Björk, N. Isernia, I. Ivanova-Stanik, E. Ivings, S. Jablonski, S. Jachmich,

T. Jackson, P. Jacquet, H. Järleblad, F. Jaulmes, J.Jenaro Rodriguez, I. Jepu, E. Joffrin, R. Johnson, T. Johnson, J. Johnston, C. Jones, G. Jones, L. Jones, N. Jones, T. Jones, A. Joyce, R. Juarez, M. Juvonen, P. Kalniņa, T. Kaltiaisenaho, J. Kaniewski, A. Kantor, A. Kappatou, J. Karhunen, D. Karkinsky, Yu Kashchuk, M. Kaufman, G. Kaveney, Ye.O. Kazakov, V. Kazantzidis, D.L. Keeling, R. Kelly, M. Kempenaars, C. Kennedy, D. Kennedy, J. Kent, K. Khan, E. Khilkevich, C. Kiefer, J. Kilpeläinen, C. Kim, Hyun-Tae Kim, S.H. Kim, D.B. King, R. King, D. Kinna, V.G. Kiptily, A. Kirjasuo, K.K. Kirov, A. Kirschner, T. kiviniemi, G. Kizane, M. Klas, C. Klepper, A. Klix, G. Kneale, M. Knight, P. Knight, R. Knights, S. Knipe, M. Knolker, S. Knott, M. Kocan, F. Köchl, I. Kodeli, Y. Kolesnichenko, Y. Kominis, M. Kong, V. Korovin, B. Kos, D. Kos, H.R. Koslowski, M. Kotschenreuther, M. Koubiti, E. Kowalska-Strzkeciwilk, K. Koziol, A. Krasilnikov, V. Krasilnikov, M. Kresina, K. Krieger, N. Krishnan, A. Krivska, U. Kruezi, I. Ksikażek, A.B. Kukushkin, H. Kumpulainen, T. Kurki-Suonio, H. Kurotaki, S. Kwak, O.J. Kwon, L. Laguardia, E. Lagzdina, A. Lahtinen, A. Laing, N. Lam, H.T. Lambertz, B. Lane, C. Lane, E.Lascas Neto, E. Łaszyńska, K.D. Lawson, A. Lazaros, E. Lazzaro, G. Learoyd, Chanyoung Lee, S.E. Lee, S. Leerink, T. Leeson, X. Lefebvre, H.J. Leggate, J. Lehmann, M. Lehnen, D. Leichtle, F. Leipold, I. Lengar, M. Lennholm, E. Leon Gutierrez, B. Lepiavko, J. Leppänen, E. Lerche, A. Lescinskis, J. Lewis, W. Leysen, L. Li, Y. Li, J. Likonen, Ch. Linsmeier, B. Lipschultz, X. Litaudon, E. Litherland-Smith, F. Liu, T. Loarer, A. Loarte, R. Lobel, B. Lomanowski, P.J. Lomas, J.M. López, R. Lorenzini, S. Loreti, U. Losada, V.P. Loschiavo, M. Loughlin, Z. Louka, J. Lovell, T. Lowe, C. Lowry, S. Lubbad, T. Luce, R. Lucock, A. Lukin, C. Luna, E.de la Luna, M. Lungaroni, C.P. Lungu, T. Lunt, V. Lutsenko, B. Lyons, A. Lyssoivan, M. Machielsen, E. Macusova, R. Mäenpää, C.F. Maggi, R. Maggiora, M. Magness, S. Mahesan, H. Maier, R. Maingi, K. Malinowski, P. Manas, P. Mantica, M.J. Mantsinen, J. Manyer, A. Manzanares, Ph. Maquet, G. Marceca, N. Marcenko, C. Marchetto, O. Marchuk, A. Mariani, G. Mariano, M. Marin, M. Marinelli, T. Markovič, D. Marocco, L. Marot, S. Marsden, J. Marsh, R. Marshall, L. Martellucci, A. Martin, A.J. Martin, R. Martone, S. Maruyama, M. Maslov, S. Masuzaki, S. Matejcik, M. Mattei, G.F. Matthews, D. Matveev, E. Matveeva, A. Mauriya, F. Maviglia, M. Mayer, M.-L. Mayoral, S. Mazzi, C. Mazzotta, R. McAdams, P.J. McCarthy, K.G. McClements, J. McClenaghan, P. McCullen, D.C. McDonald, D. McGuckin, D. McHugh,

G. McIntyre, R. McKean, J. McKehon, B. McMillan, L. McNamee, A. McShee, A. Meakins, S. Medley, C.J. Meekes, K. Meghani, A.G. Meigs, G. Meisl, S. Meitner, S. Menmuir, K. Mergia, S. Merriman, Ph. Mertens, S. Meshchaninov, A. Messiaen, R. Michling, P. Middleton, D. Middleton-Gear, J. Mietelski, D. Milanesio, E. Milani, F. Militello, A.Militello Asp, J. Milnes, A. Milocco, G. Miloshevsky, C. Minghao, S. Minucci, I. Miron, M. Miyamoto, J. Mlynář, V. Moiseenko, P. Monaghan, I. Monakhov, T. Moody, S. Moon, R. Mooney, S. Moradi, J. Morales, R.B. Morales, S. Mordijck, L. Moreira, L. Morgan, F. Moro, J. Morris, K.-M. Morrison, L. Msero, D. Moulton, T. Mrowetz, T. Mundy, M. Muraglia, A. Murari, A. Muraro, N. Muthusonai, B. N'Konga, Yong-Su Na, F. Nabais, M. Naden, J. Naish, R. Naish, F. Napoli, E. Nardon, V. Naulin, M.F.F. Nave, I. Nedzelskiy, G. Nemtsev, V. Nesenevich, I. Nestoras, R. Neu, V.S. Neverov, S. Ng, M. Nicassio, A.H. Nielsen, D. Nina, D. Nishijima, C. Noble, C.R. Nobs, M. Nocente, D. Nodwell, K. Nordlund, H. Nordman, R. Normanton, J.M. Noterdaeme, S. Nowak, E. Nunn, H. Nyström, M. Oberparleiter, B. Obryk, J. O'Callaghan, T. Odupitan, H.J.C. Oliver, R. Olney, M. O'Mullane, J. Ongena, E. Organ, F. Orsitto, J. Orszagh, T. Osborne, R. Otin, T. Otsuka, A. Owen, Y. Oya, M. Oyaizu, R. Paccagnella, N. Pace, L.W. Packer, S. Paige, E. Pajuste, D. Palade, S.J.P. Pamela, N. Panadero, E. Panontin, A. Papadopoulos, G. Papp, P. Papp, V.V. Parail, C. Pardanaud, J. Parisi, F.Parra Diaz, A. Parsloe, M. Parsons, N. Parsons, M. Passeri, A. Patel, A. Pau, G. Pautasso, R. Pavlichenko, A. Pavone, E. Pawelec, C.Paz Soldan, A. Peacock, M. Pearce, E. Peluso, C. Penot, K. Pepperell, R. Pereira, T. Pereira, E.Perelli Cippo, P. Pereslavtsev, C. Perez von Thun, V. Pericoli, D. Perry, M. Peterka, P. Petersson, G. Petravich, N. Petrella, M. Peyman, M. Pillon, S. Pinches, G. Pintsuk, W. Pires de Sá, A. Pires dos Reis, C. Piron, L. Pionr, A. Pironti, R. Pitts, K.L. van de Plassche, N. Platt, V. Plyusnin, M. Podesta, G. Pokol, F.M. Poli, O.G. Pompilian, S. Popovichev, M. Poradziński, M.T. Porfiri, M. Porkolab, C. Porosnicu, M. Porton, G. Poulipoulis, I. Predebon, G. Prestopino, C. Price, D. Price, M. Price, D. Primetzhofer, P. Prior, G. Provatas, G. Pucella, P. Puglia, K. Purahoo, I. Pusztai, O. Putignano, T. Pütterich, A. Quercia, E. Rachlew, G. Radulescu, V. Radulovic, M. Rainford, P. Raj, G. Ralph, G. Ramogida, D. Rasmussen, J.J. Rasmussen, G. Rattá, S. Ratynskaia, M. Rebai, D. Réfy, R. Reichle, M. Reinke, D. Reiser, C. Reux, S. Reynolds, M.L. Richiusa, S. Richyal, D. Rigamonti, F.G. Rimini, J. Risner, M. Riva, J. Rivero-

Rodriguez, C.M. Roach, R. Robins, S. Robinson, D. Robson, R. Rodionov, P. Rodrigues, M.Rodriguez Ramos, P. Rodriguez-Fernandez, F. Romanelli, M. Romanelli, S. Romanelli, J. Romazanov, R. Rossi, S. Rowe, D. Rowlands, M. Rubel, G. Rubinacci, G. Rubino, L. Ruchko, M. Ruiz, J.Ruiz Ruiz, C. Ruset, J. Rzadkiewicz, S. Saarelma, E. Safi, A. Sahlberg, M. Salewski, A. Salmi, R. Salmon, F. Salzedas, I. Sanders, D. Sandiford, B. Santos, A. Santucci, K. Särkimäki, R. Sarwar, I. Sarychev, O. Sauter, P. Sauwan, N. Scapin, F. Schluck, K. Schmid, S. Schmuck, M. Schneider, P.A. Schneider, D. Schwörer, G. Scott, M. Scott, D. Scraggs, S. Scully, M. Segato, Jaemin Seo, G. Sergienko, M. Sertoli, S.E. Sharapov, A. Shaw, H. Sheikh, U. Sheikh, A. Shepherd, A. Shevelev, P. Shigin, K. Shinohara, S. Shiraiwa, D. Shiraki, M. Short, G. Sias, S.A. Silburn, A. Silva, C. Silva, J. Silva, D. Silvagni, D. Simfukwe, J. Simpson, D. Sinclair, S.K. Sipilä, A.C.C. Sips, P. Sirén, A. Sirinelli, H. Sjöstrand, N. Skinner, J. Slater, N. Smith, P. Smith, J. Snell, G. Snoep, L. Snoj, P. Snyder, S. Soare, E.R. Solano, V. Solokha, A. Somers, C. Sommariva, K. Soni, E. Sorokovoy, M. Sos, J. Sousa, C. Sozzi, S. Spagnolo, T. Spelzini, F. Spineanu, D. Spong, D. Sprada, S. Sridhar, C. Srinivasan, G. Stables, G. Staebler, I. Stamatelatos, Z. Stancar, P. Staniec, G. Stankūnas, M. Stead, E. Stefanikova, A. Stephen, J. Stephens, P. Stevenson, M. Stojanov, P. Strand, H.R. Strauss, S. Strikwerda, P. Ström, C.I. Stuart, W. Studholme, M. Subramani, E. Suchkov, S. Sumida, H.J. Sun, T.E. Susts, J. Svensson, J. Svoboda, R. Sweeney, D. Sytnykov, T. Szabolics, G. Szepesi, B. Tabia, T. Tadić, B. Tál, T. Tala, A. Tallargio, P. Tamain, H. Tan, K. Tanaka, W. Tang, M. Tardocchi, D. Taylor, A.S. Teimane, G. Telesca, N. Teplova, A. Teplukhina, D. Terentyev, A. Terra, D. Terranova, N. Terranova, D. Testa, E. Tholerus, J. Thomas, E. Thoren, A. Thorman, W. Tierens, R.A. Tinguely, A. Tipton, H. Todd, M. Tokitani, P. Tolias, M. Tomeš, A. Tookey, Y. Torikai, U. von Toussaint, P. Tsavalas, D. Tskhakaya, I. Turner, M. Turner, M.M. Turner, M. Turnyanskiy, G. Tvalashvili, S. Tyrrell, M. Tyshchenko, A. Uccello, V. Udintsev, G. Urbanczyk, A. Vadgama, D. Valcarcel, M. Valisa, P.Vallejos Olivares, O. Vallhagen, M. Valovič, D. Van Eester, J. Varje, S. Vartanian, T. Vasilopoulou, G. Vayakis, M. Vecsei, J. Vega, S. Ventre, G. Verdoolaege, C. Verona, G.Verona Rinati, E. Veshchev, N. Vianello, E. Viezzer, L. Vignitchouk, R. Vila, R. Villari, F. Villone, P. Vincenzi, I. Vinyar, B. Viola, A.J. Virtanen, A. Vitins, Z. Vizvary, G. Vlad, M. Vlad, P. Vondráček, P.de Vries, B. Wakeling, N.R. Walkden, M. Walker, R. Walker, M. Walsh, E. Wang, N. Wang, S. Warder, R. Warren,

J. Waterhouse, C. Watts, T. Wauters, A. Weckmann, H.Wedderburn Maxwell, M. Weiland, H. Weisen, M. Weiszflog, P. Welch, N. Wendler, A. West, M. Wheatley, S. Wheeler, A. Whitehead, D. Whittaker, A. Widdowson, S. Wiesen, J. Wilkinson, J.C. Williams, D. Willoughby, I. Wilson, J. Wilson, T. Wilson, M. Wischmeier, P. Wise, G. Withenshaw, A. Withycombe, D. Witts, A. Wojcik-Gargula, E. Wolfrum, R. Wood, C. Woodley, R. Woodley, B. Woods, J. Wright, J.C. Wright, T. Xu, D. Yadikin, M. Yajima, Y. Yakovenko, Y. Yang, W. Yanling, V. Yanovskiy, I. Young, R. Young, R.J. Zabolockis, J. Zacks, R. Zagorski, F.S. Zaitsev, L. Zakharov, A. Zarins, D. Zarzoso Fernandez, K.-D. Zastrow, Y. Zayachuk, M. Zerbini, W. Zhang, Y. Zhou, M. Zlobinski, A. Zocco, A. Zohar, V. Zoita, S. Zoletnik, V.K. Zotta, I. Zoulias, W. Zwingmann, and I. Zychor.
Overview of JET results for optimising ITER operation.
Nuclear Fusion, 62(4):042026, April 2022.
doi: 10.1088/1741-4326/ac47b4.
URL https://doi.org/10.1088/1741-4326/ac47b4.

[10] A. Kallenbach.
Overview of ASDEX upgrade results.
Nuclear Fusion, 57(10):102015, June 2017.
doi: 10.1088/1741-4326/aa64f6.
URL https://doi.org/10.1088/1741-4326/aa64f6.

[11] C. Hidalgo, E. Ascasíbar, D. Alegre, A. Alonso, J. Alonso, R. Antón, A. Baciero, J. Baldzuhn, J.M. Barcala, L. Barrera, E. Blanco, J. Botija, L. Bueno, S. Cabrera, A. de Castro, E. de la Cal, I. Calvo, A. Cappa, D. Carralero, R. Carrasco, B. Carreras, R. Castro, A. de Castro, L. Cebrián, A.A. Chmyga, M. Chamorro, P. Colino, F. de Aragón, M. Drabinskiy, J. Duque, L. Eliseev, F.J. Escoto, T. Estrada, M. Ezzat, F. Fraguas, D. Fernández-Ruiz, J.M. Fontdecaba, A. Gabriel, D. Gadariya, L. García, I. García-Cortés, R. García-Gómez, J.M. García-Regaña, A. González-Jerez, G. Grenfell, J. Guasp, V. Guisse, J. Hernández-Sánchez, J. Hernanz, A. Jiménez-Denche, P. Khabanov, N. Kharchev, R. Kleiber, F. Koechl, T. Kobayashi, G. Kocsis, M. Koepke, A.S. Kozachek, L. Krupnik, F. Lapayese, M. Liniers, B. Liu, D. López-Bruna, B. López-Miranda, U. Losada, E. de la Luna, S.E. Lysenko, F. Martín-Díaz, G. Martín-Gómez, E. Maragkoudakis, J. Martínez-Fernández, K.J. McCarthy, F. Medina, M. Medrano, A.V. Melnikov, P. Méndez, F.J. Miguel, B. van Milligen,

A. Molinero, G. Motojima, S. Mulas, Y. Narushima, M. Navarro, I. Nedzelskiy, R. Nuñez, M. Ochando, S. Ohshima, E. Oyarzábal, J.L. de Pablos, F. Palomares, N. Panadero, F. Papoušek, F. Parra, C. Pastor, I. Pastor, A. de la Peña, R. Peralta, A. Pereira, P. Pons-Villalonga, H. Polaino, A.B. Portas, E. Poveda, F.J. Ramos, G.A. Rattá, M. Redondo, C. Reynoso, E. Rincón, C. Rodríguez-Fernández, L. Rodríguez-Rodrigo, A. Ros, E. Sánchez, J. Sánchez, E. Sánchez-Sarabia, S. Satake, J.A. Sebastián, R. Sharma, N. Smith, C. Silva, E.R. Solano, A. Soleto, M. Spolaore, T. Szepesi, F.L. Tabarés, D. Tafalla, H. Takahashi, N. Tamura, H. Thienpondt, A. Tolkachev, R. Unamuno, J. Varela, J. Vega, J.L. Velasco, I. Voldiner, S. Yamamoto, and the TJ-II Team.

Overview of the TJ-II stellarator research programme towards model validation in fusion plasmas.

Nuclear Fusion, 62(4):042025, April 2022.

doi: 10.1088/1741-4326/ac2ca1.

URL https://doi.org/10.1088/1741-4326/ac2ca1.

[12] M. Fujiwara, K. Kawahata, N. Ohyabu, O. Kaneko, A. Komori, H. Yamada, N. Ashikawa, L.R. Baylor, S.K. Combs, P.C. deVries, M. Emoto, A. Ejiri, P.W. Fisher, H. Funaba, M. Goto, D. Hartmann, K. Ida, H. Idei, S. Iio, K. Ikeda, S. Inagaki, N. Inoue, M. Isobe, S. Kado, K. Khlopenkov, T. Kobuchi, A.V. Krasilnikov, S. Kubo, R. Kumazawa, F. Leuterer, Y. Liang, J.F. Lyon, S. Masuzaki, T. Minami, J. Miyajima, T. Morisaki, S. Morita, S. Murakami, S. Muto, T. Mutoh, Y. Nagayama, N. Nakajima, Y. Nakamura, H. Nakanishi, K. Narihara, K. Nishimura, N. Noda, T. Notake, S. Ohdachi, Y. Oka, S. Okajima, M. Okamoto, M. Osakabe, T. Ozaki, R.O. Pavlichenko, B.J. Peterson, A. Sagara, K. Saito, S. Sakakibara, R. Sakamoto, H. Sanuki, H. Sasao, M. Sasao, K. Sato, M. Sato, T. Seki, T. Shimozuma, M. Shoji, H. Sugama, H. Suzuki, M. Takechi, Y. Takeiri, N. Tamura, K. Tanaka, K. Toi, T. Tokuzawa, Y. Torii, K. Tsumori, K.Y. Watanabe, T. Watanabe, T. Watari, I. Yamada, S. Yamaguchi, S. Yamamoto, M. Yokoyama, N. Yoshida, Y. Yoshimura, Y.P. Zhao, R. Akiyama, K. Haba, M. Iima, J. Kodaira, T. Takita, T. Tsuzuki, K. Yamauchi, H. Yonezu, H. Chikaraishi, S. Hamaguchi, S. Imagawa, N. Inoue, A. Iwamoto, S. Kitagawa, Y. Kubota, R. Maekawa, T. Mito, K. Murai, A. Nishimura, H. Chikaraishi, K. Takahata, H. Tamura, S. Yamada, N. Yanagi, K. Itoh, K. Matsuoka, K. Ohkubo, I. Ohtake, S. Satoh, T. Satow, S. Sudo, S. Tanahashi, K. Yamazaki, Y. Hamada, and O. Motojima.

Overview of LHD experiments.
Nuclear Fusion, 41(10):1355–1367, October 2001.
doi: 10.1088/0029-5515/41/10/305.
URL https://doi.org/10.1088/0029-5515/41/10/305.

[13] T. Sunn Pedersen, I. Abramovic, P. Agostinetti, M. Agredano Torres, S. Äkäslompolo, J. Alcuson Belloso, P. Aleynikov, K. Aleynikova, M. Alhashimi, A. Ali, N. Allen, A. Alonso, G. Anda, T. Andreeva, C. Angioni, A. Arkhipov, A. Arnold, W. Asad, E. Ascasibar, M.H. Aumeunier, K. Avramidis, E. Aymerich, S.G. Baek, J. Bähner, A. Baillod, M. Balden, M. Balden, J. Baldzuhn, S. Ballinger, M. Banduch, S. Bannmann, A. Bañón Navarro, T. Barbui, C. Beidler, C. Belafdil, A. Bencze, A. Benndorf, M. Beurskens, C. Biedermann, O. Biletskyi, B. Blackwell, M. Blatzheim, T. Bluhm, D. Böckenhoff, G. Bongiovi, M. Borchardt, D. Borodin, J. Boscary, H. Bosch, T. Bosmann, B. Böswirth, L. Böttger, A. Bottino, S. Bozhenkov, R. Brakel, C. Brandt, T. Bräuer, H. Braune, S. Brezinsek, K. Brunner, S. Buller, R. Burhenn, R. Bussiahn, B. Buttenschön, A. Buzás, V. Bykov, I. Calvo, K. Camacho Mata, I. Caminal, B. Cannas, A. Cappa, A. Carls, F. Carovani, M. Carr, D. Carralero, B. Carvalho, J. Casas, D. Castano-Bardawil, F. Castejon, N. Chaudhary, I. Chelis, A. Chomiczewska, J.W. Coenen, M. Cole, F. Cordella, Y. Corre, K. Crombe, G. Cseh, B. Csillag, H. Damm, C. Day, M. de Baar, E. De la Cal, S. Degenkolbe, A. Demby, S. Denk, C. Dhard, A. Di Siena, A. Dinklage, T. Dittmar, M. Dreval, M. Drevlak, P. Drewelow, P. Drews, D. Dunai, E. Edlund, F. Effenberg, G. Ehrke, M. Endler, D.A. Ennis, F.J. Escoto, T. Estrada, E. Fable, N. Fahrenkamp, A. Fanni, J. Faustin, J. Fellinger, Y. Feng, W. Figacz, E. Flom, O. Ford, T. Fornal, H. Frerichs, S. Freundt, G. Fuchert, M. Fukuyama, F. Füllenbach, G. Gantenbein, Y. Gao, K. Garcia, J.M. García Regaña, I. García-Cortés, J. Gaspar, D.A. Gates, J. Geiger, B. Geiger, L. Giudicotti, A. González, A. Goriaev, D. Gradic, M. Grahl, J.P. Graves, J. Green, E. Grelier, H. Greuner, S. Groß, H. Grote, M. Groth, M. Gruca, O. Grulke, M. Grün, J. Guerrero Arnaiz, S. Günter, V. Haak, M. Haas, P. Hacker, A. Hakola, A. Hallenbert, K. Hammond, X. Han, S.K. Hansen, J.H. Harris, H. Hartfuß, D. Hartmann, D. Hathiramani, R. Hatzky, J. Hawke, S. Hegedus, B. Hein, B. Heinemann, P. Helander, S. Henneberg, U. Hergenhahn, C. Hidalgo, F. Hindenlang, M. Hirsch, U. Höfel, K.P. Hollfeld, A. Holtz, D. Hopf, D. Höschen, M. Houry, J. Howard, X. Huang, M. Hubeny, S. Hudson, K. Ida, Y. Igitkhanov, V. Igochine, S. Illy, C. Ionita-Schrittwieser,

M. Isobe, M. Jabłczyńska, S. Jablonski, B. Jagielski, M. Jakubowski, A. Jansen van Vuuren, J. Jelonnek, F. Jenko, F. Jenko, T. Jensen, H. Jenzsch, P. Junghanns, J. Kaczmarczyk, J. Kallmeyer, U. Kamionka, M. Kandler, S. Kasilov, Y. Kazakov, D. Kennedy, A. Kharwandikar, M. Khokhlov, C. Kiefer, C. Killer, A. Kirschner, R. Kleiber, T. Klinger, S. Klose, J. Knauer, A. Knieps, F. Köchl, G. Kocsis, Ya.I. Kolesnichenko, A. Könies, R. König, J. Kontula, P. Kornejew, J. Koschinsky, M.M. Kozulia, A. Krämer-Flecken, R. Krampitz, M. Krause, N. Krawczyk, T. Kremeyer, L. Krier, D.M. Kriete, M. Krychowiak, I. Ksiazek, M. Kubkowska, M. Kuczynski, G. Kühner, A. Kumar, T. Kurki-Suonio, S. Kwak, M. Landreman, P.T. Lang, A. Langenberg, H.P. Laqua, H. Laqua, R. Laube, S. Lazerson, M. Lewerentz, C. Li, Y. Liang, Ch. Linsmeier, J. Lion, A. Litnovsky, S. Liu, J. Lobsien, J. Loizu, J. Lore, A. Lorenz, U. Losada, F. Louche, R. Lunsford, V. Lutsenko, M. Machielsen, F. Mackel, J. Maisano-Brown, O. Maj, D. Makowski, G. Manduchi, E. Maragkoudakis, O. Marchuk, S. Marsen, E. Martines, J. Martinez-Fernandez, M. Marushchenko, S. Masuzaki, D. Maurer, M. Mayer, K.J. McCarthy, O. Mccormack, P. McNeely, H. Meister, B. Mendelevitch, S. Mendes, A. Merlo, A. Messian, A. Mielczarek, O. Mishchenko, B. Missal, R. Mitteau, V.E. Moiseenko, A. Mollen, V. Moncada, T. Mönnich, T. Morisaki, D. Moseev, G. Motojima, S. Mulas, M. Mulsow, M. Nagel, D. Naujoks, V. Naulin, T. Neelis, H. Neilson, R. Neu, O. Neubauer, U. Neuner, D. Nicolai, S.K. Nielsen, H. Niemann, T. Nishiza, T. Nishizawa, T. Nishizawa, C. Nührenberg, R. Ochoukov, J. Oelmann, G. Offermanns, K. Ogawa, S. Okamura, J. Ölmanns, J. Ongena, J. Oosterbeek, M. Otte, N. Pablant, N. Panadero Alvarez, N. Panadero Alvarez, A. Pandey, E. Pasch, R. Pavlichenko, A. Pavone, E. Pawelec, G. Pechstein, G. Pelka, V. Perseo, B. Peterson, D. Pilopp, S. Pingel, F. Pisano, B. Plöckl, G. Plunk, P. Pölöskei, B. Pompe, A. Popov, M. Porkolab, J. Proll, M.J. Pueschel, M.-E. Puiatti, A. Puig Sitjes, F. Purps, K. Rahbarnia, M. Rasiński, J. Rasmussen, A. Reiman, F. Reimold, M. Reisner, D. Reiter, M. Richou, R. Riedl, J. Riemann, K. Rieße, G. Roberg-Clark, V. Rohde, J. Romazanov, D. Rondeshagen, P. Rong, L. Rudischhauser, T. Rummel, K. Rummel, A. Runov, N. Rust, L. Ryc, P. Salembier, M. Salewski, E. Sanchez, S. Satake, G. Satheeswaran, J. Schacht, E. Scharff, F. Schauer, J. Schilling, G. Schlisio, K. Schmid, J. Schmitt, O. Schmitz, W. Schneider, M. Schneider, P. Schneider, R. Schrittwieser, T. Schröder, M. Schröder, R. Schroeder, B. Schweer, D. Schwörer,

E. Scott, E. Scott, B. Shanahan, G. Sias, P. Sichta, M. Singer, P. Sinha, S. Sipliä, C. Slaby, M. Sleczka, H. Smith, J. Smoniewski, E. Sonnendrücker, M. Spolaore, A. Spring, R. Stadler, D. Stańczak, T. Stange, I. Stepanov, L. Stephey, J. Stober, U. Stroth, E. Strumberger, C. Suzuki, Y. Suzuki, J. Svensson, T. Szabolics, T. Szepesi, M. Szücs, F.L. Tabarés, N. Tamura, A. Tancetti, C. Tantos, J. Terry, H. Thienpondt, H. Thomsen, M. Thumm, J.M. Travere, P. Traverso, J. Tretter, E. Trier, H. Trimino Mora, T. Tsujimura, Y. Turkin, A. Tykhyi, B. Unterberg, P. van Eeten, B.Ph. van Milligen, M. van Schoor, L. Vano, S. Varoutis, M. Vecsei, L. Vela, J.L. Velasco, M. Vervier, N. Vianello, H. Viebke, R. Vilbrandt, G. Vogel, N. Vogt, C. Volkhausen, A. von Stechow, F. Wagner, E. Wang, H. Wang, F. Warmer, T. Wauters, L. Wegener, T. Wegner, G. Weir, U. Wenzel, A. White, F. Wilde, F. Wilms, T. Windisch, M. Winkler, A. Winter, V. Winters, R. Wolf, A.M. Wright, G.A. Wurden, P. Xanthopoulos, S. Xu, H. Yamada, H. Yamaguchi, M. Yokoyama, M. Yoshinuma, Q. Yu, M. Zamanov, M. Zanini, M. Zarnstorff, D. Zhang, S. Zhou, J. Zhu, C. Zhu, M. Zilker, A. Zocco, H. Zohm, S. Zoletnik, and L. Zsuga.

Experimental confirmation of efficient island divertor operation and successful neoclassical transport optimization in Wendelstein 7-X.

Nuclear Fusion, 62(4):042022, April 2022.

doi: 10.1088/1741-4326/ac2cf5.

URL https://doi.org/10.1088/1741-4326/ac2cf5.

[14] H. Bruhns.

Energietechnologien und Energiewirtschaft: Vorträge auf der DPG-Frühjahrstagung in Dresden 2013.

Deutsche Physikalische Gesellschaft, Bad Honnef, 2013.

[15] T. Sunn Pedersen, M. Otte, S. Lazerson, P. Helander, S. Bozhenkov, C. Biedermann, T. Klinger, R. C. Wolf, H. S. Bosch, I. Abramovic, S. Äkäslompolo, P. Aleynikov, K. Aleynikova, A. Ali, A. Alonso, G. Anda, T. Andreeva, E. Ascasibar, J. Baldzuhn, M. Banduch, T. Barbui, C. Beidler, A. Benndorf, M. Beurskens, W. Biel, D. Birus, B. Blackwell, E. Blanco, M. Blatzheim, T. Bluhm, D. Böckenhoff, P. Bolgert, M. Borchardt, L.G. Böttger, R. Brakel, C. Brandt, T. Bräuer, H. Braune, R. Burhenn, B. Buttenschön, V. Bykov, I. Calvo, A. Cappa, A. Carls, B. Brotas de C., Francisco C., Mark C., M. Cole, S. Costea, G. Cseh, A. Czarnecka, A. Da Molin, E. de la Cal, A. de la Pena, S. Degenkolbe, C. Prakash

Dhard, A. Dinklage, M. Dostal, M. Drevlak, P. Drewelow, P. Drews, A. Dudek, F. Durodie, A. Dzikowicka, P. van Eeten, F. Effenberg, M. Endler, V. Erckmann, T. Estrada, N. Fahrenkamp, J. Fellinger, Y. Feng, W. Figacz, O. Ford, T. Fornal, H. Frerichs, G. Fuchert, M. Garcia-Munoz, B. Geiger, J. Geiger, N. Gierse, A. Gogoleva, B. Goncalves, D. Gradic, M. Grahl, S. Groß, H. Grote, O. Grulke, C. Guerard, Matthias Haas, J. Harris, H.J. Hartfuß, D. Hartmann, D. Hathiramani, B. Hein, S. Heinrich, S. Henneberg, C. Hennig, J. Hernandez, C. Hidalgo, U. Hidalgo, M. Hirsch, U. Höfel, H. Hölbe, A. Hölting, M. Houry, V. Huber, C. Ionita, B. Israeli, S. Jablonski, M. Jakubowski, A. Jansen van Vuuren, H. Jenzsch, J. Kaczmarczyk, J.P. Kallmeyer, U. Kamionka, H. Kasahara, N. Kenmochi, W. Kernbichler, C. Killer, D. Kinna, R. Kleiber, J. Knauer, F. Köchl, G. Kocsis, Y. Kolesnichenko, A. Könies, R. König, P. Kornejew, F. Köster, A. Krämer-Flecken, R. Krampitz, N. Krawzyk, T. Kremeyer, M. Krychowiak, I. Ksiazek, M. Kubkowska, G. Kühner, T. Kurki-Suonio, P. Kurz, K. Küttler, S. Kwak, M. Landreman, A. Langenberg, F. Lapayese, H. Laqua, H.P. Laqua, R. Laube, M. Laux, H. Lentz, M. Lewerentz, Y. Liang, S. Liu, J.F. Lobsien, J. Loizu Cisquella, D. Lopez-Bruna, J. Lore, A. Lorenz, V. Lutsenko, H. Maaßerg, J. Maisano-Brown, O. Marchuk, L. Marrelli, S. Marsen, N. Marushchenko, S. Masuzaki, K. McCarthy, P. McNeely, F. Medina, D. Milojevic, A. Mishchenko, B. Missal, J. Mittelstaedt, A. Mollen, V. Moncada, T. Mönnich, D. Moseev, M. Nagel, D. Naujoks, G. Hutch Neilson, O. Neubauer, U. Neuner, T.T. Ngo, H. Niemann, C. Nührenberg, J. Nührenberg, M. Ochando, K. Ogawa, J. Ongena, H. Oosterbeek, N. Pablant, D. Pacella, L. Pacios, N. Panadero, E. Pasch, I. Pastor, A. Pavone, E. Pawelec, A. Pedrosa, V. Perseo, B. Peterson, D. Pilopp, F. Pisano, M. Ester Puiatti, G. Plunk, M. Preynas, J. Proll, A. Puig Sitjes, F. Purps, M. Rack, K. Rahbarnia, J. Riemann, K. Rißе, P. Rong, J. Rosenberger, L. Rudischhauser, K. Rummel, T. Rummel, A. Runov, N. Rust, L. Ryc, H. Saitoh, S. Satake, J. Schacht, O. Schmitz, S. Schmuck, B. Schneider, M. Schneider, W. Schneider, R. Schrittwieser, M. Schröder, T. Schröder, R. Schröder, H. W. Schumacher, B. Schweer, R. Seki, P. Sinha, S. Sipilae, C. Slaby, H. Smith, J. Sousa, A. Spring, B. Standley, T. Stange, A. von Stechow, L. Stephey, M. Stoneking, U. Stridde, Y. Suzuki, J. Svensson, T. Szabolics, T. Szepesi, H. Thomsen, J.M. Travere, P. Traverso, H. Trimino Mora, H. Tsuchiya, T. Tsuijmura, Y. Turkin, S. Valet, Boudewijn van Milligen, L. Vela, J.L. Velasco, M. Vergote, M. Vervier, H. Viebke, R. Vilbrandt, C. Perez von

Thun, F. Wagner, E. Wang, N. Wang, F. Warmer, T. Wauters, L. Wegener, T. Wegner, G. Weir, J. Wendorf, U. Wenzel, A. Werner, Y. Wie, B. Wiegel, F. Wilde, T. Windisch, M. Winkler, V. Winters, A. Wright, G. Wurden, P. Xanthopoulos, I. Yamada, R. Yasuhara, M. Yokoyama, D. Zhang, M. Zilker, A. Zimbal, A. Zocco, and S. Zoletnik.

Confirmation of the topology of the Wendelstein 7-X magnetic field to better than 1:100, 000.

Nature Communications, 7(1), November 2016.

doi: 10.1038/ncomms13493.

URL https://doi.org/10.1038/ncomms13493.

[16] J. Geiger, C.D. Beidler, Y. Feng, H. Maaßberg, N.B. Marushchenko, and Y. Turkin. Physics in the magnetic configuration space of W7-X.

Plasma Physics and Controlled Fusion, 57(1):014004, November 2015.

doi: 10.1088/0741-3335/57/1/014004.

URL https://doi.org/10.1088/0741-3335/57/1/014004.

[17] C.D. Beidler, H.M. Smith, A. Alonso, T. Andreeva, J. Baldzuhn, M.N.A. Beurskens, M. Borchardt, S.A. Bozhenkov, K.J. Brunner, H. Damm, M. Drevlak, O.P. Ford, G. Fuchert, J. Geiger, P. Helander, U. Hergenhahn, M. Hirsch, U. Höfel, Ye. O. Kazakov, R. Kleiber, M. Krychowiak, S. Kwak, A. Langenberg, H.P. Laqua, U. Neuner, N.A. Pablant, E. Pasch, A. Pavone, T.S. Pedersen, K. Rahbarnia, J. Schilling, E.R. Scott, T. Stange, J. Svensson, H. Thomsen, Y. Turkin, F. Warmer, R.C. Wolf, D. Zhang, I. Abramovic, S. Äkäslompolo, J. Alcusón, P. Aleynikov, K. Aleynikova, A. Ali, A. Alonso, G. Anda, E. Ascasibar, J.P. Bähner, S.G. Baek, M. Balden, M. Banduch, T. Barbui, W. Behr, A. Benndorf, C. Biedermann, W. Biel, B. Blackwell, E. Blanco, M. Blatzheim, S. Ballinger, T. Bluhm, D. Böckenhoff, B. Böswirth, L.-G. Böttger, V. Borsuk, J. Boscary, H.-S. Bosch, R. Brakel, H. Brand, C. Brandt, T. Bräuer, H. Braune, S. Brezinsek, K.-J. Brunner, R. Burhenn, R. Bussiahn, B. Buttenschön, V. Bykov, J. Cai, I. Calvo, B. Cannas, A. Cappa, A. Carls, L. Carraro, B. Carvalho, F. Castejon, A. Charl, N. Chaudhary, D. Chauvin, F. Chernyshev, M. Cianciosa, R. Citarella, G. Claps, J. Coenen, M. Cole, M.J. Cole, F. Cordella, G. Cseh, A. Czarnecka, K. Czerski, M. Czerwinski, G. Czymek, A. da Molin, A. da Silva, A. de la Pena, S. Degenkolbe, C.P. Dhard, M. Dibon, A. Dinklage, T. Dittmar, P. Drewelow, P. Drews, F. Durodie, E. Edlund, F. Effenberg,

G. Ehrke, S. Elgeti, M. Endler, D. Ennis, H. Esteban, T. Estrada, J. Fellinger, Y. Feng, E. Flom, H. Fernandes, W.H. Fietz, W. Figacz, J. Fontdecaba, T. Fornal, H. Frerichs, A. Freund, T. Funaba, A. Galkowski, G. Gantenbein, Y. Gao, J. García Regaña, D. Gates, B. Geiger, V. Giannella, A. Gogoleva, B. Goncalves, A. Goriaev, D. Gradic, M. Grahl, J. Green, H. Greuner, A. Grosman, H. Grote, M. Gruca, O. Grulke, C. Guerard, P. Hacker, X. Han, J.H. Harris, D. Hartmann, D. Hathiramani, B. Hein, B. Heinemann, P. Helander, S. Henneberg, M. Henkel, U. Hergenhahn, J. Hernandez Sanchez, C. Hidalgo, K. P. Hollfeld, A. Hölting, D. Höschen, M. Houry, J. Howard, X. Huang, Z. Huang, M. Hubeny, M. Huber, H. Hunger, K. Ida, T. Ilkei, S. Illy, B. Israeli, S. Jablonski, M. Jakubowski, J. Jelonnek, H. Jenzsch, T. Jesche, M. Jia, P. Junghanns, J. Kacmarczyk, J.-P. Kallmeyer, U. Kamionka, H. Kasahara, W. Kasparek, N. Kenmochi, C. Killer, A. Kirschner, T. Klinger, J. Knauer, M. Knaup, A. Knieps, T. Kobarg, G. Kocsis, F. Köchl, Y. Kolesnichenko, A. Könies, R. König, P. Kornejew, J.-P. Koschinsky, F. Köster, M. Krämer, R. Krampitz, A. Krämer-Flecken, N. Krawczyk, T. Kremeyer, J. Krom, I. Ksiazek, M. Kubkowska, G. Kühner, T. Kurki-Suonio, P.A. Kurz, M. Landreman, P. Lang, R. Lang, S. Langish, H. Laqua, R. Laube, S. Lazerson, C. Lechte, M. Lennartz, W. Leonhardt, C. Li, Y. Li, Y. Liang, C. Linsmeier, S. Liu, J.-F. Lobsien, D. Loesser, J. Loizu Cisquella, J. Lore, A. Lorenz, M. Losert, A. Lücke, A. Lumsdaine, V. Lutsenko, H. Maaßberg, O. Marchuk, J.H. Matthew, S. Marsen, M. Marushchenko, S. Masuzaki, D. Maurer, M. Mayer, K. McCarthy, P. McNeely, A. Meier, D. Mellein, B. Mendelevitch, P. Mertens, D. Mikkelsen, A. Mishchenko, B. Missal, J. Mittelstaedt, T. Mizuuchi, A. Mollen, V. Moncada, T. Mönnich, T. Morisaki, D. Moseev, S. Murakami, G. Náfrádi, M. Nagel, D. Naujoks, H. Neilson, R. Neu, O. Neubauer, T. Ngo, D. Nicolai, S.K. Nielsen, H. Niemann, T. Nishizawa, R. Nocentini, C. Nührenberg, J. Nührenberg, S. Obermayer, G. Offermanns, K. Ogawa, J. Ölmanns, J. Ongena, J.W. Oosterbeek, G. Orozco, M. Otte, L. Pacios Rodriguez, N. Panadero, N. Panadero Alvarez, D. Papenfuß, S. Paqay, E. Pawelec, T.S. Pedersen, G. Pelka, V. Perseo, B. Peterson, D. Pilopp, S. Pingel, F. Pisano, B. Plaum, G. Plunk, P. Pölöskei, M. Porkolab, J. Proll, M.-E. Puiatti, A. Puig Sitjes, F. Purps, M. Rack, S. Récsei, A. Reiman, F. Reimold, D. Reiter, F. Remppel, S. Renard, R. Riedl, J. Riemann, K. Risse, V. Rohde, H. Röhlinger, M. Romé, D. Rondeshagen, P. Rong, B. Roth, L. Rudischhauser, K. Rummel, T. Rummel, A. Runov, N. Rust, L. Ryc, S. Ryosuke, R. Sakamoto, M. Salewski,

A. Samartsev, E. Sánchez, F. Sano, S. Satake, J. Schacht, G. Satheeswaran, F. Schauer, T. Scherer, A. Schlaich, G. Schlisio, F. Schluck, K.-H. Schlüter, J. Schmitt, H. Schmitz, O. Schmitz, S. Schmuck, M. Schneider, W. Schneider, P. Scholz, R. Schrittwieser, M. Schröder, T. Schröder, R. Schroeder, H. Schumacher, B. Schweer, S. Sereda, B. Shanahan, M. Sibilia, P. Sinha, S. Sipliä, C. Slaby, M. Sleczka, W. Spiess, D. A. Spong, A. Spring, R. Stadler, M. Stejner, L. Stephey, U. Stridde, C. Suzuki, V. Szabó, T. Szabolics, T. Szepesi, Z. Szökefalvi-Nagy, N. Tamura, A. Tancetti, J. Terry, J. Thomas, M. Thumm, J.M. Travere, P. Traverso, J. Tretter, H. Trimino Mora, H. Tsuchiya, T. Tsujimura, S. Tulipán, B. Unterberg, I. Vakulchyk, S. Valet, L. Vanó, P. van Eeten, B. van Milligen, A. J. van Vuuren, L. Vela, J.-L. Velasco, M. Vergote, M. Vervier, N. Vianello, H. Viebke, R. Vilbrandt, A. von Stechow, A. Vorköper, S. Wadle, F. Wagner, E. Wang, N. Wang, Z. Wang, T. Wauters, L. Wegener, J. Weggen, T. Wegner, Y. Wei, G. Weir, J. Wendorf, U. Wenzel, A. Werner, A. White, B. Wiegel, F. Wilde, T. Windisch, M. Winkler, A. Winter, V. Winters, S. Wolf, R. C. Wolf, A. Wright, G. Wurden, P. Xanthopoulos, H. Yamada, I. Yamada, R. Yasuhara, M. Yokoyama, M. Zanini, M. Zarnstorff, A. Zeitler, H. Zhang, J. Zhu, M. Zilker, A. Zocco, S. Zoletnik, and M. Zuin.

Demonstration of reduced neoclassical energy transport in wendelstein 7-x.
Nature, 596(7871):221–226, August 2021.
doi: 10.1038/s41586-021-03687-w.
URL https://doi.org/10.1038/s41586-021-03687-w.

[18] H.D. M. Darwin and R.M. Kulsrud.
Neoclassical transport in stellarators.
The Physics of Fluids, 30(2):442–461, February 1987.
doi: 10.1063/1.866395.
URL https://doi.org/10.1063/1.866395.

[19] W.I. van Rij and S.P. Hirshman.
Variational bounds for transport coefficients in three-dimensional toroidal plasmas.
Physics of Fluids B: Plasma Physics, 1(3):563–569, March 1989.
doi: 10.1063/1.859116.
URL https://doi.org/10.1063/1.859116.

[20] R.C. Wolf.
Major results from the first plasma campaign of the Wendelstein 7-X stellarator.

Nuclear Fusion, 57(10):102020, July 2017.
doi: 10.1088/1741-4326/aa770d.
URL https://doi.org/10.1088/1741-4326/aa770d.

[21] T. Klinger.
Overview of first Wendelstein 7-X high-performance operation.
Nuclear Fusion, 59(11):112004, June 2019.
doi: 10.1088/1741-4326/ab03a7.
URL https://doi.org/10.1088/1741-4326/ab03a7.

[22] S.A. Bozhenkov, Y. Kazakov, O.P. Ford, M.N.A. Beurskens, J. Alcusón, J.A. Alonso, J. Baldzuhn, C. Brandt, K.J. Brunner, H. Damm, G. Fuchert, J. Geiger, O. Grulke, M. Hirsch, U. Höfel, Z. Huang, J. Knauer, M. Krychowiak, A. Langenberg, H.P. Laqua, S. Lazerson, N. B. Marushchenko, D. Moseev, M. Otte, N. Pablant, E. Pasch, A. Pavone, J.H.E. Proll, K. Rahbarnia, E.R. Scott, H.M. Smith, T. Stange, A. von Stechow, H. Thomsen, Yu. Turkin, G. Wurden, P. Xanthopoulos, D. Zhang, and R.C. Wolf.
High-performance plasmas after pellet injections in Wendelstein 7-X.
Nuclear Fusion, 60(6):066011, May 2020.
doi: 10.1088/1741-4326/ab7867.
URL https://doi.org/10.1088/1741-4326/ab7867.

[23] P.J. Catto.
Linearized gyro-kinetics.
Plasma Physics, 20(7):719–722, July 1978.
doi: 10.1088/0032-1028/20/7/011.
URL https://doi.org/10.1088/0032-1028/20/7/011.

[24] M. Barnes, F.I. Parra, and M. Landreman.
stella: An operator-split, implicit–explicit δf-gyrokinetic code for general magnetic field configurations.
Journal of Computational Physics, 391:365–380, August 2019.
doi: 10.1016/j.jcp.2019.01.025.
URL https://doi.org/10.1016/j.jcp.2019.01.025.

[25] F. Jenko.
Massively parallel vlasov simulation of electromagnetic drift-wave turbulence.
Computer Physics Communications, 125(1-3):196–209, March 2000.

doi: 10.1016/s0010-4655(99)00489-0.
URL https://doi.org/10.1016/s0010-4655(99)00489-0.

[26] R.J. Goldston.
Introduction to Plasma Physics.
CRC Press, July 2020.
doi: 10.1201/9780367806958.
URL https://doi.org/10.1201/9780367806958.

[27] J.D. Jackson.
Electrodynamics, Classical.
Wiley-VCH Verlag GmbH & Co. KGaA, April 2003.
doi: 10.1002/3527600434.eap109.
URL https://doi.org/10.1002/3527600434.eap109.

[28] F.I. Parra and I. Calvo.
Phase-space lagrangian derivation of electrostatic gyrokinetics in general geometry.
Plasma Physics and Controlled Fusion, 53(4):045001, February 2011.
doi: 10.1088/0741-3335/53/4/045001.
URL https://doi.org/10.1088/0741-3335/53/4/045001.

[29] I. Calvo and F.I. Parra.
Long-wavelength limit of gyrokinetics in a turbulent tokamak and its intrinsic ambipolarity.
Plasma Physics and Controlled Fusion, 54(11):115007, October 2012.
doi: 10.1088/0741-3335/54/11/115007.
URL https://doi.org/10.1088/0741-3335/54/11/115007.

[30] E. Sánchez, J.M. García-Regaña, A. Bañón Navarro, J.H.E. Proll, C. Mora Moreno, A. González-Jerez, I. Calvo, R. Kleiber, J. Riemann, J. Smoniewski, M. Barnes, and F.I. Parra.
Gyrokinetic simulations in stellarators using different computational domains.
Nuclear Fusion, 61(11):116074, October 2021.
doi: 10.1088/1741-4326/ac2a87.
URL https://doi.org/10.1088/1741-4326/ac2a87.

[31] S.P. Hirshman.
Steepest-descent moment method for three-dimensional magnetohydrodynamic equilibria.

Physics of Fluids, 26(12):3553, 1983.
doi: 10.1063/1.864116.
URL https://doi.org/10.1063/1.864116.

[32] S. Gottlieb, C.W. Shu, and E. Tadmor.
Strong stability-preserving high-order time discretization methods.
SIAM Review, 43(1):89–112, January 2001.
ISSN 1095-7200.
doi: 10.1137/s003614450036757x.
URL http://dx.doi.org/10.1137/S003614450036757X.

[33] M.A. Beer, S.C. Cowley, and G.W. Hammett.
Field-aligned coordinates for nonlinear simulations of tokamak turbulence.
Physics of Plasmas, 2(7):2687–2700, August 1995.
doi: 10.1063/1.871232.
URL https://doi.org/10.1063/1.871232.

[34] M.F. Martin, M. Landreman, P. Xanthopoulos, N.R. Mandell, and W. Dorland.
The parallel boundary condition for turbulence simulations in low magnetic shear devices.
Plasma Physics and Controlled Fusion, 60(9):095008, July 2018.
doi: 10.1088/1361-6587/aad38a.
URL https://doi.org/10.1088/1361-6587/aad38a.

[35] R.L. Dewar and S.R. Hudson.
Stellarator symmetry.
Physica D: Nonlinear Phenomena, 112(1–2):275–280, January 1998.
ISSN 0167-2789.
doi: 10.1016/s0167-2789(97)00216-9.
URL http://dx.doi.org/10.1016/S0167-2789(97)00216-9.

[36] S.E. Parker, W.W. Lee, and R.A. Santoro.
Gyrokinetic simulation of ion temperature gradient driven turbulence in 3D toroidal geometry.
Physical Review Letters, 71(13):2042–2045, September 1993.
doi: 10.1103/physrevlett.71.2042.
URL https://doi.org/10.1103/physrevlett.71.2042.

[37] M. Kotschenreuther, G. Rewoldt, and W.M. Tang.
Comparison of initial value and eigenvalue codes for kinetic toroidal plasma instabilities.
Computer Physics Communications, 88(2-3):128–140, August 1995.
doi: 10.1016/0010-4655(95)00035-e.
URL https://doi.org/10.1016/0010-4655(95)00035-e.

[38] Z. Lin.
Turbulent transport reduction by zonal flows: massively parallel simulations.
Science, 281(5384):1835–1837, September 1998.
doi: 10.1126/science.281.5384.1835.
URL https://doi.org/10.1126/science.281.5384.1835.

[39] W. Dorland, F. Jenko, M. Kotschenreuther, and B.N. Rogers.
Electron temperature gradient turbulence.
Physical Review Letters, 85(26):5579–5582, December 2000.
doi: 10.1103/physrevlett.85.5579.
URL https://doi.org/10.1103/physrevlett.85.5579.

[40] J. Candy and R.E. Waltz.
An eulerian gyrokinetic-Maxwell solver.
Journal of Computational Physics, 186(2):545–581, April 2003.
doi: 10.1016/s0021-9991(03)00079-2.
URL https://doi.org/10.1016/s0021-9991(03)00079-2.

[41] S. Jolliet, A. Bottino, P. Angelino, R. Hatzky, T.M. Tran, B.F. Mcmillan, O. Sauter, K. Appert, Y. Idomura, and L. Villard.
A global collisionless PIC code in magnetic coordinates.
Computer Physics Communications, 177(5):409–425, September 2007.
doi: 10.1016/j.cpc.2007.04.006.
URL https://doi.org/10.1016/j.cpc.2007.04.006.

[42] A.G. Peeters, Y. Camenen, F.J. Casson, W.A. Hornsby, A.P. Snodin, D. Strintzi, and G. Szepesi.
The nonlinear gyro-kinetic flux tube code GKW.
Computer Physics Communications, 180(12):2650–2672, December 2009.
doi: 10.1016/j.cpc.2009.07.001.
URL https://doi.org/10.1016/j.cpc.2009.07.001.

[43] V. Kornilov, R. Kleiber, R. Hatzky, L. Villard, and G. Jost.
Gyrokinetic global three-dimensional simulations of linear ion-temperature-gradient modes in Wendelstein 7-X.
Physics of Plasmas, 11(6):3196–3202, June 2004.
doi: 10.1063/1.1737393.
URL https://doi.org/10.1063/1.1737393.

[44] T.H. Watanabe and H. Sugama.
Velocity–space structures of distribution function in toroidal ion temperature gradient turbulence.
Nuclear Fusion, 46(1):24–32, December 2005.
doi: 10.1088/0029-5515/46/1/003.
URL https://doi.org/10.1088/0029-5515/46/1/003.

[45] P. Xanthopoulos and F. Jenko.
Gyrokinetic analysis of linear microinstabilities for the stellarator Wendelstein 7-X.
Physics of Plasmas, 14(4):042501, April 2007.
doi: 10.1063/1.2714328.
URL https://doi.org/10.1063/1.2714328.

[46] J.A. Baumgaertel, E.A. Belli, W. Dorland, W. Guttenfelder, G.W. Hammett, D.R. Mikkelsen, G. Rewoldt, W.M. Tang, and P. Xanthopoulos.
Simulating gyrokinetic microinstabilities in stellarator geometry with GS2.
Physics of Plasmas, 18(12):122301, December 2011.
doi: 10.1063/1.3662064.
URL https://doi.org/10.1063/1.3662064.

[47] M.D.J. Cole, R. Hager, T. Moritaka, J. Dominski, R. Kleiber, S. Ku, S.A. Lazerson, J. Riemann, and C.S. Chang.
Verification of the global gyrokinetic stellarator code XGC-S for linear ion temperature gradient driven modes.
Physics of Plasmas, 26(8):082501, August 2019.
doi: 10.1063/1.5109259.
URL https://doi.org/10.1063/1.5109259.

[48] M. Maurer, A. Bañón-Navarro, T. Dannert, M. Restelli, F. Hindenlang, T. Görler, D. Told, D. Jarema, G. Merlo, and F. Jenko.
GENE-3D: a global gyrokinetic turbulence code for stellarators.

Journal of Computational Physics, 420:109694, November 2020.
doi: 10.1016/j.jcp.2020.109694.
URL https://doi.org/10.1016/j.jcp.2020.109694.

[49] H.Y. Wang, I. Holod, Z. Lin, J. Bao, J.Y. Fu, P.F. Liu, J.H. Nicolau, D. Spong, and Y. Xiao.
Global gyrokinetic particle simulations of microturbulence in W7-X and LHD stellarators.
Physics of Plasmas, 27(8):082305, August 2020.
doi: 10.1063/5.0014198.
URL https://doi.org/10.1063/5.0014198.

[50] P. Helander, T. Bird, F. Jenko, R. Kleiber, G.G. Plunk, J.H.E. Proll, J. Riemann, and P. Xanthopoulos.
Advances in stellarator gyrokinetics.
Nuclear Fusion, 55(5):053030, April 2015.
doi: 10.1088/0029-5515/55/5/053030.
URL https://doi.org/10.1088/0029-5515/55/5/053030.

[51] A.M. Dimits, G. Bateman, M.A. Beer, B.I. Cohen, W. Dorland, G.W. Hammett, C. Kim, J.E. Kinsey, M. Kotschenreuther, A.H. Kritz, L.L. Lao, J. Mandrekas, W.M. Nevins, S.E. Parker, A.J. Redd, D.E. Shumaker, R. Sydora, and J. Weiland.
Comparisons and physics basis of tokamak transport models and turbulence simulations.
Physics of Plasmas, 7(3):969–983, March 2000.
doi: 10.1063/1.873896.
URL https://doi.org/10.1063/1.873896.

[52] F. Merz.
Gyrokinetic simulation of multimode plasma turbulence.
PhD thesis, Universität Münster, 2009.

[53] S.P. Hirshman, K.C. Shaing, W.I. van Rij, C.O. Beasley, and E.C. Crume.
Plasma transport coefficients for nonsymmetric toroidal confinement systems.
Physics of Fluids, 29(9):2951–2959, sep 1986.
doi: 10.1063/1.865495.
URL https://doi.org/10.1063%2F1.865495.

[54] J. Riemann, R. Kleiber, and M. Borchardt.
Effects of radial electric fields on linear ITG instabilities in W7-X and LHD.
Plasma Physics and Controlled Fusion, 58(7):074001, May 2016.
doi: 10.1088/0741-3335/58/7/074001.
URL https://doi.org/10.1088/0741-3335/58/7/074001.

[55] J.H.E. Proll, P. Xanthopoulos, and P. Helander.
Collisionless microinstabilities in stellarators. II. numerical simulations.
Physics of Plasmas, 20(12):122506, December 2013.
doi: 10.1063/1.4846835.
URL https://doi.org/10.1063/1.4846835.

[56] J.H.E Proll, H.E. Mynick, P. Xanthopoulos, S.A. Lazerson, and B.J. Faber.
TEM turbulence optimisation in stellarators.
Plasma Physics and Controlled Fusion, 58(1):014006, October 2015.
doi: 10.1088/0741-3335/58/1/014006.
URL https://doi.org/10.1088/0741-3335/58/1/014006.

[57] J.A. Alcusón, P. Xanthopoulos, G.G. Plunk, P. Helander, F. Wilms, Y. Turkin, A. von Stechow, and O. Grulke.
Suppression of electrostatic micro-instabilities in maximum-J stellarators.
Plasma Physics and Controlled Fusion, 62(3):035005, January 2020.
doi: 10.1088/1361-6587/ab630e.
URL https://doi.org/10.1088/1361-6587/ab630e.

[58] J.H.E. Proll.
Trapped-particle instabilities in quasi-isodynamic stellarators.
PhD thesis, Max-Planck-Institute für Plasmaphysik, 2014.

[59] M.N. Rosenbluth and F.L. Hinton.
Poloidal flow driven by ion-temperature-gradient turbulence in tokamaks.
Physical Review Letters, 80(4):724–727, January 1998.
doi: 10.1103/physrevlett.80.724.
URL https://doi.org/10.1103/physrevlett.80.724.

[60] H. Sugama and T.-H. Watanabe.
Dynamics of zonal flows in helical systems.
Physical Review Letters, 94(11), March 2005.

doi: 10.1103/physrevlett.94.115001.
URL https://doi.org/10.1103/physrevlett.94.115001.

[61] A. Mishchenko, P. Helander, and A. Könies.
Collisionless dynamics of zonal flows in stellarator geometry.
Physics of Plasmas, 15(7):072309, July 2008.
doi: 10.1063/1.2963085.
URL https://doi.org/10.1063/1.2963085.

[62] P. Helander, A. Mishchenko, R. Kleiber, and P. Xanthopoulos.
Oscillations of zonal flows in stellarators.
Plasma Physics and Controlled Fusion, 53(5):054006, April 2011.
doi: 10.1088/0741-3335/53/5/054006.
URL https://doi.org/10.1088/0741-3335/53/5/054006.

[63] P. Monreal, I. Calvo, E. Sánchez, F.I. Parra, A. Bustos, A. Könies, R. Kleiber, and T. Görler.
Residual zonal flows in tokamaks and stellarators at arbitrary wavelengths.
Plasma Physics and Controlled Fusion, 58(4):045018, February 2016.
doi: 10.1088/0741-3335/58/4/045018.
URL https://doi.org/10.1088/0741-3335/58/4/045018.

[64] P. Monreal, E. Sánchez, I. Calvo, A. Bustos, F.I. Parra, A. Mishchenko, A. Könies, and R. Kleiber.
Semianalytical calculation of the zonal-flow oscillation frequency in stellarators.
Plasma Physics and Controlled Fusion, 59(6):065005, April 2017.
doi: 10.1088/1361-6587/aa6990.
URL https://doi.org/10.1088/1361-6587/aa6990.

[65] J. Smoniewski, E. Sánchez, I. Calvo, M.J. Pueschel, and J.N. Talmadge.
Comparison of local and global gyrokinetic calculations of collisionless zonal flow damping in quasi-symmetric stellarators.
Physics of Plasmas, 28(4):042503, April 2021.
doi: 10.1063/5.0038841.
URL https://doi.org/10.1063/5.0038841.

[66] J.A. Alonso, E. Sánchez, I. Calvo, J.L. Velasco, K.J. McCarthy, A. Chmyga, L.G. Eliseev, T. Estrada, R. Kleiber, L.I. Krupnik, A.V. Melnikov, P. Monreal, F.I. Parra, S. Perfilov, and A.I. Zhezhera.

Observation of oscillatory radial electric field relaxation in a helical plasma.
Physical Review Letters, 118(18), May 2017.
doi: 10.1103/physrevlett.118.185002.
URL https://doi.org/10.1103/physrevlett.118.185002.

[67] P. Xanthopoulos, F. Merz, T. Görler, and F. Jenko.
Nonlinear gyrokinetic simulations of ion-temperature-gradient turbulence for the optimized Wendelstein 7-X stellarator.
Physical Review Letters, 99(3), July 2007.
doi: 10.1103/physrevlett.99.035002.
URL https://doi.org/10.1103/physrevlett.99.035002.

[68] P. Xanthopoulos, A. Mischchenko, P. Helander, H. Sugama, and T.-H. Watanabe.
Zonal flow dynamics and control of turbulent transport in stellarators.
Physical Review Letters, 107(24), December 2011.
doi: 10.1103/physrevlett.107.245002.
URL https://doi.org/10.1103/physrevlett.107.245002.

[69] A. Bañón-Navarro, G. Merlo, G.G. Plunk, P. Xanthopoulos, A. von Stechow, A. Di Siena, M. Maurer, F. Hindenlang, F. Wilms, and F. Jenko.
Global gyrokinetic simulations of ITG turbulence in the magnetic configuration space of the Wendelstein 7-X stellarator.
Plasma Physics and Controlled Fusion, 62(10):105005, August 2020.
doi: 10.1088/1361-6587/aba858.
URL https://doi.org/10.1088/1361-6587/aba858.

[70] E. Sánchez, A. Mishchenko, J.M. García-Regaña, R. Kleiber, A. Bottino, and L. Villard.
Nonlinear gyrokinetic PIC simulations in stellarators with the code EUTERPE.
Journal of Plasma Physics, 86(5):855860501, 2020.
doi: 10.1017/S0022377820000926.

[71] J.M. García-Regaña, M. Barnes, I. Calvo, F.I. Parra, J.A. Alcusón, R. Davies, A. González-Jerez, A. Mollén, E. Sánchez, J.L. Velasco, and A. Zocco.
Turbulent impurity transport simulations in Wendelstein 7-X plasmas.
Journal of Plasma Physics, 87(1):85587010, February 2021.
doi: 10.1017/s0022377820001543.
URL https://doi.org/10.1017/s0022377820001543.

[72] H. Thienpondt, J.M. García-Regaña, I. Calvo, J.A. Alonso, J.L. Velasco, A. González-Jerez, M. Barnes, K. Brunner, O. Ford, G. Fuchert, J. Knauer, E. Pasch, and L. Vanó.
Prevention of core particle depletion in stellarators by turbulence.
Phys. Rev. Res., 5:L022053, Jun 2023.
doi: 10.1103/PhysRevResearch.5.L022053.
URL https://link.aps.org/doi/10.1103/PhysRevResearch.5.L022053.

[73] D. Carralero, T. Estrada, E. Maragkoudakis, T. Windisch, J.A. Alonso, M. Beurskens, S. Bozhenkov, I. Calvo, H. Damm, O. Ford, G. Fuchert, J.M. García-Regaña, N. Pablant, E. Sánchez, E. Pasch, J.L. Velasco, and the Wendelstein 7-X team.
An experimental characterization of core turbulence regimes in Wendelstein 7-X.
Nuclear Fusion, 61(9):096015, August 2021.
doi: 10.1088/1741-4326/ac112f.
URL https://doi.org/10.1088/1741-4326/ac112f.

[74] T. Windisch, S. Wolf, G. M. Weir, S.A. Bozhenkov, H. Damm, G. Fuchert, O. Grulke, M. Hirsch, W. Kasparek, T. Klinger, C. Lechte, E. Pasch, B. Plaum, and E.A. Scott.
Phased array doppler reflectometry at Wendelstein 7-X.
Review of Scientific Instruments, 89(10):10H115, October 2018.
doi: 10.1063/1.5039287.
URL https://doi.org/10.1063/1.5039287.

[75] T. Estrada, D. Carralero, T. Windisch, E. Sánchez, J.M. García-Regaña, J. Martínez-Fernández, A. de la Peña, J.L. Velasco, J.A. Alonso, M. Beurskens, S. Bozhenkov, H. Damm, G. Fuchert, R. Kleiber, N. Pablant, E. Pasch, and the W7-X team.
Radial electric field and density fluctuations measured by doppler reflectometry during the post-pellet enhanced confinement phase in W7-X.
Nuclear Fusion, 61(4):046008, March 2021.
doi: 10.1088/1741-4326/abddee.
URL https://doi.org/10.1088/1741-4326/abddee.

[76] D. Carralero, T. Estrada, E. Maragkoudakis, T. Windisch, J.A. Alonso, J.L. Velasco, O. Ford, M. Jakubowski, S. Lazerson, M. Beurskens, S. Bozhenkov, I. Calvo,

H. Damm, G. Fuchert, J.M. García-Regaña, U.H. öfel, N. Marushchenko, N. Pablant, E. Sánchez, H.M. Smith, E. Pasch, and T. Stange.
On the role of density fluctuations in the core turbulent transport of Wendelstein 7-X.
Plasma Physics and Controlled Fusion, 64(4):044006, February 2022.
doi: 10.1088/1361-6587/ac4d14.
URL https://doi.org/10.1088/1361-6587/ac4d14.

[77] E.Z. Gusakov and A.V. Surkov.
Spatial and wavenumber resolution of doppler reflectometry.
Plasma Physics and Controlled Fusion, 46(7):1143–1162, June 2004.
doi: 10.1088/0741-3335/46/7/012.
URL https://doi.org/10.1088/0741-3335/46/7/012.

[78] N.B. Marushchenko, Y. Turkin, and H. Maassberg.
Ray-tracing code TRAVIS for ECR heating, EC current drive and ECE diagnostic.
Computer Physics Communications, 185(1):165–176, January 2014.
doi: 10.1016/j.cpc.2013.09.002.
URL https://doi.org/10.1016/j.cpc.2013.09.002.

[79] J.P. Bähner, J.A. Alcusón, S.K. Hansen, A. von Stechow, O. Grulke, T. Windisch, H.M. Smith, Z. Huang, E.M. Edlund, M. Porkolab, M.N.A. Beurskens, S.A. Bozhenkov, O.P. Ford, L. Vanó, A. Langenberg, N. Pablant, G.G. Plunk, A. Bañón Navarro, and F. Jenko.
Phase contrast imaging measurements and numerical simulations of turbulent density fluctuations in gas-fuelled ECRH discharges in Wendelstein 7-X.
Journal of Plasma Physics, 87(3), June 2021.
doi: 10.1017/s0022377821000635.
URL https://doi.org/10.1017/s0022377821000635.

[80] D. Told, F. Jenko, T. Görler, F.J. Casson, and E. Fable.
Characterizing turbulent transport in ASDEX upgrade l-mode plasmas via nonlinear gyrokinetic simulations.
Physics of Plasmas, 20(12):122312, dec 2013.
doi: 10.1063/1.4858899.
URL https://doi.org/10.1063%2F1.4858899.

[81] H. Biglari, P.H. Diamond, and M.N. Rosenbluth.

Toroidal ion-pressure-gradient-driven drift instabilities and transport revisited. *Physics of Fluids B: Plasma Physics*, 1(1):109–118, January 1989. doi: 10.1063/1.859206. URL https://doi.org/10.1063/1.859206.